Title
Optimized Structures for Low-Profile Phase Change Thermal Spreaders

Permalink
https://escholarship.org/uc/item/2m31q8n6

Author
Sharratt, Stephen A.

Publication Date
2012

Peer reviewed|Thesis/dissertation

UNIVERSITY OF CALIFORNIA

Los Angeles

Optimized Structures for Low-Profile Phase Change Thermal Spreaders

A dissertation submitted in partial satisfaction

of the requirements for the degree

Doctor of Philosophy in Mechanical Engineering

by

Stephen Andrew Sharratt

2012

ABSTRACT OF THE DISSERTATION

Optimized Structures for Low-Profile Phase Change

Thermal Spreaders

by

Stephen Andrew Sharratt

Doctor of Philosophy in Mechanical Engineering

University of California, Los Angeles, 2012

Professor Y. Sungtaek Ju

Thin, low-profile phase change thermal spreaders can provide cooling solutions for some of today's most pressing heat flux dissipation issues. These thermal issues are only expected to increase as future electronic circuitry requirements lead to denser and potentially 3D chip packaging. Phase change based heat spreaders, such as heat pipes or vapor chambers, can provide a practical solution for effectively dissipating large heat fluxes. This thesis reports a comprehensive study of state-of-the-art capillary pumped wick structures using computational modeling, micro wick fabrication, and experimental analysis.

Modeling efforts focus on predicting the shape of the liquid meniscus inside a complicated 3D wick structure. It is shown that this liquid shape can drastically affect the wick's thermal resistance. In addition, knowledge of the liquid meniscus shape allows for the computation of key parameters such as permeability and capillary pressure which are necessary for predicting the maximum heat flux.

After the model is validated by comparison to experimental results, the wick structure is optimized so as to decrease overall wick thermal resistance and increase the maximum capillary limited heat flux before dryout. The optimized structures are then fabricated out of both silicon and copper using both traditional and novel micro-fabrication techniques. The wicks are made super-hydrophilic using chemical and thermal oxidation schemes. A sintered monolayer of Cu particles is fabricated and analyzed as well.

The fabricated wick structures are experimentally tested for their heat transfer performance inside a well controlled copper vacuum chamber. Heat fluxes as high as 170 W/cm^2 are realized for Cu wicks with structure heights of 100 μm. The structures optimized for both minimized thermal resistance and high liquid supply ability perform much better than their non-optimized counterparts. The super-hydrophilic oxidation scheme is found to drastically increase the maximum heat flux and decrease thermal resistance.

This research provides key insights as to how to optimize heat pipe structures to minimize thermal resistance and increase maximum heat flux. These thin wick structures can also be combined with a thicker liquid supply layer so that thin, low-resistance evaporator layers can be constructed and higher heat fluxes realized. The work presented in this thesis can be used to aid in the development of high-performance phase change thermal spreaders, allowing for temperature control of a variety of powerful electronic components.

The dissertation of Stephen Andrew Sharratt is approved.

_____

Ivan Catton

_____

Adrienne Lavine

_____

Gerassimos Orkoulas

_____

Y. Sungtaek Ju, Committee Chair

University of California, Los Angeles

2012

DEDICATION

This work is dedicated to my wife, Debbie.

TABLE OF CONTENTS

LIST OF TABLES

LIST OF FIGURES

ACKNOWLEDGEMENT

VITA

2003 - 2007	B.S. Mechanical Engineering
	University of California, Berkeley
2007	Associate Systems Engineer Intern
	NASA Jet Propulsion Laboratory (JPL)
	La Canada – Flintridge, CA
2009	M.S. in Mechanical Engineering
2007 – 2012	Graduate Student Researcher/Teaching Associate
	University of California, Los Angeles

PUBLICATIONS

Sharratt, S., Nam, Y., and Ju, Y.S., "Performance Modeling of Micropost Wicks for Micro Heat Pipes at Low Heat Fluxes," 2010 ASME International Exposition, IMECE2010-40719.

Sharratt, S., Nam, Y., and Ju, Y.S., "Liquid Supply and Heat Transfer Performance of Sintered Cu Monolayer Wicks for Phase Change Heat Transfer Applications," ASME/JSME 8th Thermal Conference 2011, AJTEC2011-44356.

Sharratt, S., Peng, C., and Ju, Y.S., 2012, "Silicon Micro-Post Wicks with Modified Geometries for Improved Phase Change Heat Transfer Performance," To be published.

Sharratt, S., Nam, Y., Peng, C., and Ju, Y.S., 2012, "Advanced Geometry Wicks for Improved High Heat Flux Performance," To be published.

Nam, Y., **Sharratt, S.**, Byon, C., Kim, S.J., and Ju, Y.S., 2010, "Fabrication and Characterization of the Capillary Performance of Superhydrophilic Cu Micropost Arrays," *Journal of Electromechanical Systems*, **19** (3).

Nam, Y., **Sharratt, S.**, Cha, G., and Ju, Y.S., 2011, "Characterization and Modeling of the Heat Transfer Performance of Nanostructured Cu Micropost Wicks," *Journal of Heat Transfer*, October 2011, **133**.

Nam, Y., **Sharratt, S**., and Ju, Y.S., "Nanostructured Copper Micro-Post Wicks for Advanced Heat Pipes," MEMS 2011 Conference Proceedings, Cancun, Mexico.

Fan, A., Bonner, R., **Sharratt, S.**, and Ju, Y.S., "An Innovative Passive Cooling Method for High Performance Light-Emitting Diodes," 28th IEEE Semi-Therm Symposium.

Trujillo, J.E., Kim, J.W., Lan, E.H, **Sharratt, S.**, Ju, Y, and Dunn, B., 2011, "Metal-Matrix Nanocomposites with Tailored Coefficients of Thermal Expansion for Improved Thermomechanical Reliability," Journal of Electronic Materials, December 2011.

Hwang, G.S., Fleming, E., Carne, B., **Sharratt, S.**, Nam, Y., Dussinger, P., Ju, Y.S., and Kaviany, M., 2011, "Multi-artery heat-pipe spreader: Lateral Liquid Supply, International Journal of Heat and Mass Transfer, 54 (2011).

CHAPTER 1

Introduction

Thermal control of an electronic component is often the bottleneck to the device's overall performance. Sufficient temperature control can lead to increased performance, efficiency, reliability, lifetime, and prevention of catastrophic failure. As Moore's law continues to hold and the number of transistors a chip continues to double every 18-24 months, the need for removing larger and larger heat fluxes from integrated circuits continues to increase. Thermal control is also expected to be the eventual bottleneck to the commercial implementation of continually increasing transistor density [1]. Newer, high power electronic components, such as GaAs and Si based transistor amplifiers inside new high performance devices dissipate heat fluxes of approximately 100-300 W/cm^2, High Voltage-High Power Amplifiers (HVHPAs) are expected to dissipate at even higher fluxes: aggressive and innovative thermal solutions are required to maintain appropriate board temperatures [2]. In addition, an expected future transition to 3D chip architectures is also expected to increase the need for thin, low profile, high heat flux cooling solutions [3,4]. For these reasons, the field of thermal management is growing rapidly and the industry's global revenues are expected to grow from $7.5 billion in 2009 to $8 billion in 2011 and $10.9 billion in 2016. Within this field, hardware solutions are expected to provide over 83% percent of the expected revenue. Software management solutions, on the other hand, are expected to only account for ~5% of revenue [5]. Effective thermal solutions depend on the end-user requirements: size and weight, cost, heat flux capability, passive or actively cooled, hot spots, operating temperature range, and material compatibility (including CTE match) to name a few.

Research in the field of high heat flux thermal management over the past few decades has led to new solutions capable of acting as efficient and effective heat spreaders, each with their own advantage and disadvantage. But newer, more aggressive solutions are also needed as heat flux demands continue to rise. Presented here is a brief summary of the current and future demand for high heat flux thermal solutions, recent work performed in the field of developing needed thermal solutions, followed by a summary and overview to the work presented in this thesis.

1.1   High Heat Flux Cooling Demands

High Performance Electronic Components and the Need to Remove High Heat Fluxes

An example of a current thermal challenge is presented for the case of an airborne phased array radar antenna (Fig. 1.1) [6]. Beam pointing of the radar is controlled by the arrays of slats of microwave modules (Fig. 1.1A, and zoomed in view of a single slat array in Fig. 1.1B), each module having circuitry required for sending and receiving. The slats are spaced about 2cm apart.

The microwave modules (rectangular packages in Fig. 1.1B) contain power amplifiers (either GaAs or, in the near future, GaN) that dissipate power on the order of ten watts ($\sim100W/cm^2$) or more for each module. The electrical performance of the power amplifiers decreases with increasing temperature, while the amplifier junction temperatures must be below 150°C (for reliability) while module to module temperature variation is not to exceed 10°C. In addition, silicon devices on the slat for voltage and logic control must be kept at an appropriate temperature for reliable performance. The slats are comprised of vacuum brazed aluminum skins on a core of high-density fin stock and are cooled on one side by coolant flow.
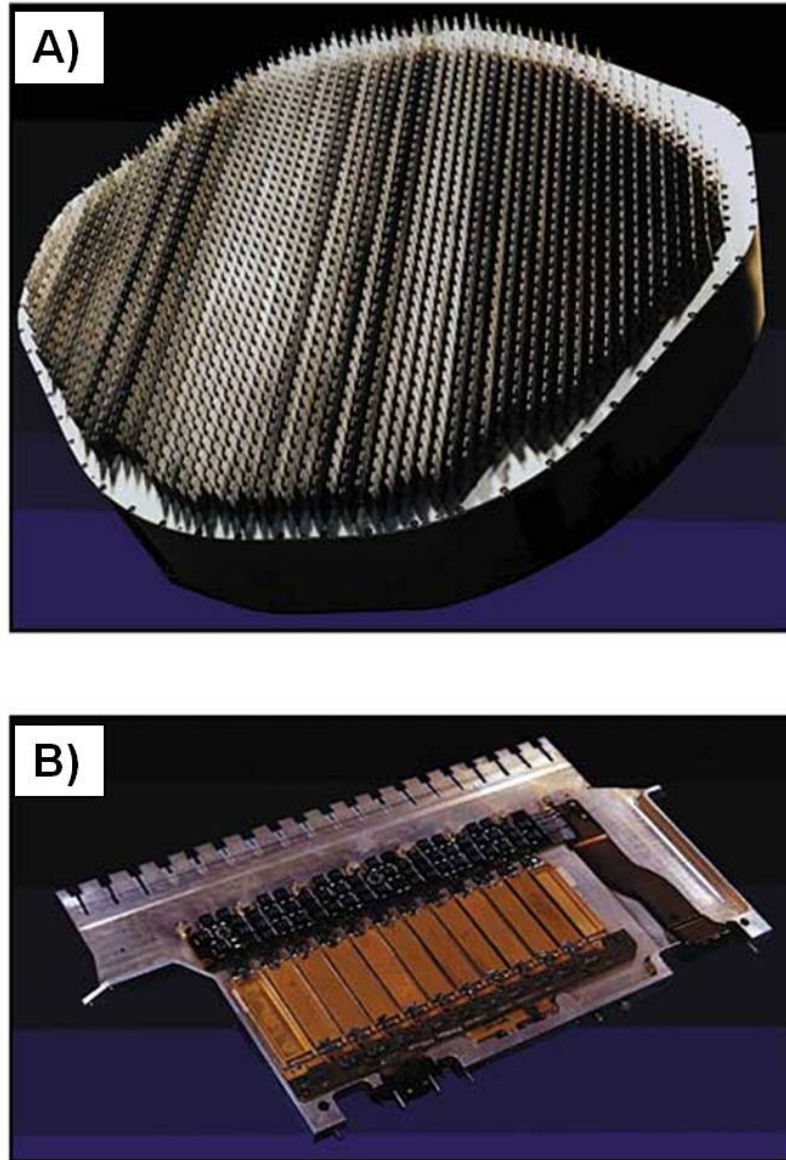
Figure 1.1: A) Phased Array Radar Antenna with Slats, B) Row of Microwave Modules

on a Single Slat [6].

High thermal conductivity materials are used when possible, but CTE mismatch and easy

device repair and replacement often requires the use of the interface materials with low thermal

conductivities.

It is easy to see that size, form factor, and device performance are some (thought by no means all) of the factors limiting possible thermal solutions. As power demands increase (thought to be over 10X current power specs), novel and aggressive thermal and packaging solutions will be required to ensure device performance and operability.

The 3D Electronic Circuit Thermal Problem and Thin, Low Profile Cooling Solutions

3D circuit architectures allow the integration of multiple subsystems onto a single chip. These subsystems may include logic, memory, RF devices, opto-electronic devices, and MEMS. Compared to a 2D chip (Fig. 1.2), converting to a 3D architecture (Fig. 1.3 and 1.4) allows for reduced communication delay between subsystem modules, reduced interconnect length, and increased reliability [3]. In their seminal paper on the subject, K. Banerjee, et al, state that:

> Deep-submicrometer VLSI interconnect scaling trends and the
>
> growing need for heterogeneous integration of technologies in one
>
> single die have created the necessity to seek alternatives to the
>
> existing (2-D) single-active-layer ICs….3-D ICs are an attractive
>
> chip architecture that can alleviate the interconnect related
>
> problems such as delay and power dissipation and can also
>
> facilitate integration of heterogeneous technologies in one single
>
> chip. In fact, several applications of 3-D ICs have been recently
>
> demonstrated, which show the potential of this technology for
>
> effective implementations of SoC designs that are expected to form
>
> the backbone of most future electronic systems. While many
>
> technological challenges need to be overcome for the successful

4

realization of completely monolithic 3-D ICs, advanced 3-D

packaging techniques to realize heterogeneous ICs can be

precursors to the future monolithic 3-D ICs.

However, the thermal management issues associated with this 3D architecture are critical.

As subsystem components are stacked atop each other, the amount of power generated per

available surface area for cooling also increases drastically (Fig. 1.3). In addition, due to the

increased functionality of the 3D circuitry, even less surface area is available for cooling.

Another issue includes the large differences in cooling needs throughout the 3D chip since

temperature non-uniformity can impair the operation of the collective circuit [4].
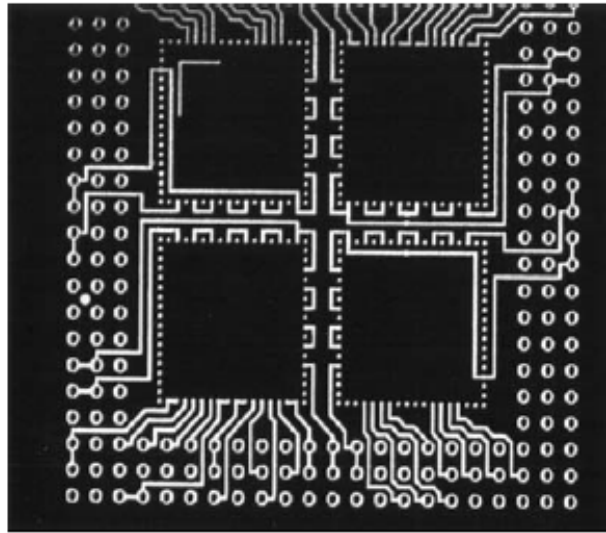
Figure 1.2: Electrical layout of a traditional single layer chip architecture with chips, electrical

circuit tracks and contact pads. [7]

A typical 3D circuit schematic layers various 3D circuit subsystems atop each other to

not only shorten interconnect length, but also reduce space (compare Fig. 3 to Fig. 4). A

traditional cooling scheme applied to the 3D circuit architecture is comprised of the single chip

cooled on only the top side. Vias (metalized holes) connect the circuitry subsystems to allow for effective electrical signal transport across the various layers as well thermal transport to the heat spreader. A thermal interface material (TIM) allows efficient thermal transport to an air cooled heat sink. The number of stacked subsystems is also limited by the ability to transfer thermal energy through the various layers. It is easy to see that the nature of device construction, while excellent from a circuitry performance standpoint, requires innovative cooling solutions if thermal bottlenecks are not to limit intended performance or device capability.
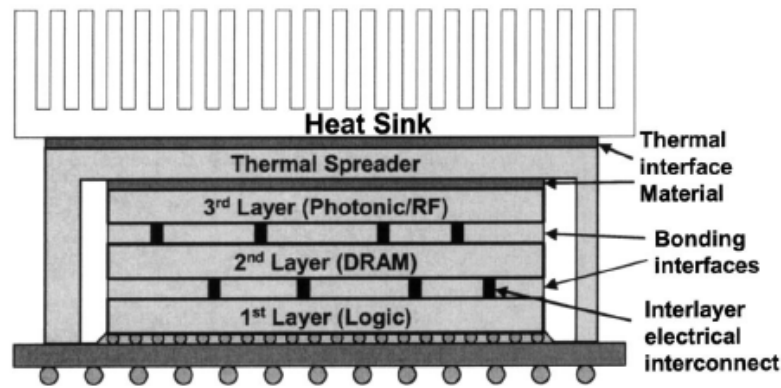
Figure 1.3: 3D Chip Architecture using Traditional On-Top Heat Sink [4].

A proposed solution to this 3D chip architecture uses thin cooling layers to remove thermal energy from the relevant circuit subsystem (Fig. 1.4). The cooling solution, in this case micro-channel evaporators, can be constructed around the electrical/thermal vias. Even though each subsystem is cooled by its own heat dissipation layer, a thermal via is required to transfer the heat through the low thermal conductivity substrate to the heat spreader. From a thermal standpoint, there is no limit to the number of subsystem layers that can be stacked upon each other. In addition, no massive finned heat sink is required atop the chip, since the micro evaporator can effectively transfer thermal energy to where it can be removed effectively.

6
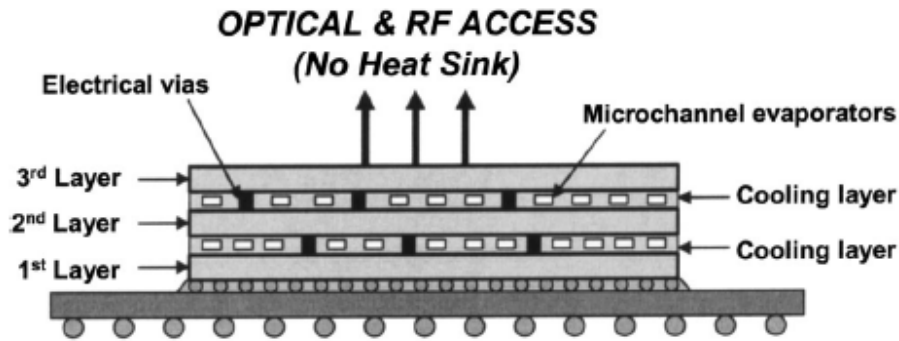
Figure 1.4: 3D Chip Architecture Using Thin Micro-Channel Heat Dissipation Methods [4].

Thin heat spreaders can be an effective solution for the thermal bottlenecks predicted in 3D electronic circuits. These spreaders can be passive (such as a thermal ground plane) or active (such as a pumped micro-channel cooler) depending on the desired space requirements, form factor, noise-level, etc. In either case, the solution must be capable of reliably removing large heat fluxes from a very confined and thin location and then effectively transferring that energy across large distances.

1.2   Review of Electronic Device Cooling Technologies

Traditional Cooling: Solid Conduction Fins and Radiators

Heat flux dissipation from most electronic devices typically follows the same pattern: heat flux is conducted through the device, the device casing, a layer(s) thermal interface material (TIM), a heat spreader, and finally dumped to the ambient (Fig. 1.5). Typical thermal solution layouts are 1D – an electronic component sits on one side of a PC board and the heat flux is removed through the top of the component.
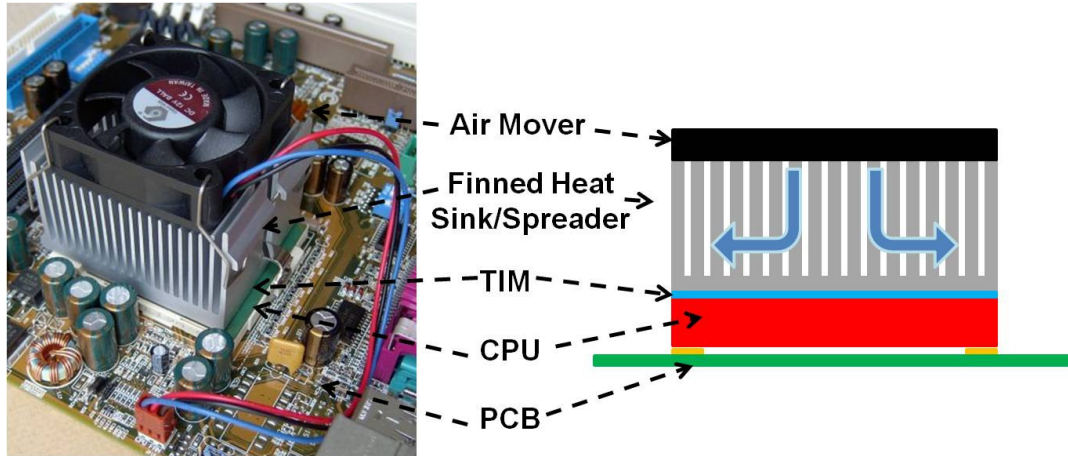
Figure 1.5: Layout and Schematic of Typical Electronics Cooling Systems.

Traditional cooling of electronic components uses a combination of conduction and either forced or natural convection. The heat flux travels through the component's casing, through a thermal interface material (TIM), to a heat sink. The purpose of the TIM is to ensure good thermal contact, minimize the effect of CTE mismatch, and allow for easy removing and replacement. This sink is comprised of a high thermal conductivity material (i.e. copper or aluminum) formed into a high surface area shape such as a collection of fins. This shape allows the effective heat dissipation so that the thermal energy can be removed by forced or natural convection to the ambient. In space environments, where convection is not possible, radiator surfaces are typically utilized so that the thermal energy can be dissipated. In these cases, a high thermal conductivity material such as aluminum (or a heat pipe, discussed later) is used to transfer the thermal energy from the component to the radiator.

Fluid Jet and Spray Impingement

Liquid jet impingement, in which a stream of liquid is directed at the hot spot, is an effective way of removing heat from high power devices [8]. Cooling of the surface is achieved

through a combination of both conduction through the liquid layer, convection, and boiling (Fig. 1.6). Spray cooling typically required a lower fluid flow rate, but a larger pressure dropt at the nozzle. In addition, using droplets instead of a single stream can increase temperature uniformity and delay liquid separation from the wall during boiling [8]. Wang, et al. [9] studied micromachined jets for VLSI cooling and showed effective cooling using an array of jets to cool a 1cm^2 area dissipating 90W. Their data indicated convection coefficients on the order of 0.07 – 4.4 W/cm^{2}K for single phase and ~ 3 W/cm^{2}K for two phase conditions, indicating pool boiling may be occurring. They also showed that control of the flooding level could increase the convection coefficient. Sung and Mudawar [10] used a hybrid system of micro-channels impinged by a jet of HFE-7100 (dielectric fluid) to achieve a CHF of >1100 W/cm^2.
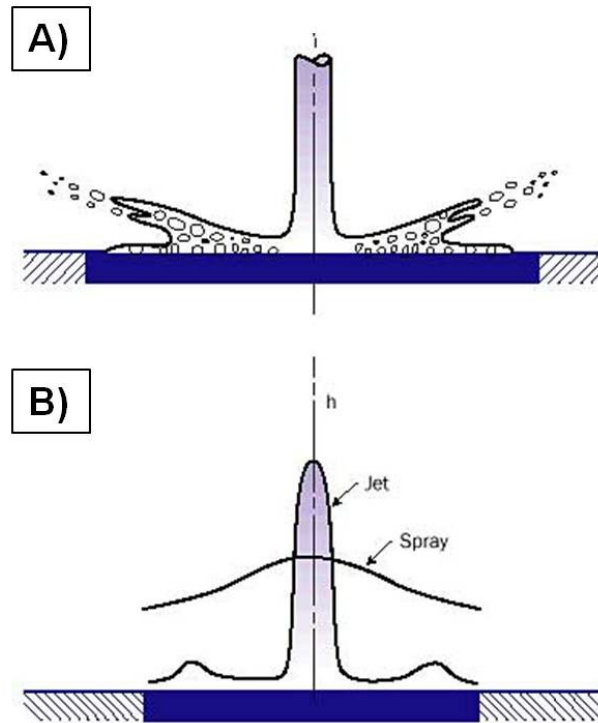
Figure 1.6: A) Sketch of Liquid Jet Impingement Cooling on a Flat Surface. B) Increased heat transfer uniformity due to spray cooling [8].

As pointed about by [10], jet impingement systems are difficult to implement and more expensive than other cooling solutions. Pumping power, pressure drop, liquid flow rate, fluid type, and size constrains must all be considered. Often times to the need for a pump can add significant size, weight, and cost to the final device design.

Micro Channel Cooling

Micro channel cooling makes use of forced flow through a small hydraulic diameter channel ($D_h<1$ mm) [11]. Fluid is pumped through the channel where it convectively cools the heated device. The fluid then travels through another heat sink or radiator to release the energy to the ambient. The small hydraulic diameters result in laminar flow and very high liquid-side heat transfer coefficients (for laminar flow in a circular tube, $Nu_D = hD_h/k_L \sim 4$). Unfortunately, the small length scale can also result in huge pressure drops and associated physical complexities, especially in two phase flow. For a constant flow rate, the pressure drop increases as D_h^{-2}. In addition, the use of a pump to drive the liquid adds complexities, cost, volume, and mass and may limit the potential applications. Garimella and Sobhan have shown that for work up to the year 2000, "given the diversity in the results in the literature, a reliable prediction of the heat transfer rates and pressure drops in micro-channels is not currently possible for design applications such as micro-channel heat sink" [12]. The diversity in results can be seen in the Nusselt number plot (Fig. 1.7) of Morini who performed a comprehensive review of experimental data from other researchers.

Gillot, et al., were able to remove 350 W/cm^2 using both single and two phase micro-channel flow. They found that for two phase flow, the pumping power was ~ ten times lower than single phase flow and also required considerably lower flow rates [13]. However, the

unpredictability of the local heat transfer coefficients due to boiling can result in local temperature variations of 10-15°C as well as backflow of already heated fluid due to bubble expansion. More recently, various companies have offered pumped single and two phase micro channel solutions capable of removing heat fluxes > 1300 W/cm^2 or over 200 W/cm^2 with an overall thickness of less than 300μm [8]. North and Cho [14] constructed a porous metal foam acting as an array of micro-channels to remove over 500 W/cm^2 with a 50°C superheat and a pressure drop of 115 kPa using water.
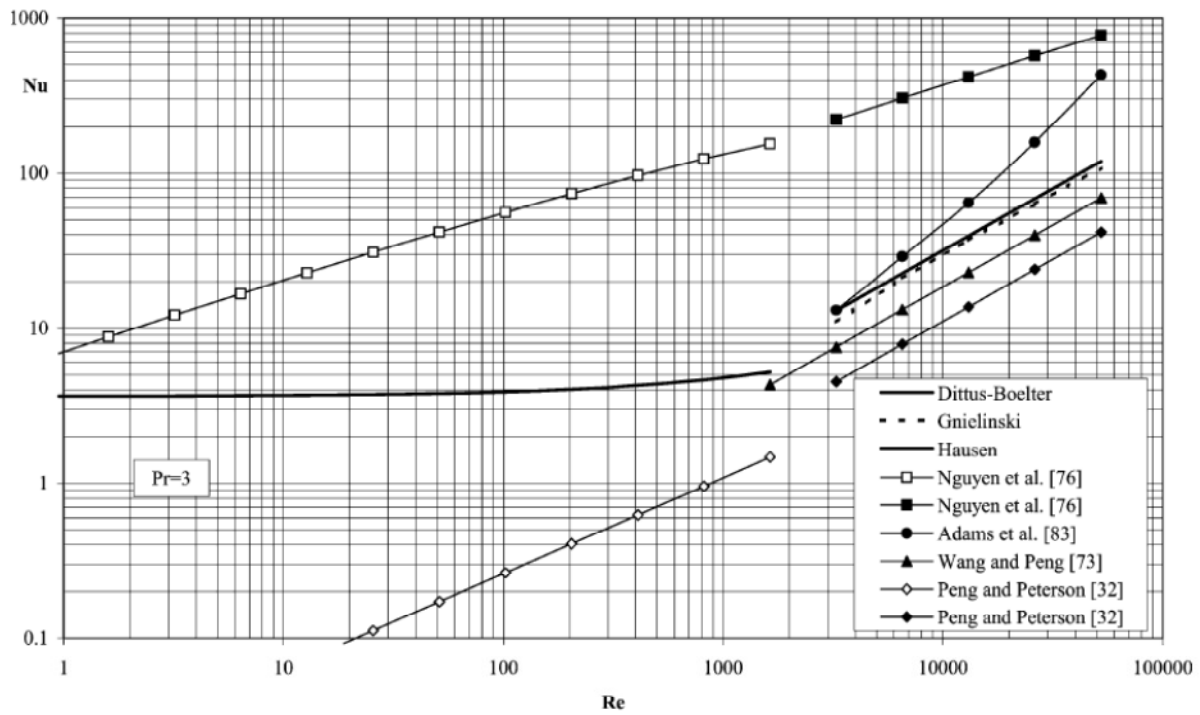
Figure 1.7: Experimental Micro Channel Heat Transfer: Liquid Flow with Pr = 3 from Various Experiments [11].

1.3   Phase-Change Spreaders

A collection of phase change based thermal solutions exist which utilize the vapor flow of an evaporated fluid to transfer large amounts of thermal energy over a large distance with a

small temperature difference. The net result is an extremely high thermal conductivity (50,000 –

200,000 W/mK) in the direction of vapor flow if the travel distance is large [8]. The vapor

returns to the liquid state in the condenser region and then travels back to the evaporator area.

Different form factors such a heat pipe (long and narrow) or vapor chamber (thin and flat) can be

used for different purposes, but the core principles are the same. For example, the heat pipe can

be used for transfer large heat fluxes from a laptop CPU to a fan when the fan cannot be located

atop the CPU due to space constraints. A vapor chamber, on the other hand, can be used to

effectively spread the heat flux out to the condenser region, allowing for smaller temperature

drop requirements and less power-intensive method of cooling (such as a lower mass flow rate

air fan or natural convection) at the condenser region.

Bringing the fluid back to the evaporator region can be accomplished in multiple ways.

The simplest is gravity pumping (Perkins tube), in which the hot spot is located at the lowest end

of the heat pipe. Vapor travels upward due to its lower density, condenses, and then travels back

to the evaporator under the power of gravity. In other devices, such as capillary heat pipes

(CHP), the fluid is wicked via capillary pumping to the evaporator area. The pumping is a result

of the interaction of a micro-structured surface and the surface tension of the fluid. Loop heat

pipes (LHP) operate under a similar principal, but use a design such that the pressure from the

generated vapor can help push the liquid back to the evaporator region.

Passive phase change thermal spreaders offer the capability to meet both thermal and

packaging requirements. Their excellent thermal conductivity and ability to tolerate heat fluxes

on the order of 100-1000W/cm^2 make them an ideal choice for high performance devices such as

the Phased Array Radar Antenna (Fig. 1.1) in which thermal demands are large and the form factor is stringent.

1.4   Summary of Work Presented in this Thesis

This thesis focuses on the evaporator region of a capillary pumped heat pipe or vapor chamber. This region is chosen because it is often the bottle neck to overall thermal performance: the largest heat fluxes and temperature superheats are seen in the evaporator region. The maximum sustained heat flux is of great importance to thermal engineers. After this heat flux has been reached, the effective pipe or chamber thermal conductivity drops rapidly, as heat is transferred only through solid conduction in the thin casing material. The capillary limit, describing the point at which the capillary pressure generated in the evaporator region is not large enough to overcome viscous or gravitational pressure heads is often the deciding factor of the maximum heat flux. For this reason, two the main factors governing max heat flux, permeability and capillary pressure (described in detail in the next chapter), are studied in this work. Other potential heat flux limits include liquid entrainment, sonic choking, and boiling.

Since the evaporator is subject to the highest heat fluxes, it is a key element to the thermal design of the overall device. A large effective heat transfer coefficient in the evaporator region can lower the temperature superheat required for heat flux dissipation. This heat transfer resistance is mostly a function of solid and liquid thermal conduction flow paths. Therefore, it is important to accurately characterize and model both heat flow paths. The attention in this thesis is focused on thin evaporator wicks. These low-profile wicks are designed to either be used alone in extremely thin vapor chamber or integrated into a multi-scale wick (as shown in Fig. 1.8

below) in which there is a specific liquid supply structure for bringing fluid from the condenser to the evaporator and another structure to optimize the heat transfer in the evaporator region.

-Liquid Supply Wick:
high permeability, effective vapor removal

Cooling flow
Condenser wall
Vapor chamber
Heat source

-Thin Evaporator Wick:
high effective thermal conductivity, low liquid supply capability
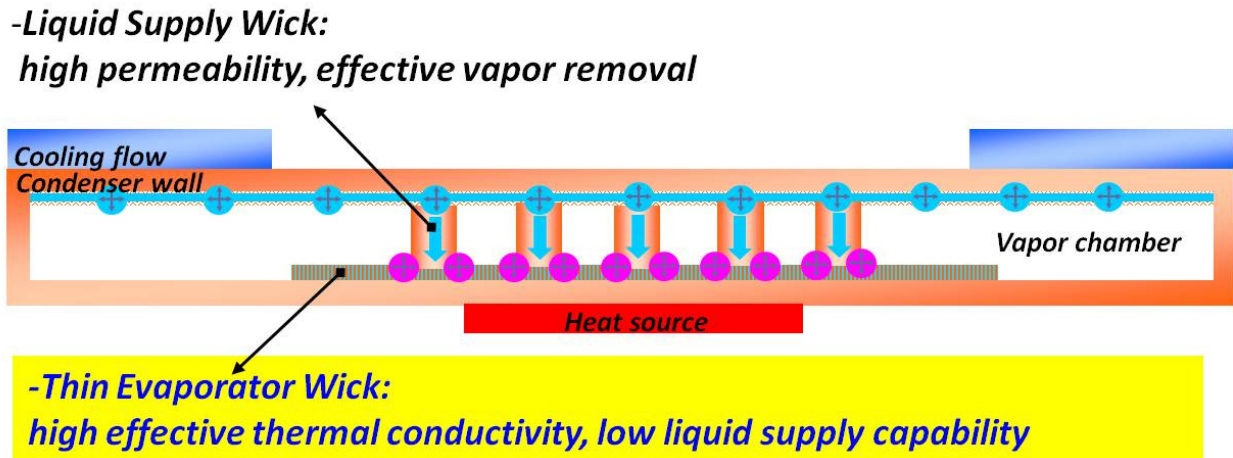
Figure 1.8: Schematic of a thin vapor chamber.

Computational modeling that considers the shape of both the solid and liquid structures is used to predict capillary pressure, permeability, and effective heat transfer coefficient. Thin, high aspect ratio structures are fabricated out of copper and silicon material using micro-manufacturing methods. These structures are chosen based on the information learned from the computational modeling and are designed to optimize both maximum heat flux and effective heat transfer coefficient. A monolayer of sintered spheres (a traditional heat pipe wick structure) is also considered and tested. All the structures are experimentally tested for their heat transfer performance: both maximum heat flux and the effective thermal resistance are measured.

This work can be used to provide insights to the physical phenomena occurring in these "passive" cooling devices and aid in the design of thin, lightweight thermal solutions for powerful electronic components.

14

CHAPTER 2

Computational Modeling of Wick Liquid Supply

Heat pipe or vapor chamber failure can be catastrophic and result in device burn-up. Once the fluid can no longer return from the condenser to the evaporator, solid conduction through the thin walled chamber will be the main mode of energy transfer. For this reason, it is important to study the parameters which govern liquid supply performance. The maximum heat flux supported by a wick is often a function of the liquid supply capability. For a given fluid, two of the key parameters of wick liquid supply are permeability and capillary pressure. Analytically or computationally determining these values can be difficult due to the complex 3D structure and meniscus shape. Fluid choice can also be a strong factor of the maximum heat flux as well. In this chapter, a computational model based on a liquid meniscus energy minimization algorithm is presented. The resulting meniscus shape can be analyzed for its curvature and hence, capillary pressure. In addition, the 3D fluid geometry (including meniscus shape) can be imported in a finite element solver and the permeability can be determined. Using a hexagonal array of cylindrical posts, the results of a rate of rise experiment to the computationally predicted permeability and capillary pressure are compared. Excellent agreement is found between the predicted and experimental results. High solid fraction post geometries were found to result in a lower liquid supply even though the small post spacing can generate high capillary pressure. Low solid fraction geometries were shown to achieve the highest liquid supply capability. The work presented here can be used to optimize a low-profile wick's liquid supply capability and delay the onset of critical heat flux (CHF).

2.1   Background

A capillary pumped heat pipe or vapor chamber transports liquid to the evaporator region by taking advantage of the surface tension interaction between the fluid and micro wick structure. The pore shape resulting from the solid structure influences both capillary pressure (the driving pressure to pump the fluid) and the bulk resistance to flow through the solid matrix. Other pressure heads which may typically be considered are vapor-phase pressure drop as well as gravitational head. Typically, for a given surface energy (contact angle) condition, a higher capillary pressure is associated with a smaller pore size, but also a lower permeability. A larger pore size results in the opposite effect [15,16]. The overall effect of both these terms needs to be determined. A convenient way of doing this is the liquid supply capability (Eqn. 2.1) [17], defined below:

$$Liquid\ Supply\ Capability = \frac{K}{R_{eff}} \quad (2.1)$$

where K is the liquid permeability and R_{eff} is the effective radius of curvature associated with the capillary pressure (both these terms are defined in more detail in the following computational sections). This ratio describes the relative importance of the pressure head provided by the capillary pressure to that of the flow resistance through the solid matrix. Mills described the importance of this ratio on the capillary heat flow limit (Eqn. 2.2) [18], the heat flow (in Watts) at which the capillary pressure is no longer capable of overcoming the bulk flow resistance associated with the required liquid flow to the evaporator

$$q_{capillary\ limit} = M\left(\frac{A_w}{L_{eff}}\right)\left(\frac{K}{R_{eff}}\right) \quad (2.2)$$

where A_w is the cross sectional flow area, and L_{eff} is the distance the fluid travels through the porous matrix. These two terms are often chosen based on heat pipe or vapor chamber size

requirements. *M* is the merit number, a descriptor of a given fluids performance as a heat pipe fluid and is defined as follows (Eqn. 2.3):

$$M = \frac{\rho_L \sigma h_{fg}}{\mu_L} \quad (2.3)$$

The maximum heat flux achievable before liquid-dryout is directly proportional to both the liquid supply ratio and the merit number. At temperatures between 300 and 400K, water has one of the highest merit numbers of any fluid due to its high surface tension (~70 mN/m) and very high enthalpy of vaporization (h_{fg} ~ 2300 kJ/kg) [18,19]. For that reason, water is utilized as the working fluid in our simulations and experiments.

Washburn was the first to propose, in 1921, a model that predicted liquid propagation speeds in a capillary channel by balancing capillary and viscous forces [20]. Typical models of flow through a porous matrix for heat pipe applications are based around either sintered particles or wire mesh since these are typical structures used for manufactured wicks. Due to the tortuous and complicated nature of these structures, most modeling efforts are built on simplifying approximations. At low Reynolds numbers, popular models are based on approximations such as treating the flow through the pores as networks of channel flow in parallel and series [21], shape factor-modified Hagen-Poiseulle flow (for example, Carman-Kozeny) [22], or creeping flow [15]. More recently, new micro-structured post array geometries with very organized and precise geometries have been created using micro-fabrication techniques. Various studies have analyzed and modeled the permeability and capillary pressure inside theses micro-pillar arrays [17,23-25]. Ranjan et al. computed the capillary pressure inside traditional 3D heat pipe wick structures including packed arrays of square and cylindrical posts and spheres [23]. Nam, Y., Sharratt, S., et al. used the Surface Evolver energy minimization algorithm to predict the capillary pressure and permeability for an array of hexagonally packed cylindrical micro posts (the emphasis of this

chapter) and found excellent agreement to experimental results [24]. Xiao et al., used a similar

scheme to computationally determine an optimized set of post spacing and diameters for

capillary liquid supply performance for post heights < 25 μm [25].

In this chapter, a novel method is presented for analyzing the effect of complex

microstructure geometry on liquid supply performance. The Surface Evolver algorithm is used

to determine the equilibrium meniscus shape that results from the surface tension interaction

between the fluid and the solid geometry. The resulting fluid shape can then imported into a 3D

finite element solver and both permeability and capillary pressure can be calculated and the

liquid supply capability can be determined. The capillary pressure, permeability, and liquid

supply are compared to the experimental case of a hexagonally packed cylindrical post array.

2.2   3D Meniscus Calculation

Liquid-Vapor Meniscus

The effect of surface tension on the fluid-vapor interface was calculated using The Surface

Evolver (SE): a program which computes the shape of a surface resulting in an energy

minimization while subject to geometrical or energy constraints [26]. Geometry constraints may

include fluid volume, wall containment, maximum fluid height, and symmetry planes. The only

energy term considered in our simulation is the relative surface energies of the fluid, vapor, and

solid surfaces. These relative surface energies are typically seen in terms of the contact angle of

a droplet on a flat surface. The contact angle value is a result of a balance of these surface

energies which result in a surface energy minimum (Eqn. 2.4 – Young's equation) [27]:

$$\cos\theta = \frac{\sigma_{solid-vapor} - \sigma_{solid-liquid}}{\sigma_{liquid-vapor}} \quad (2.4)$$

where σ is the surface energy due to the interaction of two surfaces.

Using the SE algorithm, the shape of the surface is iterated so as move down the surface energy gradient by calculating the force on each vertex as the negative gradient of the energy. With each iteration, the vertices are moved in direction of the force with a magnitude proportional to the force magnitude. A converged solution was achieved when the meniscus area did not change by more than 0.1% for 50 iterations (Fig. 2.1). Doubling the number of mesh elements resulted in less than a 1% change for all calculations. .
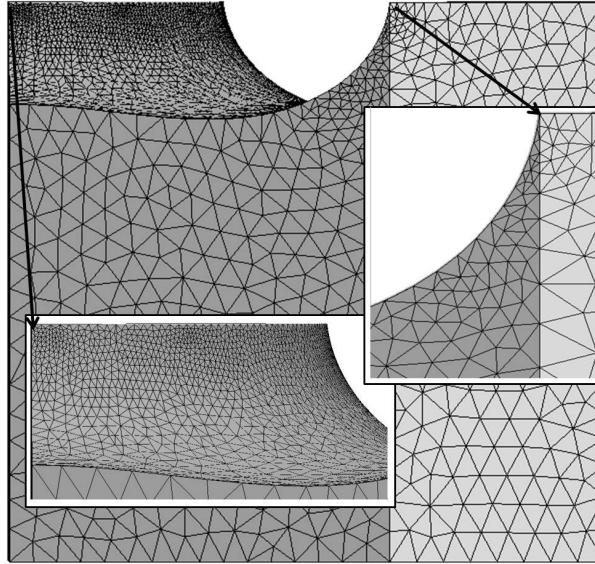
Figure 2.1: Surface Mesh of 3D Fluid Meniscus inside Hexagonally Packed Post Geometry

The surface mesh is smoothed following a similar procedure to that developed by Frommelt [28,29]. This procedure eliminated mesh elements with poor shapes for finite element calculations – this includes mesh elements much smaller than surrounding elements as well as elements with large, scalene angles. This allowed for easier and more reliable import of the mesh structure into COMSOL 3.5a. This was very important for more complicated geometries, such as the 3D meniscus between closely packed spheres. A VRML (Virtual Reality Modeling

19

Language) file containing relevant surface geometry information (vertices and edge data for each

mesh element) was created and exported from SE into COMSOL.

Unit Cell Approach

For hexagonally packed structures, a rectangular unit cell area chosen for wick symmetry is

used for analysis (Fig. 2.2). All four side walls are symmetry planes. This shape was chosen

because its small size (relative to an entire hexagonal array) allowed for relatively fast

computational times while using less computational memory. In addition, the rectangular unit

cell (vs. a triangular unit cell) allows for physically appropriate boundary conditions used in

permeability calculations: including the no-slip BC on the side walls and substrate surface. For

the heat transfer calculations in Chapter 3, the unit cell choice allows for consideration of both

the solid and liquid conduction resistances.
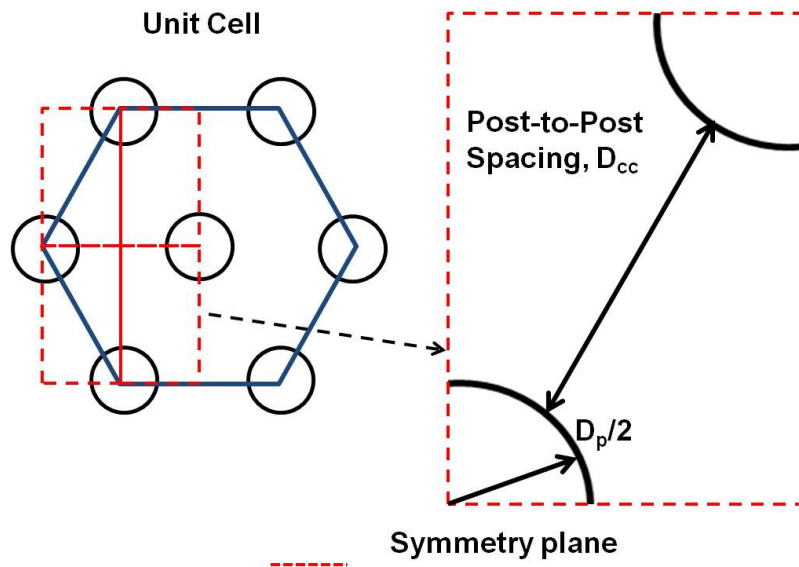
Figure 2.2: Unit cell used for calculation of fluid meniscus shape.

2.3   Permeability

Flow through a porous medium is subject to increased shear stress resistance associated with the higher internal surface area. In the case of complex 3D structures, the effect of the increased surface area and tortuous fluid paths can make computing the flow field difficult. Darcy was the first, in 1856, to measure the bulk resistance to 1D flow through a porous matrix [30]. He found that the resistance to flow for through a porous medium can be described by the equation (Eqn. 2.5) that now bears his name:

$$-\frac{dP}{dx} = \frac{\mu}{K} U_D \qquad (2.5)$$

where P is liquid pressure, K is the permeability, μ is the viscosity of the Newtonian fluid, and U_D is the fluid velocity (volumetric flow rate / bulk channel area) [15]. At low liquid velocities, this definition of permeability can accurately account for the effects of internal surface area, fluid flow path, and other hydrodynamic characteristics. We utilize this definition in our calculations because the Reynolds number of flow through our porous medium in all expected experimental cases is expected to in the range of $Re_D < 10$.

The liquid geometry information, including the 3D liquid meniscus shape, is imported into COMSOL 3.5a for CFD calculations. The fluid unit cell and Navier-Stokes boundary conditions are shown in Fig. 2.3. The micro-posts are assumed to be smooth cylinders. The no-slip boundary condition is applied on all the solid surfaces, and the symmetry condition is applied on the symmetry walls. Since the viscosity of air is much smaller than that of water, the shear stress on the liquid meniscus is negligible. At large heat fluxes, the effect of vapor shear moving in the opposite direction during heat pipe operation may need to be considered, but that effect is ignored here. Any deflection of the liquid meniscus from its equilibrium shape is also

ignored. The normal velocity and the gradients of the tangential velocity in the normal direction

are therefore both set to be zero on the meniscus surface. The pressure difference between the

inlet and outlet is set to match the average flow rates observed in the experiments ($Re_D < 10$).

The steady incompressible Navier–Stokes equation is solved to predict the full 3-D velocity

profiles and the average velocity across the unit cell inlet. From the calculated average velocity

(U_D), the permeability can be determined using Darcy's law.
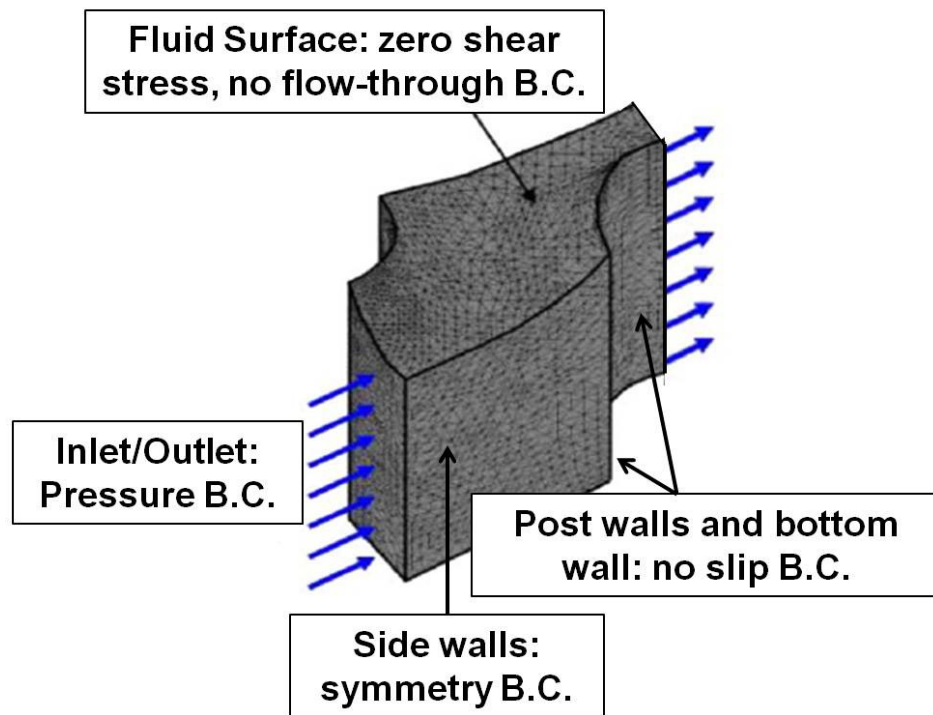
Figure 2.3: Fluid Geometry and Relevant Boundary Conditions used in CFD calculation of

permeability through micro post array.

The effect of the fluid meniscus shape on permeability is shown in Fig. 2.4. At low post

and fluid heights, the relative "flow area" that is inaccessible due to the fluid meniscus can cause

a large decrease in permeability compared to a flat meniscus assumption. As contact angle

increases, this meniscus effect decreases. As post and fluid height increase, the relative effect of the meniscus also becomes smaller.
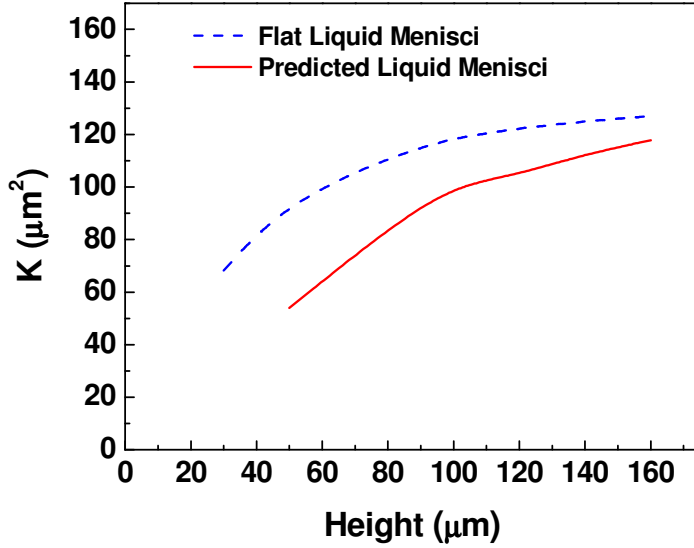
Figure 2.4: The effect of post height and the liquid meniscus shape on permeability for a hexagonally packed array of 50 μm diameter with 100 μm pitch, 7° contact angle.

2.4   Capillary Pressure

A liquid-vapor interface will attempt to minimize the overall system surface energy. If under the influence of surface tension, the result can be a curved interface. The effect of this curvature is normally described as follows (Eqn. 2.6):

$$P_c = \sigma \left(\frac{1}{R_I} + \frac{1}{R_{II}} \right) = \sigma H = \frac{\sigma}{R_{eff}} \quad (2.6)$$

where σ is surface tension (or can also be called $\sigma_{liquid\text{-}vapor}$), H is the curvature (Eqn. 2.7) of the interface and R_I and R_{II} are the principal radii of curvature.

23

$$H = \frac{\frac{d^2\delta}{dx^2}}{\left(1+\left(\frac{d\delta}{dx}\right)^2\right)^{3/2}} \qquad (2.7)$$

In Eqn. 2.8 [27], δ is the position of the meniscus at a given location. For a fluid with zero

contact angle in a easily defined geometry such as a cylindrical tube or a infinitely long channel

with width W, the radii of curvature are well defined: $R_I = R_{II} = R_{tube}$ and $R_I = W/2$ and $R_{II} = \infty$,

respectively. As the contact angle moves away from $0°$, the curvature and capillary pressure

magnitude decrease. For complex geometries, such as those with a 3D nature or a

mathematically complex aspect, determining the radii of curvature can be difficult. Two

examples of this complexity occur in hexagonally packed posts and packed spheres (Fig. 2.5).

These shapes are mentioned because they are studied in detail later in this work.
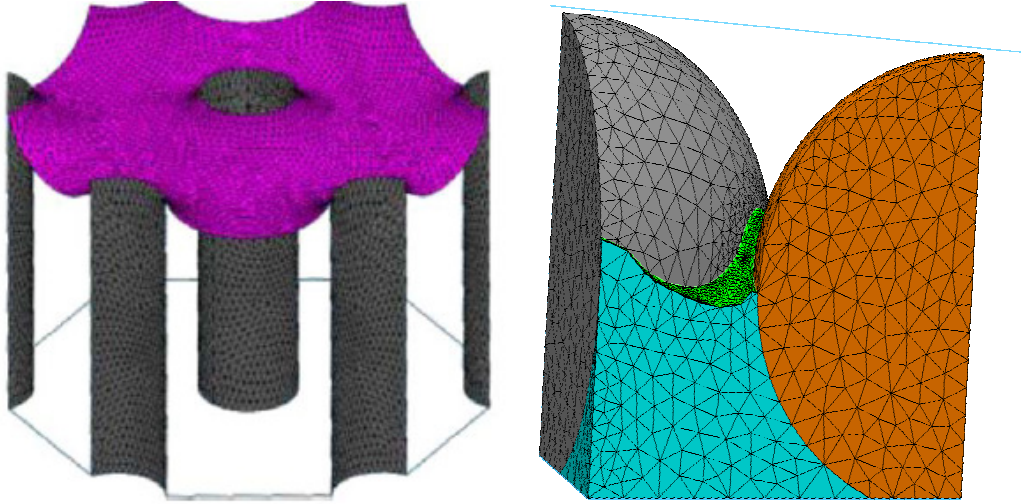
Figure 2.5: 3D meniscus shapes in complex wick structures: hexagonally packed posts (left) and

packed spheres (right).

In an operating heat pipe wick, the liquid pressure should vary both across the wick

surface and within the unit cell. Because there is non-uniform heating the in the evaporation

region, with some areas exposed to high heat fluxes and some areas exposed to near zero fluxes,

an overall pressure gradient should exist across the wick surface to pump fluid to the high

evaporation rate areas. Within the unit cell, a liquid pressure gradient is required to continually

pump fluid to the high evaporation rate interline region (where the fluid layer and liquid side

thermal resistance are smallest). Due to the small thickness of the region, liquid pressure

gradients can be quite large in the interline region, this can affect the meniscus curvature [31,32].

In addition, as the distance between a liquid and solid becomes very small ($\delta < 1$-2 um),

intermolecular forces cause an additional pressure known as disjoining pressure. Previous works

[31-42] have derived models that attempt to account for this pressure and its effect on heat

transfer and liquid flow in the thin film region. Depending on the fluid type (polar vs. non-

polar), differing equations have been found to be accurate. For non-polar liquids [26], Eqn. 2.8

can be used to determine the magnitude of the disjoining pressure. The variable A in Eqn. 2.8 is

known as the modified Hamaker coefficient and accounts for the London-van der Waals force

between the fluid and wall atoms. It is a function of both fluid and solid materials.

$$P_d = \frac{A}{\delta^3} \qquad (2.8)$$

For polar fluids [43], Eqn. 2.9 is often utilized to account for the effect of disjoining pressure

$$P_d = \rho_l RT_\delta \ln[\hat{A}\delta^B] \quad (2.9)$$

where $\hat{A}$ and B are both functions of the fluid and solid materials. The disjoining pressure can

often act to extend the meniscus in the interline region [27]. In this work, the effects of

disjoining pressure are ignored.

2.5   Comparison of Modeling to Experimental Results for Hexagonally Packed Posts

To verify the accuracy of our liquid supply computation scheme, we compare our results to an experiment expressly designed to measure the K/R_{eff} ratio. The experiment is described only briefly here but can be found in greater detail in Chapter 5. An initially dry wick is held in a vertical orientation and dipped into a pool of water. Due to the driving capillary pressure, the fluid is sucked into and up the wick. By analyzing how fast the fluid moves through the wick structure, the liquid supply capability can be calculated. Hexagonally packed posts are utilized as the studied geometry. Only the ratio of K/R_{eff} can be determined due to experimental limitations. Therefore, the predicted permeability (Fig. 2.6) is calculated and used to determine the experimentally measured capillary radius using the K/R_{eff} ratio. Two different cases are studied: first the post diameter is held constant and the spacing is allowed to change, for the second case the spacing is held constant and the diameter is varied. Cylindrical posts with diameters ranging between 30 and 100 μm and spacing between 12.5 and 60 um are studied (see Table 2.1). Post heights are 100 μm. The cylindrical posts are comprised of copper with a super-hydrophilic nano-coating (CuO black oxide, 7° contact angle); the fabrication details are presented in-depth in Chapter 4.

A 7° contact angle is used to describe the relative energies in the Surface Evolver algorithm. The capillary pressure is determined using the mean curvature from the 3D meniscus. Agreement between the experimental and computed capillary pressure results is best at lower solid fractions (Figs. 2.7) for both cases. The discrepancy between the computed and experimental values is thought to be due in part to non-uniformity in the post geometry and

complex micro-scale phenomena not captured by the static meniscus model. At higher solid

fractions, the effect of any non-uniformity in the post diameter or spacing can be quite severe.

Table 2.1: Description of Experimentally Studied Hexagonally Packed Cu Geometries for

Comparison to Modeling Results

Case	D_p (µm)	D_{cc} (µm)	Solid Fraction
I	50	12.5	0.580
		25	0.403
		37.5	0.296
		50	0.227
		65	0.171
II	30	50	0.128
	50		0.227
	75		0.326
	100		0.403
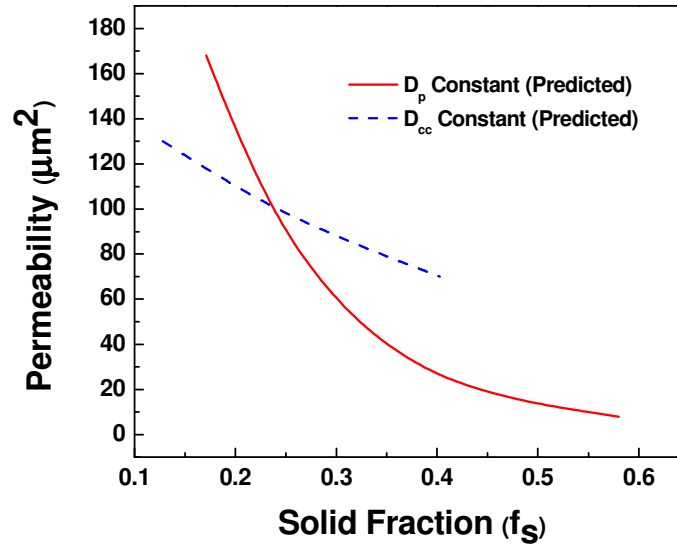
Figure 2.6: Predicted permeability of hexagonally packed posts shown in Table 2.1.
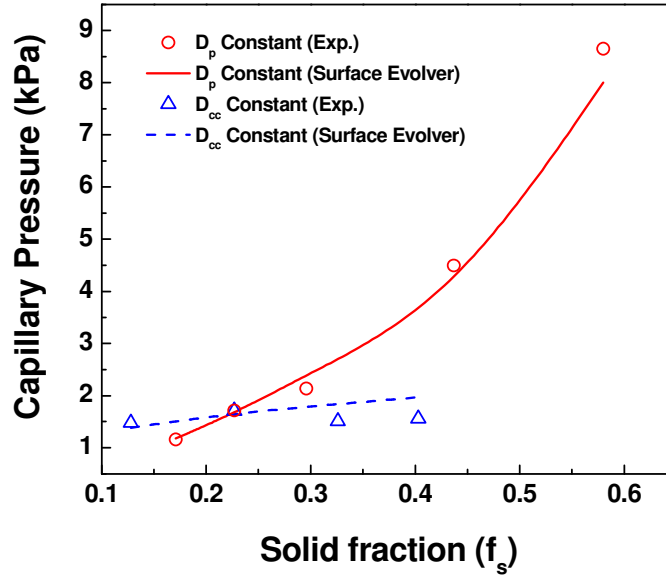
Figure 2.7: Computed vs. experimentally measured capillary pressure values for the hexagonally

packed posts shown in Table 2.1.

The comparison between experimental and modeling results for K/R_{eff} is presented in

Fig. 2.8. Good agreement is found over the wide range of solid fractions. Both cases show

agreement within an experimental error less than 25% between results for all solid fractions.

Except at the high solid fraction range, the discrepancy is typically much lower, within 10% for

most cases. Although the highest capillary pressures are predicted for high solid fraction cases,

the highest liquid supply is found for the low solid fraction case. In both studied geometry

arrangements, solid fraction is shown to be a strong predictor of the liquid supply ability.
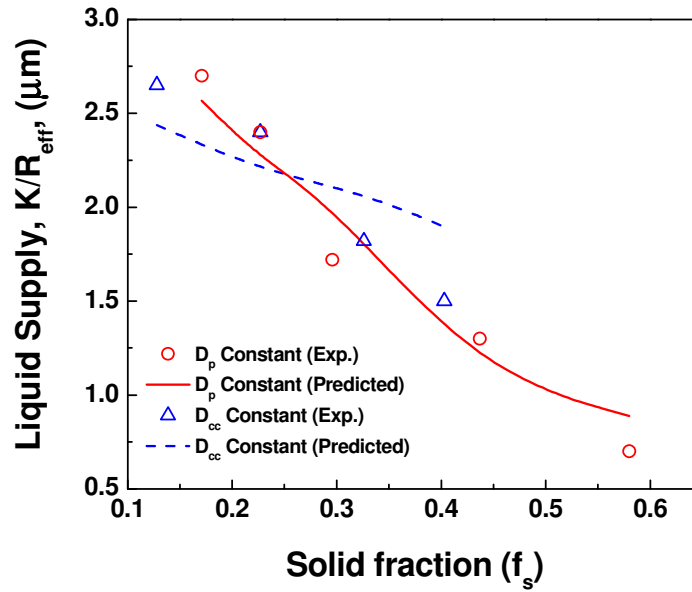
Figure 2.8: Computed vs. experimentally measured liquid supply values for the hexagonally packed posts shown in Table 2.1.

2.6   Summary

A surface energy minimization algorithm is utilized to determine the 3D meniscus shape resulting from a complex geometry. Capillary pressure is determined by computing the meniscus curvature. Liquid permeability is predicted by determining the average flow velocity through a unit cell of fluid. When compared to the rate-of-rise experiment involving hexagonally packed posts, the modeling method proves accurate over a range of solid fractions and post geometry variations. The agreement between results provides validation to our modeling efforts. The work presented in this chapter can be used to optimize the liquid supply of our fabricated wick structures.

The main conclusions reached in this chapter were as follows:

1. A surface energy algorithm was used to compute the 3D meniscus shape

2. Permeability and capillary pressure, directly related to the maximum heat flux by the K/R_{eff} ratio, can be computed using the 3D meniscus shape.

3. Liquid supply is a strong function of solid fraction for the studied geometry cases.

4. The largest K/R_{eff} ratio was found for geometries with small solid fractions.

5. The modeling results were validated by comparison to experimental results for hexagonally packed, super-hydrophilic, circular posts.

CHAPTER 3

Computational Modeling of Effective Heat Transfer Coefficient

The evaporator region of a heat pipe or vapor chamber can be responsible for a large portion of the thermal resistance. The heat transfer in the evaporator region consists of solid and liquid conduction, convection, and evaporation.   Here we present our work model for the effective heat transfer coefficient in a micro-structured wick. A static meniscus assumption is made in which the shape of the liquid-vapor interface is assumed constant. This assumption limits the validity of the modeling to the low heat flux regime where complexities such as localized boiling or dry-out are non-existent. The complex, static fluid meniscus geometry is calculated using a surface energy minimization algorithm and a commercially available 3D finite element solver is used to compute the effective heat transfer coefficient. We present our results for the effective heat transfer coefficient of hexagonally packed copper posts as well as a comparison to experimental results. Heat transfer coefficients on the order of 10 W/cm^{2}K are predicted and our results are validated by comparison to our experimental data. Good agreement between the experimental and predicted results for a static meniscus contact angle of 30 - 50°. The work presented here can be used to decrease the thermal resistance in a wick evaporator.

3.1   Background

Previous modeling of heat pipe performance has focused predominately on the entire heat pipe (evaporator, condenser, and vapor space) to determine critical heat flux [31,44]. Detailed work on the evaporator region has been performed previously for triangular grooves [33,34], micro-channels [35], flat surfaces [36,37], inclined surfaces [38], and spheres [39,45]. Ranjan et al. [23,46,47] computed the 3D meniscus shape and determined that certain wick geometries

allow for better heat transfer performance because of the amount of high evaporation rate thin film or interline area.

Here, a novel method is presented for analyzing the effect of complex microstructure wick geometries on thermal resistance. The Surface Evolver algorithm is used to determine the equilibrium meniscus shape that results from the surface tension interaction between the fluid and the solid micro-structure geometry. This equilibrium fluid geometry is imported into a commercial finite element solver and merged with the solid wick structure. Heat transfer through the fluid and solid geometry is analyzed considering a simple conduction and evaporation model. A heat transfer coefficient (h_{eff}) definition is utilized so that the effect of wick geometry and meniscus shape on heat transfer can be analyzed and compared to experimental results.

3.2   Effective Heat Transfer Coefficient Definition and Calculation

In order to quantify the effect of the thermal resistance in the wick area, modeling is performed on a unit cell (presented in Chapter 2). This choice allows the inclusion of all the important thermal resistances present in a wick evaporator. The heat flow path in the evaporator region includes solid conduction resistance through the wick structure, liquid conduction resistance through the liquid layer, and an evaporation resistance at the liquid-vapor interface (Fig. 3.1). Other heat transfer mechanisms can include convection and boiling. These additional mechanisms can be ignored at low heat fluxes [46,47]. Thermal spreading through the pipe or chamber walls is significant because the thickness of the wall can be much greater than the height of the wick geometry and typically highly thermally conductive materials are used.

Since the thermal conductivity of liquid, k_L, is typically much lower than that of the solid structure, k_s, most of the heat flow will occur in regions where the fluid thickness, δ, is small. For this reason, knowledge of the 3D meniscus shape is important for accurate determination of the effective heat transfer coefficient.
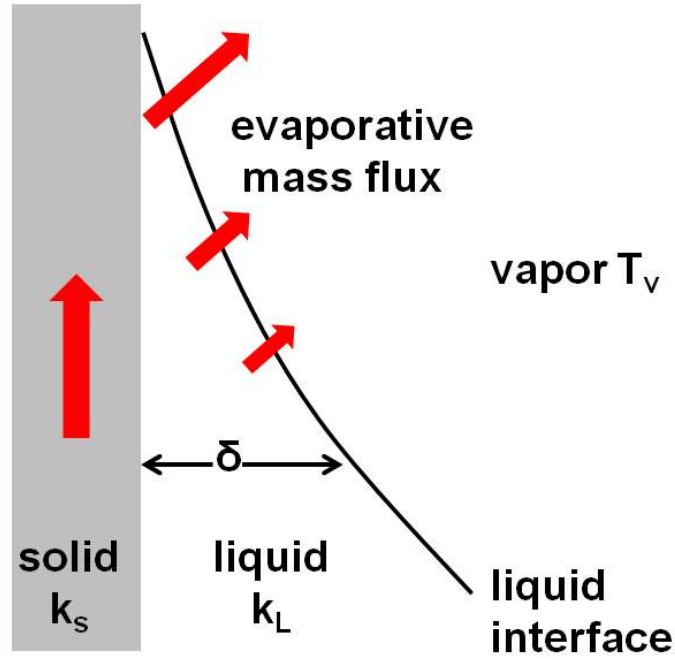
Figure 3.1: Heat transfer in the thin meniscus region – due to the typically high k_s/k_L ratio, the majority of heat transfer will occur where δ is small.

We use a definition for effective heat transfer coefficient (Eqn. 3.1) that accounts for the thermal resistance of the wick+fluid combination without including spreading in the substrate or casing (Fig. 3.2). This method was chosen so as to best account for the effect of solid geometry (height and shape) and solid structure thermal conductivity. Hence, the effective heat transfer coefficient is defined as:

$$h_{eff} = \frac{q''}{T_{wall} - T_v} \qquad (3.1)$$

33

where T_{wall} is the temperature at interface of the substrate-wick structure (Fig. 3.2) and q" is the input heat flux to the unit cell.
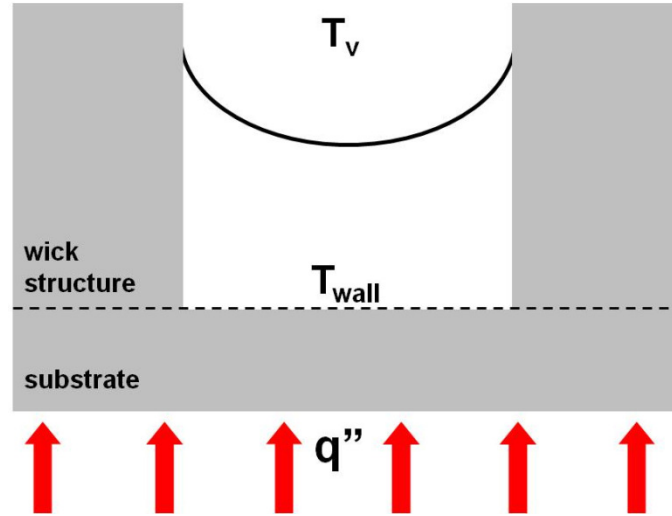
Figure 3.2: Schematic for definition of Effective Heat Transfer Coefficient

3.3   Static Meniscus Effective Heat Transfer Coefficient Calculation

The surface mesh of the solid posts of the microstructure was created simultaneously in the Surface Evolver program and merged to the fluid body so that heat transfer through both the liquid and solid are considered. For the experimentally tested wick, the substrate thickness was much greater (~5x) than the height of the post, allowing the thermal energy to spread from the bottom of the substrate to the posts. This effect is modeled by a small solid substrate of near-infinite thermal conductivity at the bottom of the posts.

Boundary conditions are used to enforce symmetry and heat transfer conditions (Fig. 3.3). An input heat flux, $q_{in}^{"}$, is specified at the bottom of the evaporator substrate. An insulation boundary condition is used to enforce symmetry on the side planes of the fluid and structure body. Insulation is assumed on the un-wetted portion of the post (top of post is assumed to not wet). The heat transfer coefficient determined in Eqn. 3.2 is used for the fluid-vapor interface boundary condition. All physical parameters are known and assumed constant. T_{lv} is approximated as T_v in the *a* and *b* terms in Eqn. 3.2 with negligible impact on results. The interface heat transfer coefficient (Eqn. 3.3) is a function of temperature due to the pressure term.
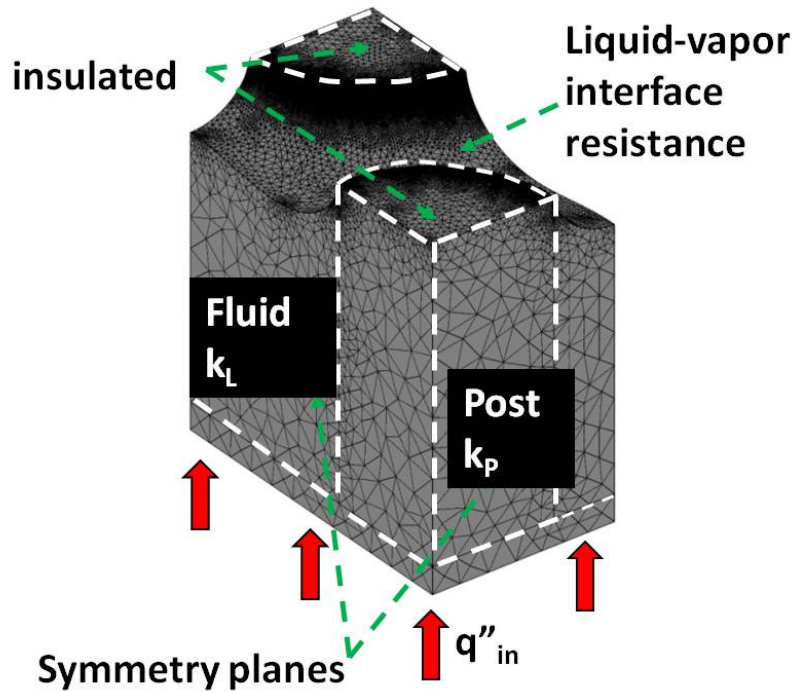
Figure 3.3: Finite element effective heat transfer coefficient and relevant boundary conditions.

Liquid-Vapor Interface Resistance

For most applications, ignoring the transport resistance due to the liquid-vapor interface leads to negligible error. For fluid thicknesses on the order of a few microns, the transport resistance can be of the same order as the conduction resistance of the liquid film. An appropriate mass flux condition at the fluid-vapor interface is required to accurately determine resistance to heat transfer [27]. Wayner derived a quasi-thermodynamic solution based model for mass flux at a liquid-vapor interface (Eqn. 3.2) [32]:

$$m^{''} = a(T_{lv} - T_v) - b(P_v - P_l) \qquad (3.2)$$

$$\text{where } a = C\left(\frac{\bar{M}}{2\pi\bar{R}T_{lv}}\right)^{1/2}\frac{P_v\bar{M}h_{fg}}{\bar{R}T_vT_{lv}} \text{ and } b = C\left(\frac{\bar{M}}{2\pi\bar{R}T_{lv}}\right)^{1/2}\frac{P_vV_l}{\bar{R}T_{lv}} \text{ and } C = \frac{2\hat{\sigma}}{2-\hat{\sigma}}$$

The accommodation coefficient, $\hat{\sigma}$, describes the fraction of vapor molecules which cross the liquid-vapor interface due to either evaporation or condensation as opposed to molecular reflection off the interface. Experimental studies suggested that the accommodation coefficient may vary greatly depending on the material systems and surface contamination [27,48]. Smaller values of the accommodation coefficient would increase the liquid-vapor interface resistance, which in turn increases the relative importance of the liquid-side conduction resistance. Mills experimentally showed that for clean water, no interface resistance was measured during condensation, implying that the accommodation coefficient is greater than 0.45 [49]. As in previous works, an accommodation coefficient of one is assumed for clean water [50]. The effective heat transfer coefficient is shown to not be noticeably affected by changing values of

the accommodation coefficient between 0.5 – 1. Table 3.1 shows the properties of water utilized

in our calculations [51].

A heat transfer coefficient on the liquid surface can then be defined as:

$$h_{lv} = \frac{m'' h_{fg}}{(T_{lv} - T_v)} \qquad (3.3)$$

where T_{lv} is the temperature at the interface.

Table 3.1: Relevant Properties of Clean Water [51] for Interface Resistance Model.

M	18.02 g/mol
h_{fg}	2.39×10^3 kJ/kg
P_v	8.6 kPa
V_l	1.82×10^{-5} m^3/mol
σ	69 mN/m^2
k_{Si}	148 W/mK
k_{Cu}	390 W/mK
k_l	0.63 W/mK
$\hat{\sigma}$	1

The Surface Evolver algorithm is appropriate for determining static meniscus shapes.

Evaporation on a microstructure surface is inherently dynamic process which involving large

liquid pressure drops through thin film regions. In addition, phenomena such as Marangoni flow

or bubble generation are not considered. The analysis presented can be used as a convenient

method of determining the effect of the solid and liquid interaction affects the heat transfer

performance at low heat fluxes.

3.4 Comparison of Static Meniscus to Experimental Results for Hexagonally Packed Posts

We validate our modeling efforts by comparing to experimental data. We use a hexagonal post array of super-hydrophilic Cu wicks (described in detail in Chapter 4). The experimental conditions and data analysis method are described in thoroughly in Chapter 5.

In order to determine the valid range at which the static meniscus assumption is appropriate, the experimental heat transfer performance is studied at low fluxes. In analyzing $h_{app} = q_h''/(T_h - T_v)$ for a range of heat fluxes, q_h'' values > ~35 W/cm^2 result in decreasing thermal performance (Fig. 3.4). This static meniscus modeling method produces the heat transfer coefficient for low heat fluxes (<35W/cm^2), an important limitation since only the static meniscus shape is considered.
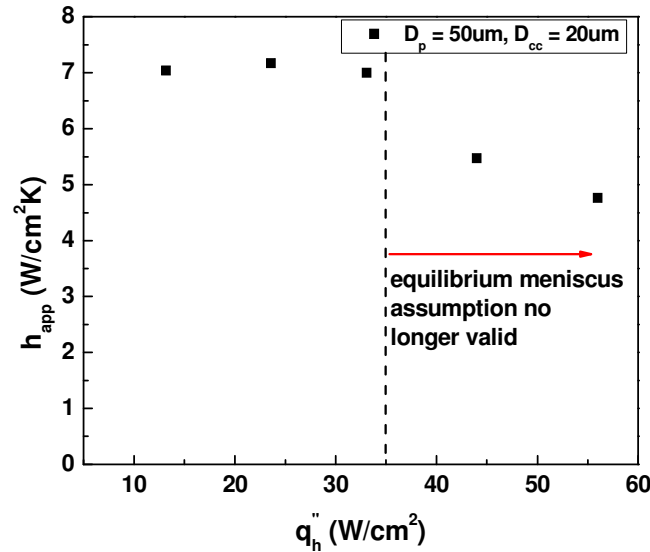
Figure 3.4: h_{app} = q"$_{heater}$ / (T$_{heater}$-T$_{vapor}$) showing increased thermal resistance for heat fluxes >35W/cm^2.

38

The predicted h_{eff} from the simulation for a contact angle of 35° - 50° matches the

experimental data closely for a range of solid fractions (Fig. 3.5). This agreement shows the

validity of assuming an equilibrium meniscus for h_{eff} modeling at low heat fluxes. The error bars

represent the standard error of h_{es}. At large h values, h_{eff} is highly sensitive to the heater

temperature: as high as 2.7 (W/cm²K)/K. Although the complexities associated with heat

transfer in a thin meniscus region are complex, our results show that in the cases of super-

hydrophilic circular posts with diameter on the order of 50 μm, we can account for the

complexities by assuming a fluid interface shape corresponding to a static contact angle of ~ 35°

- 50°.
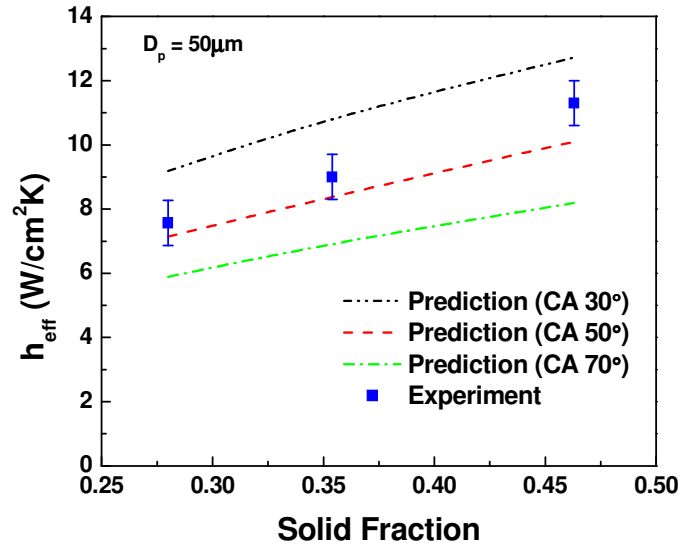
Figure 3.5: Experimentally determined h_{eff} vs. prediction from static meniscus model for a range

of solid fractions.

In order to develop an optimized wick structure, a more in-depth analysis of the static

meniscus heat transfer results is undertaken. Most of the liquid-side heat transfer is found to

occur in the thin film region, or interline region in which the film thickness is < 2-5 um. This is because the thermal conductivity of water ($k_L \sim 0.6$W/mK) is much lower than that of the solid material (in this case, Cu, $k_{Cu} \sim 390$ W/mK). The interplay between these two thermal resistances can be seen in Fig. 3.6, where an increase in solid fraction may result in either a decrease or increase the heat transfer coefficient.
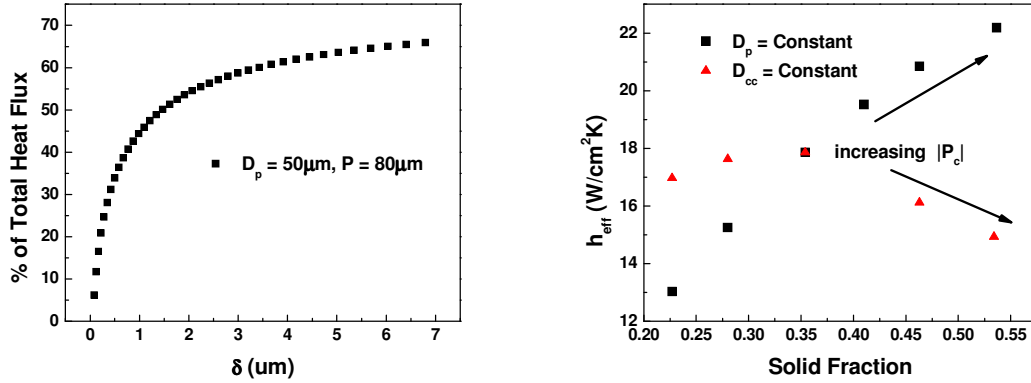
Figure 3.6: Left Side: Percentage of total heat flux through the meniscus at fluid thickness δ. Right side: Modeling results showing that solid fraction is not always a good predictor of h_{eff}. Both presented results correspond to a static contact angle of 7°.

For high thermal conductivity structures, a better predictor of performance may be the normalized thin film area (Fig. 3.7). The normalized thin film area is defined as the portion of the fluid meniscus within 2 μm of the solid surface normalized by the unit cell base area. For the Cu + water combination analyzed here, the solid thermal conduction resistance is much less important than the liquid conduction resistance. Thus, increasing the normalized thin film area leads to increasing the predicted heat transfer coefficient. However, as the solid thermal

conductivity resistance increases, both types of conduction resistance become important and must be considered.
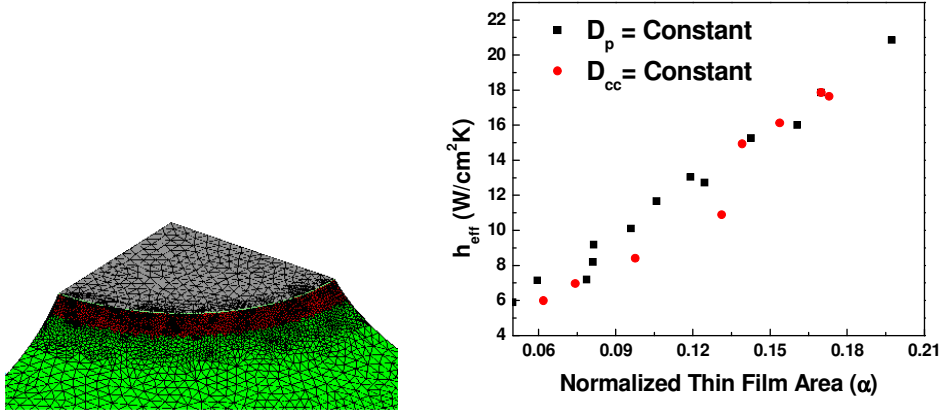
Figure 3.7: Left Side: Mesh of the meniscus region near a circular post; the dark region is the thin film region ($\delta < 2\mu m$). Right side: h_{eff} as a function of normalized thin film area for Cu structures.

3.5   Summary

A static meniscus simulation was developed as a means of predicting heat transfer performance at low heat fluxes by accounting for conduction and evaporation resistances. A hexagonal post array with varying solid fractions was used as the sample geometry.   Heat transfer performance, defined as h_{eff}, was predicted for various solid fraction and contact angles. The simulation results were compared to experimental results and strong agreement was observed over a range of solid fractions for a contact angle range of 35° - 50°, validating the modeling method for low heat fluxes. This method of analyzing heat transfer in the evaporator region can be used as a tool for optimizing wick heat transfer performance. The main conclusions reached were as follows:

41

1. The equilibrium meniscus assumption is validated by comparison to experimental data for $q_h^{"} < {\sim}35$ W/cm^2.

2. A large percentage of heat transfer (~50%) is shown to occur within the thin meniscus region ($\delta < 2$ μm) for low contact angles.

3. Small contact angles result in the largest heat transfer performance. h_{eff} varies between 6 – 20 W/cm^{2}K for contact angles ranging between 90° - 0°, respectively.

4. Solid fraction is not a good indicator of thermal performance because it does not account for how the fluid interacts with the solid geometry.

5. For higher thermally conductivity solids (i.e. Cu) and moderate aspect ratio structures, the normalized thin film area, α, is shown to be an excellent parameter for predicting thermal performance over a range of solid fractions and contact angles.

CHAPTER 4

Wick Fabrication

Three different fabrication techniques are utilized to create thin (30 – 200 μm) wick

structures. A monolayer of Cu spheres is constructed using traditional sintering techniques. The

other two techniques – Si etching and Cu electroplating deposition - are based on a hexagonally

packed geometry. Silicon wicks are fabricated using a Bosch-type etching method. Because of

the high amount of process control, complex 3D structures are fabricated with aspect ratios as

high as 24 for posts diameters of 10 μm. Copper wicks structures are grown via an electroplating

method and heights of 120 μm are achieved. However, limited fabrication process control limits

the maximum aspect ratio to approximately 5. For both the Si and Cu structures, the wettability

is increased using either a thermal or chemical oxidation scheme, respectively, to change the

surface chemistry and roughness. Gold thin film heaters are also fabricated using traditional

techniques and are utilized during experimental testing because of their small size, excellent

reliability, and ease of use.

4.1   Background

Traditional wick fabrication methods typically utilize one of three different

manufacturing methods (Fig. 4.1) – sintered spherical particles, wire mesh, or machined grooves.

Though these methods are used to manufacture commercially available heat pipes and vapor

chambers, they suffer from two different characteristics: limited machining precision and a

complex 3D shape. For example, sintered spheres often suffer from sample heterogeneity –

either in particle size distribution due to sieving processes or in necking ratios due to

complexities associated with particle packing [52]. Wire mesh must also be sintered together to

ensure good thermal contact between mesh layers and to the substrate [53]. However, mesh size options are limited by manufacturing constraints. In addition, although atomic diffusion can occur at any temperature, typical sintering temperatures take place at well over half the material's melting temperature [54]. These high temperatures can be unsuitable for certain substrates or casing materials. Machined grooves can typically only approach thickness and heights that are on the order of a few hundred micron – achieving smaller length scales is difficult [25,55]. In addition, high precision of machined grooves at small length scales (< 200 μm) can be problematic and expensive.

More recently, wick structures consisting of micro-fabricated or multi-level structures have been studied. Cai and Chen fabricated structured rows of carbon nano-tubes using CVD at 670°C [58] (Fig. 4.2A,B). Ding et al. fabricated micro titanium posts with nano-structured titanium hair to increase wettability [59] (Fig. 4.2C,D). The Ti was etched using an inductively coupled plasma gas and the nano-hairs were grown in a hydrogen peroxide solution. Multi-length scale Cu sphere structures ("bi-porous") (Fig. 4.2E) were tested by Semenic [53]. These structures were fabricated by sintering similar sized (<100 μm) Cu particles together, breaking the sintered mass into clusters (<1000 μm), and then sintering the clusters together to form a "bi-porous" structure with pore sizes on the order of both particle and cluster. These biporous clusters can then be used alone as a wick structure or integrated with a thin evaporator region, as done by Reilly et al. [60]. Nam constructed Cu posts with an integrated CuO nanostructure in a method similar to that presented in this work [62].
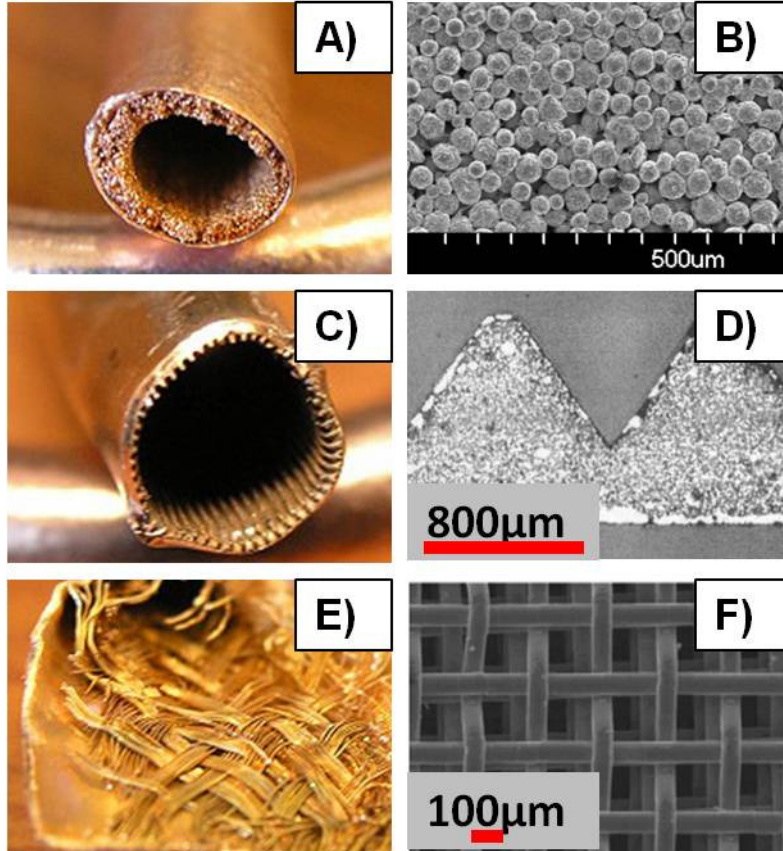
Figure 4.1: A) and B) Sintered Cu particle heat pipe wick [57] and SEM image of same; C) and D) Triangular groove heat pipe [57] and corresponding SEM image [57]; E) and F) Wire mesh wick [57] and SEM image [53].

Heater devices used to mimic high heat flux components typically consist of Cu blocks with inserted cartridge heaters [52,53,63,64]. The voltage or current through the heaters is controlled and then resulting thermal energy flow is typically funneled to a narrow neck which is soldered, pasted, or brazed to the wick substrate. While this can be a reliable heat flux input method, cartridge heaters and the corresponding Cu blocks can be large, expensive, and prone to heater failure. In addition, the large heat fluxes required in testing heat pipe wicks often leads to very high temperatures in the Cu and heater. In this work, we make use of thin, micro-fabricated

heaters which can dissipate large heat fluxes in a small form factor which can be readily and easily attached to the backside of our wick substrate using solder bonding.
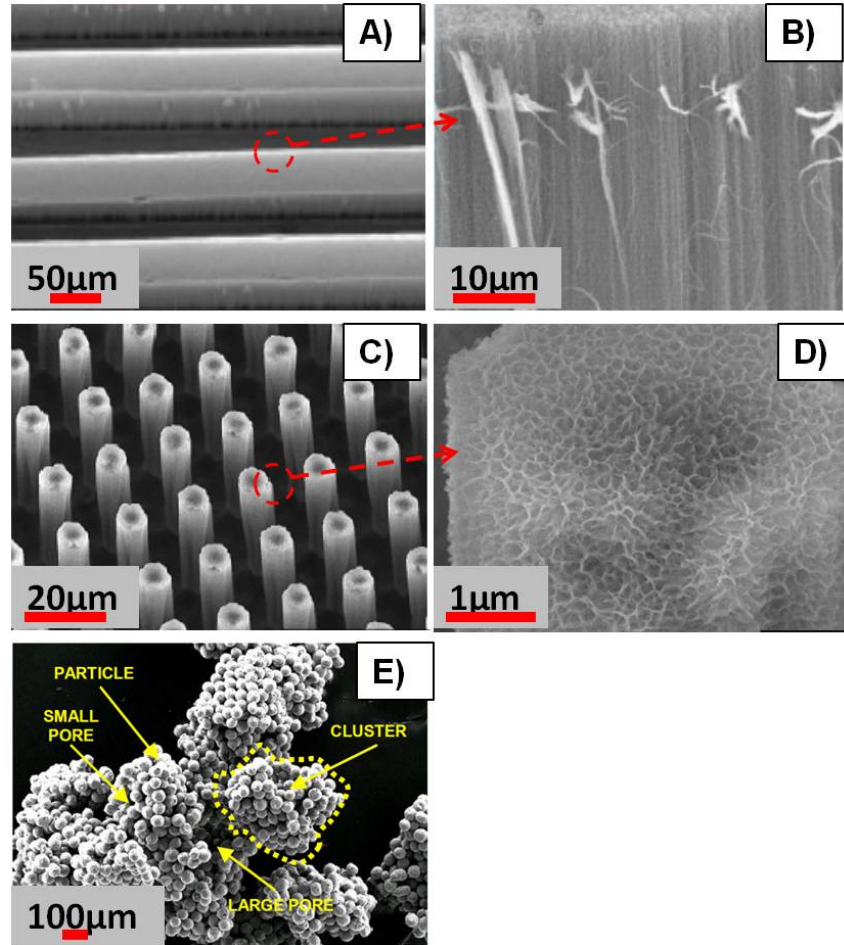
Figure 4.2: A) and B) SEM images of Bi-level CNT wick [58]; C) and D) images of etched Ti posts and nano structured Ti "hairs" [59]; E) Biporous cluster consisting of large groups of sintered smaller particles [65].

In this work, thin evaporator structures with heights on the order of 30 – 200 μm are fabricated. These structures can be integrated with a thicker liquid supply layer or can be used on their own to act as a very thin vapor chamber wick. Using micro-machining techniques,

precisely controlled sample geometries are created – making comparison to our static meniscus model comparison easier and less prone to problems associated with geometrical complexities.

4.2 Sintered Copper Particle Monolayer

Sintering Cu particles together is a well-established practice and is often utilized for fabricating heat pipe wick structures. Sintering is a high temperature process (typically greater than one-half the material melting temperature) in which the molecules of a material diffuse so as to lower the overall surface energy. The amount of diffusion is proportional to both sintering time and temperature. Copper is a common heat pipe material due to its high thermal conductivity and compatibility with water (typical sintering temperature ~800 - 1000°C [52,66], melting temperature of 1084°C [18]).

In this work, the monolayer wick samples are prepared by Advanced Cooling Technologies located in Lancaster, Pa. The Cu particles are sieved and then combined with a solvent and spread on a 500 μm thick Cu substrate (3cm x 3cm area) to form a monolayer. Three different average particle diameter samples are studied: 29, 59, and 71 μm. The samples are then sintered in a hydrogen furnace for 1 hour at 960°C. These samples are described in greater detail in Chapter 6.

4.3 Etched Silicon

Manufacturing heat pipe wicks out of silicon (Si) was chosen so as to make use of its moderate thermal conductivity (k_{si} ~ 120-150 W/mK [18]) and compatibility with micro-manufacturing techniques. Very high aspect ratio structures (see Fig. 4.4) can easily be obtained by selectively etching the Si substrate. In addition, Si and SiO_2 are compatible with water.
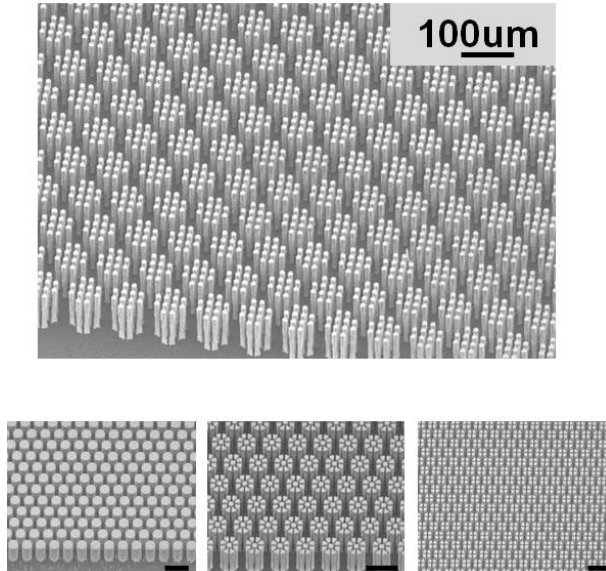
Figure 4.3: SEM images of high-aspect ratio, etched Si wick structures (height of 240um, scale bar in all images of 100 μm). From large top photo, clockwise: cluster geometry, pie, sun, and baseline-post. All structures are hexagonally packed.

A four inch diameter, 500 μm thick, single side <100> wafer with a 1.3 μm thermal oxide layer was used as the base substrate. Four wick samples were fabricated on each wafer. A photoresist layer (AZ-5214) patterned using conventional lithography techniques acted as a positive mask (Fig. 4.5 shows process flow). This mask allowed selective thermal oxide etching in an STS-AOE oxide etch chamber. Any remaining photoresist was removed using an acetone sonication bath. The silicon was etched using a Bosch style process in a Fast Deep Reactive Ion Etching (fDRIE) chamber (etch rate of ~5μm/min). Etch depths as high as 240 μm were achieved for structures with nominal diameters on the order of 10 μm. The sample was then cleaned using Piranha solution (Sulfuric acid and hydrogen peroxide) to remove any organic contaminates. Any remaining oxide was removed by a Hydrofluoric acid bath (49%

concentration). The sample was then placed in a high temperature furnace in an O_2 environment (dry oxidation) at 1100°C for approximately 1 hour to grow a conformal thermal oxide layer on the order of 100-150 nm over the entire sample and wick structure. The oxide layer increased the wettability of the wick structure due to its high surface energy (vs. that of bare Si). A 30 nm Ti layer + 350 nm Cu layer was then evaporated onto the backside of the Si wafer for heater chip soldering. The sample was diced using mechanical cracking.

500 µm Si + 1.3um oxide

Photoresist Mask

Oxide Etch

Deep Si Etch

Furnace 100nm Oxide
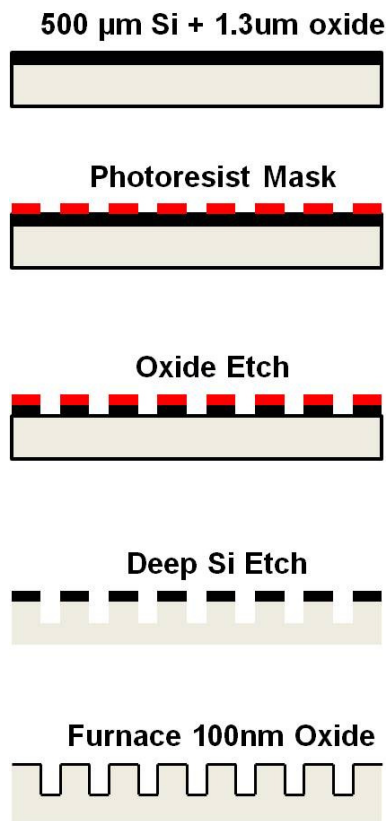
Figure 4.4: Process Flow for Etched Si Wicks using SiO_2 as mask.

4.4 Electroplated Copper

Cu wick structures were fabricated to make use of copper's relatively high thermal conductivity (k_{Cu} = 390 W/mK at ~300K [18]). A four inch diameter, 500 µm thick Si wafer

<100> was used as a substrate (see Fig. 4.6). A 30 nm Ti adhesion layer, followed by a 350 nm Cu seed layer, and another 30 nm Ti layer for Cu protection were evaporated onto the Si substrate. A thick photoresist mold (KMPR 1050, MicroChem Corp.) was patterned using typical lithography techniques to fabricate an electroplating mask. Depending on the size of the plated structures, photoresist molds varied in thickness between 100 – 150 μm. After the electroplating mold was deposited, the top Ti layer was etched using a 1% HF solution. The wettability of the mold was increased by placing it an O_2 plasma gas at 250 mTorr pressure at 175W power.

Cu was then electroplated by placing the sample in an electrolyte solution (Technic Copper FB Bath RTU: 5-10% Cu Sulfate + 15-20% Sulfuric Acid + Di water) with a current density of approximately 5mA/cm^2, corresponding to a deposition rate of approximately 6 μm/hour. The mold was then removed using a series of KMPR lift-off and dissolving chemicals (MicroChem XP Remover A and B, Neutralizer, and Remover PG). The remaining Ti layer was etched away using a 1% HF solution.

In order to increase the wettability of the bare Cu wick structure (Fig. 4.7), a chemical oxidation scheme was utilized to grow a high surface energy CuO nanostructure on the wick surface. The chemical solution consisted of 3.75g of NaClO2, 5.0g of NaOH, and 10.0g of Na3PO4*12H2O in 100mL of de-ionized water held at 95°C. The sample was immersed for approximately 5 minutes and the self-limiting 3D oxide structure grew over the entire wicks surface (Fig. 4.8). More details on this and other similar oxidation schemes and processes can be found in [67].
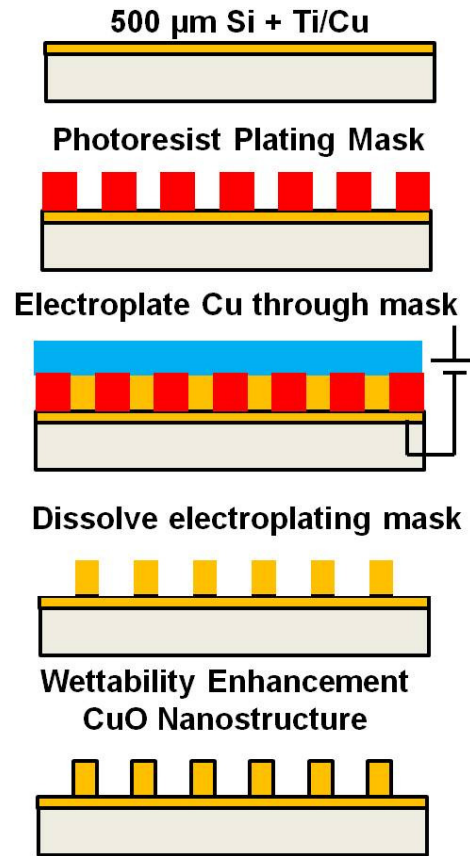
Figure 4.5: Process flow for Electroplated Cu wicks.
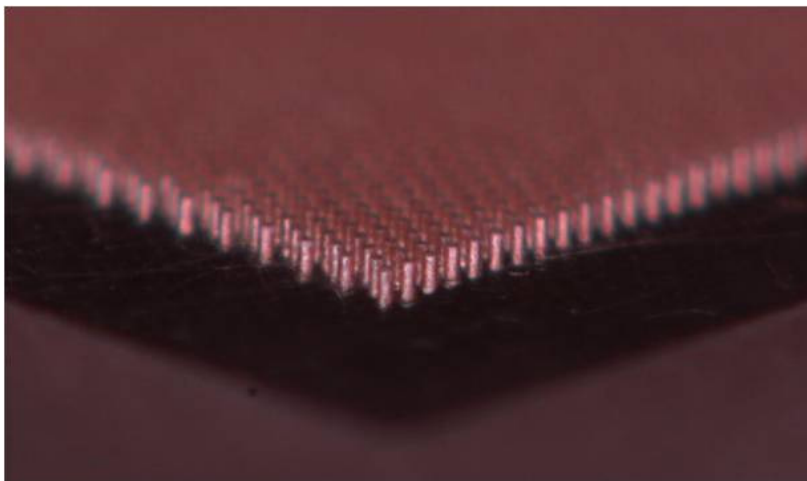
Figure 4.6: Bare Cu wick structure after electroplating mold removal.
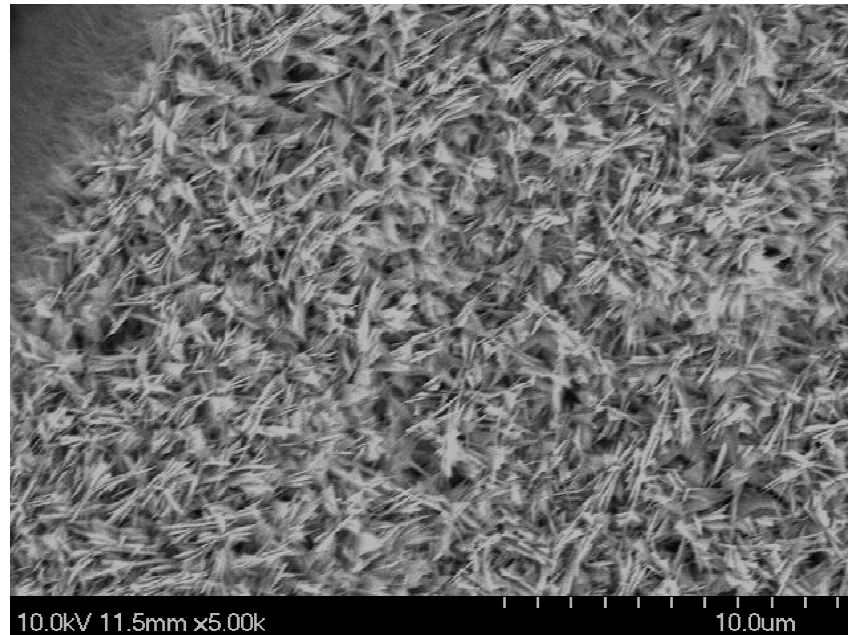
Figure 4.7: SEM image of 3D nano-structure on Cu wicks – a self-limiting chemical oxidation scheme was used to build these sharp, high surface energy, hydrophilic structures.

4.5   Thin Film Heater Chip

Thin film heater chips were chosen to mimic an actual electrical component by providing an input heat flux. These chips were used because of their ease of manufacturing, ease of replacement, small size, and well known properties for thermal characterization. Chips were either fabricated (Fig 4.9) on a 100 μm Si wafer (with a 100nm thermal oxide layer, 3" wafer) or a polished 250 μm AlN (aluminum nitride) substrate (Stellar Industries, 4" polished AlN). These substrates were chosen for their high quality surface finishes as well as their relatively high thermal conductivities: k_{si} = 130 W/mK [18], k_{AlN} = 170 W/mk [68,69]. A thin chrome layer (10 nm) was evaporated onto the polished side of the substrate followed by a 125 nm gold layer. A serpentine heater pattern was then chemically etched into the gold using a photoresist mask in

52

conjunction with chrome and gold etchants. The backside of the heater was also coated with a

30 nm chrome layer and a 350 nm copper layer for soldering to our wick substrate. The samples

were protected on both sides using a layer of dicing tape and then diced into individual chips

using a diamond saw (Fig. 4.10). The tape was removed in an acetone bath.

The serpentine gold layer acted as an electrical resistor – typical resistance values were in

the range of 500 – 600 Ω for a 5 x 5 mm^2 heater area. Four solder pads enabled a four point

probe measurement technique in which two of the pads were used to provide power to the heater,

and the other two pads were used to sense the voltage across the serpentine heater.

250 um AlN or 100um Si

10 nm Cr+ 125nm Au

Photoresist Mask

Etch Au & Cr

Dice Sample

Backside Cu

Figure 4.8: Process Flow for Heater Chip Fabrication.
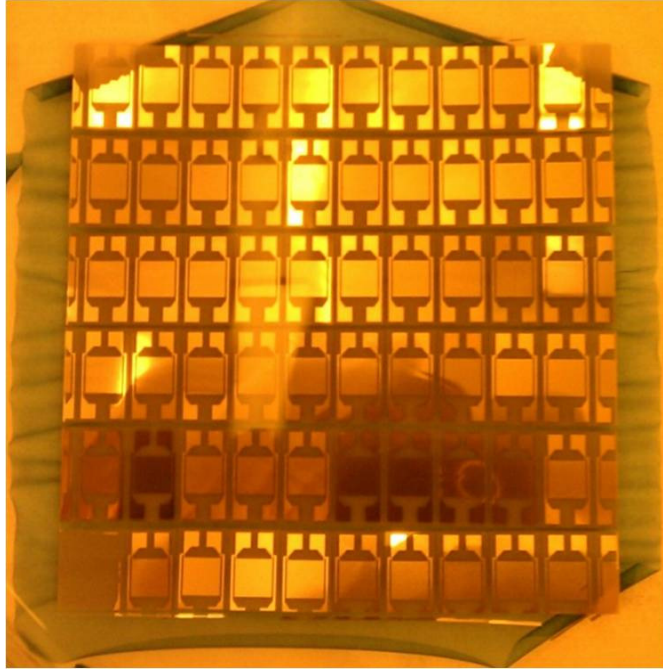
Figure 4.9: "Bulk" Processing of 5x5mm^2 Au Serpentine heaters with solder pads. Photo taken right after dicing step while protective dicing tape still attached.

4.6   Summary

Three different methods are utilized for wick structure fabrication. The first is a monolayer of Cu spheres which were bonded to the substrate via a sintering process. The second is a well controlled Si etching which allowed high aspect ratio structures and was also integrated with and SiO$_2$ surface to increase wick wettability and liquid supply. The third method consisted of electroplating copper through a thick mold to fabricate structures with an aspect ratio as high as five. The electroplated copper could then be covered with a high surface energy CuO nanostructure to increase wick liquid supply. Finally, thin film heaters consisting of thin (125 nm) gold serpentine resistive elements on Si or AlN substrates were fabricated to provide an easy to characterize experimental heat source.

54

CHAPTER 5

Experimental Setups

In this chapter the experimental setups and methodologies used in gathering and recording data for the liquid supply and heat transfer performance characterizations are described. In order to make fair and accurate comparisons to our modeling methodologies (presented in Chapter 2 and 3), accurate characterization of the wick performance is needed. Water is used as the working fluid in all cases to make use of its high Merit number and ideal properties for heat pipe operation. To determine the wick's liquid supply capability, a rate of rise experiment is used in which a dry wick is held in a vertical orientation and then dipped into a pool of liquid. The advancing liquid front is tracked and can be used to determine the wick's ability to supply fluid to the hot spot or evaporator region. The heat transfer performance is measured in well-controlled Cu vacuum chamber is utilized for thermal and pressure control. The wick is held in a vertical orientation and allowed to self-saturate. A thin film heater is soldered to the backside of the wick substrate and thermocouples located along the substrate and heater are used to measure temperature as a function of input heat flux.

5.1   Background

Careful and accurate wick characterization is necessary for meaningful model comparisons. The complex phenomena occurring in a functioning heat pipe wick can be strong functions of the wick's properties: structure shape and morphology, thermal conductivity, liquid permeability, vapor permeability, and capillary pressure. Characterizing the performance of a porous wick structure in terms of liquid supply and heat transfer performance can be difficult due

to the small size scales and complex geometries involved. For the geometries presented in this work, we focus on liquid supply (permeability and capillary pressure) and heat transfer performance. Numerous studies have looked at these properties; a summary of previous experimental work by other researchers is presented below.

Liquid Supply in Porous Media

Liquid permeability in porous media describes how conducive the media is to flow through it. Various fields of research, such as hydrogen fuel cells, oil pumping, and geology [15], study the complex nature of fluid flow through tortuous porous media. In all cases, flow through the pores results in pressure losses associated with viscous and pressure drag. These pressure losses must be overcome – either by gravity or via a pumping (such as capillary) action of some sort. Previous experimental studies on liquid supply can be broken into two categories – steady state and transient.

Semenic et al. [52] used gravitational pumping (about 1m gravity head) to force water through a porous slug (1cm diamter, 2 cm length) consisting of sintered Cu particles with a set diameter. For the packed spheres, they found that permeability was directly related to particle diameter and measured values following a linear trend of: $K[\mu m^2] = 0.0388\mu m*Diameter - 0.8309um^2$. Their particle size range varied between 58 and 83μm and measured permeability values were between 1.5 μm^2 and 2.4 μm^2. They also found that Blake-Kozeny equation under-predicted permeability by about 50%. Qu and Siu-Ho [63,70] tested an array of 200 μm x 200 μm pin fins with heights of 670 μm sandwiched between two substrates. By pumping water through the pins with Re_{inlet} <1000, they measured the drag force associated with flow past the posts.

Semenic et al. [52] determined the capillary pressure inside micro-porous Cu slugs by applying a negative gravity head. The magnitude of the gravity head was gradually increased until the force of gravity overcame the capillary force and the fluid ran out of the slug. They found that the maximum capillary pressure decreased with particle diameter such that P_c [kPa] = -0.2*$D_{particle}$[μm] + 27.81 for a range of diameters from 57 to 82 μm. For particles of diameter 57 μm, a capillary pressure of ~16kPa was measured. Several other methods exist for maximum capillary pressure determination. Vasiliev et al. [71] and others [72] used a bubble point test in which a saturated wick is held against a pressurized column of air. The pressure of the air is controlled and increased until bubbles are seen on the saturated side of the wick. This point indicates the largest effective pore radius.

Holley and Faghri [17] utilized a transient rate-of-rise measurement to determine the permeability and effective pore radius inside structures constructed for fuel cell and heat pipe applications: carbon paper and sintered Cu spheres, respectively. They utilized two techniques – mass and height tracking. By dipping a dray wick or paper into a pool of liquid and then tracking the fluid front or mass flow into the wick, they could determine the effective capillary pressure and permeability. They assumed that the driving capillary pressure acted against gravity and permeability (momentum was ignored). Here we utilize a very similar fluid front tracking technique to determine the liquid supply capability of our wick structures (described in detail in an upcoming section). Other researchers [25,72,73] have performed similar rate-of-rise tests to determine the liquid supply ability.

Thermal Performance in Porous Media (Related to Heat Pipes)

Many different combinations of experimental parameters exist for heat transfer testing of heat pipe wicks. Typical tests attempt to determine the relationship between input heat flux and

temperature superheat at either low or high heat fluxes. Experiments may be designed to emphasize only a certain region of a heat pipe (i.e. the evaporator or condenser) or may constructed to completely mimic the performance of a fully constructed heat pipe. Here we summarize previous work done in the field of heat transfer testing of heat pipe wicks.

At low heat fluxes, Lips et al. [55,56] studied the meniscus shape inside a machined Cu wick with post dimensions on the order of 400 μm in a near-horizontal orientation. They used confocal microscopy to determine the meniscus shape at very low heat fluxes using FC72 and MeOH as the working fluids. Li et al. [74] tested thin wire mesh structures by feeding with an attached, thicker liquid water supply mesh. Xu and Carey [34] tested a groove wick in a tilted orientation in a well controlled chamber while using a copper slap with cartridge heaters to provide the heat flux. Semenic et al. [52, 65] tested monoporous and biporous sintered wicks in a Cu vacuum chamber with a Cu block integrated with cartridge heaters acting as the heat source. They held the wick in a horizontal orientation and built a liquid feed structure around the wick surface to keep the bulk fluid layer below the wicks surface and prevent pool boiling. Reilly and Catton [75] tested an inorganic aqueous solution (IAS) with a similar wick in a closely related experimental setup. Iverson et al. [76] tested a vertically held wick inside a well controlled chamber and provided an input heat flux using a thin film heater. They attempted to record the fluid mass evaporation rate by measuring the rate of fluid condensation on the chamber walls. Cai and Chen [58] studied a vertically-oriented CNT wick with an attached thin film heater chip. In the vertical wick orientations, the wick is only fed by one side (instead of all sides). The heat conduction along the length of the substrate to the liquid pool is estimated to be almost negligible in both cases.

In our heat transfer experiment, the wick is held in a vertical orientation (to prevent pool boiling) and a thin film heater soldered to the sample backside to provide the input heat flux. The experiments are performed in a well controlled Cu vacuum chamber.

5.2 Liquid Rate of Rise

We utilize a liquid rate-of-rise experiment to determine the capillary liquid supply capability, K/R_{eff}, of thin heat pipe wicks. Filtered DI water or Methanol (MeOH) are used as the working fluid. Although water is one of the best working fluids for heat pipes operating at temperatures 20-150°C [18], wicks with limited surface wettability (such as bare Cu) will not naturally wet with water and require a low surface energy fluid (such as MeOH). The sample is mounted to a z-stage and slowly lowered into a pool of liquid. Once contact is made, a macro-scale meniscus (Fig 5.1) quickly forms. The height of this meniscus is a balance between gravity and the capillary force and can be predicted using Eqn. 5.1 [24]. The maximum height of the macro-scale meniscus for water on our surfaces is measured to be 4mm, agreeing closely with Eqn. 5.1.

$$h_0 = \sqrt{\frac{2\sigma(1-\sin\theta_a)}{\rho g}} \qquad (5.1)$$
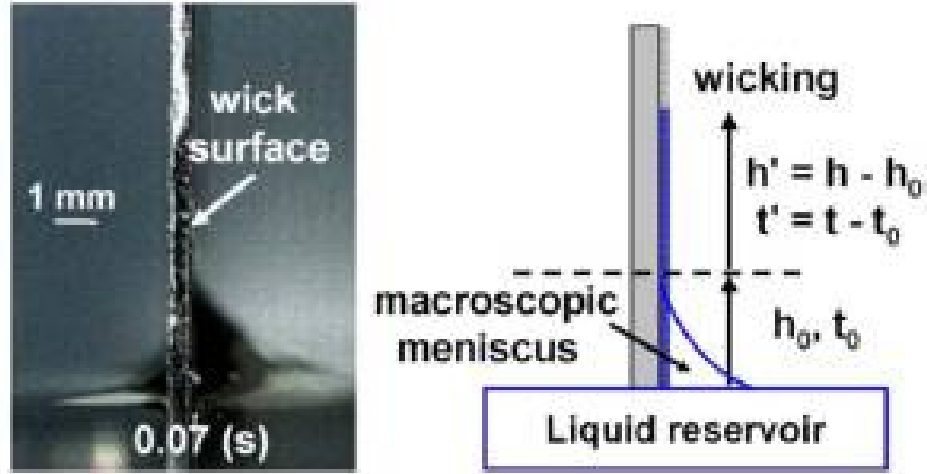
Figure 5.1: Schematic of Liquid Rate-of-Rise Experiment [24].

The fluid will then move vertically through the wick (Fig. 5.2). We track the rising fluid front as a function of time using a high speed camera (Fastcam MC2, Photron) recording at 500 frames per second. For capillary structures with a small pore diameter (< 300 μm), the inertia effect during rising is small and the liquid rise can be described by a balance between capillary, viscous drag, and gravity forces (Eqn. 5.2) [17]:

$$\frac{\sigma_{lv}}{R_{eff}} = \frac{\varepsilon}{K}\mu z \frac{dz}{dt} + \rho g z \qquad (5.2)$$

The actual flow at the micro-scale level will be very complex – especially at the fluid front. The fluid will move in a discontinuous manner in which the fluid front will merge/interact with itself in the horizontal direction before moving further vertically. Eqn. 5.2 is not intended to capture this effect, but rather the average macro-scale behavior of the liquid front.

60
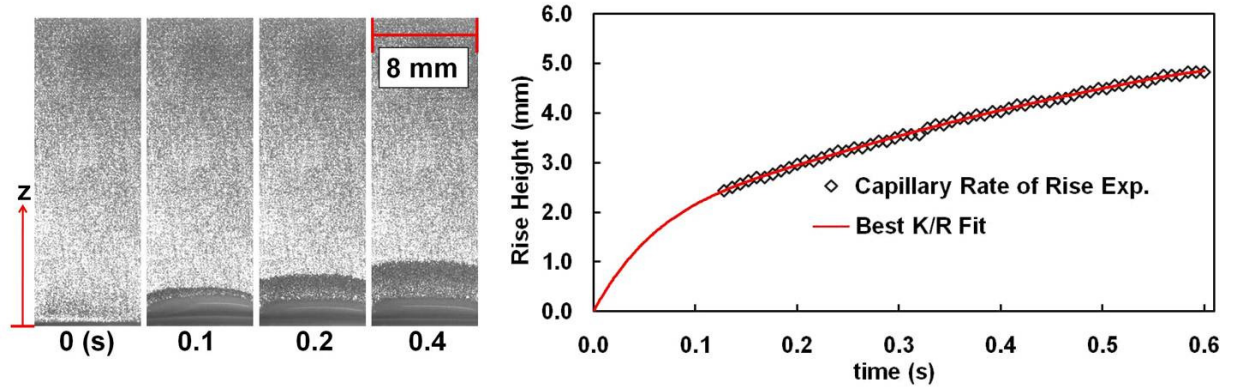
Figure 5.2: Left Side: Fluid front rising up a monolayer of sintered Cu spheres. Right side: Experimental height vs. time and resulting curve fit showing strongest K/R_{eff} fit.

The unknown parameters of Eqn. 5.2 are R_{eff} and K. By combining these terms into the liquid supply coefficient, K/R_{eff}, we arrive at the following equation (Eqn. 5.3):

$$\frac{\varepsilon}{\sigma_{lv}}\mu z \frac{dz}{dt} = \frac{K}{R_{eff}} - K\rho g z \qquad (5.3)$$

The gravity term (last term) of Eqn. 5.3 is much smaller than the K/R_{eff} due to our small experimental fluid heights. The rising height is a strong function of K/R_{eff} and only a weak function of permeability. Even holding K/R_{eff} constant and changing K by 40%, the resulting error is less than 1%. Therefore, only the ratio of K/R_{eff} can be determined and not the individual K or R_{eff} values. Since Eqn. 5.3 is only a weak function of K, we use our permeability modeling efforts (Chapter 2) to predict the appropriate K values.

We track the fluid front using an image processing algorithm in Matlab. After determining the appropriate height vs. time values, we iterate through K/R_{eff} values until finding the best fit. The experimental values can then be compared to the liquid supply modeling results.

61

5.3   Heat Transfer

As shown in the wick schematic below (Fig. 5.3), the sample is held in a vertical orientation during testing to allow the wick to self saturate and prevent pool boiling that otherwise might occur if the sample were held horizontally. The reduction in liquid supply capability due to gravity is determined to be negligible compared to the viscous drag force.

The backside of the wick substrate is Cu (either evaporated Cu on an Si substrate or solid Cu in the case of the sintered spheres) and a thin-film heater chip is soldered using a 100 μm layer of 63/37 tin/lead solder (Melting Point at 185°C, k_{solder} = 50W/mK [77]). The solder thickness is measured using a Dektak profilimeter and found not to vary by more that ±4 μm for all cases. Source and sense wires (32 AWG Cu wires with enamel coating) are then attached to the solder pads. A thin layer of Kapton tape (70 micron) is placed over the serpentine heater to ensure electrical isolation between the heater and the small bare thermocouple bead (0.4mm diameter, 36 AWG, k-type, Omega) placed at the center of the heater area. The thermocouple is held in place using approximately a 2mm diameter drop of Omega-bond 101 (k_{OB101} = 1 W/mK) [78]. The heater chip is then thermally and electrically protected from the saturated ambient environment of the chamber by a 2.5mm layer of high temperature silicone RTV 106 (Momentive). Additional thermocouples (up to 4) of the same size are cemented at various locations along backside of the substrate using OB-101 using the same procedure described above.
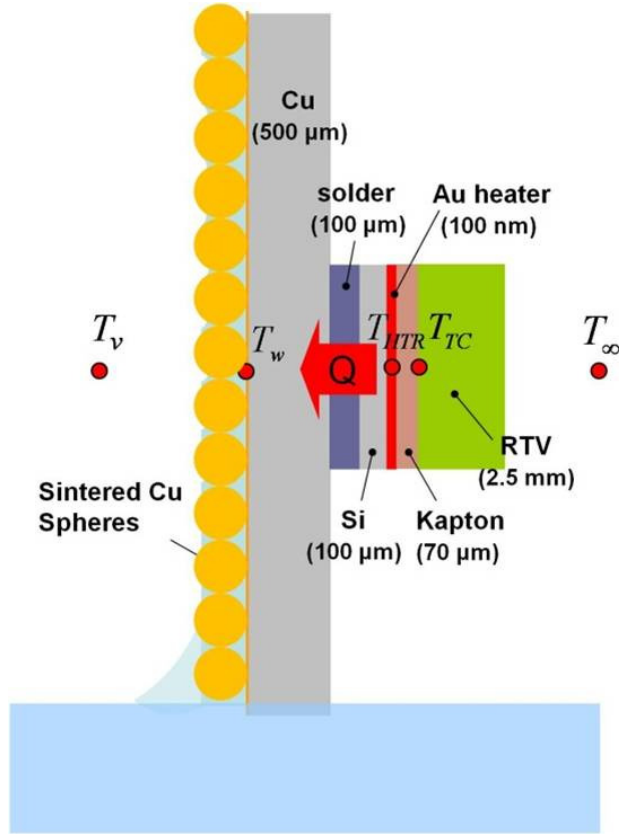
Figure 5.3: Schematic for experimental heat transfer performance test.

The thermal resistance at the solder interface was characterized using a transient hot wire method [62]. Comparing the temporal temperature profile to finite element simulations, a thermal resistance of 5 x 10^{-7} m^2K/W was measured at the solder interface.

Experimental Chamber

The heat transfer experiment occurs in a well-controlled chamber. The ambient temperature, and hence ambient pressure (vapor pressure of the working fluid), inside the chamber are controlled using flowing water through brazed condenser coils on the outside of the chamber. Water flow through the coils is controlled using a thermal bath (Thermoscientific, RTE 7). The chamber walls are comprised of Cu to ensure constant wall temperature.   Water is

used as the working fluid and the chamber is kept at 43°C corresponding to a saturation pressure of ~ 8 kPa [51]. The evaporated fluid condenses on the chamber walls and returns via gravity the liquid pool at the bottom of the chamber (akin to a thermo-siphon). This temperature was chosen because it falls in line with expected operating temperatures for real electronic devices. A ten-thermocouple feed-through system allows for the measurement of temperature at various locations in the chamber vapor space, water, and sample. The thermocouples are initially calibrated against an NIST calibrated Pt thermometer. An Omega pressure gage is also utilized to measure pressure. A LabVIEW program controls the power supply to the heater and records voltage and current, temperature, and pressure. An electrical feed-through allows the supply and measurement of electrical power to the heater chip. An Agilent N5752A high voltage power supply set up in a source-sense mode is used to provide the input power to the heater chip. In addition, a high accuracy-high precision Keithley 2000 multi-meter is also utilized for voltage and current recording.
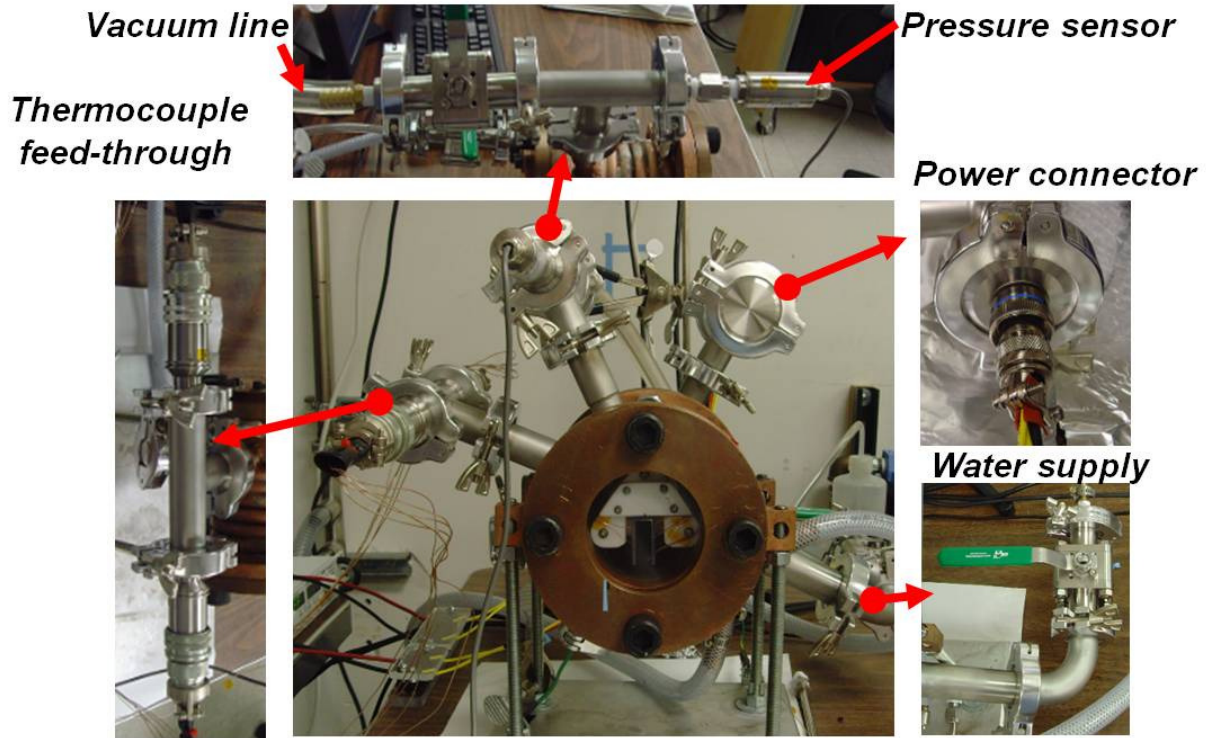
Figure 5.4: Experimental chamber for heat transfer performance test.

Experimental Procedure

After the sample is mounted onto its holder, de-ionized water is pumped into the chamber via mild vacuum pumping. Previously, the water has been degassed by vigorous boiling on a hot plate at 1 atm for four hours. The water is again brought to a rigorous boil four times inside the chamber to ensure degassing. Power is applied to the thin film heater and the sample is allowed to achieve thermal steady state before increasing to the next desired power level. Data is recorded at a frequency of 0.5 Hz and the last 1 minute of steady state data is averaged for analysis.

For an accurate comparison to our heat transfer modeling efforts, thermal spreading between the heater and evaporator surface is accounted for. A numerical model of the substrate and

heater geometry is constructed using the same sample parameters and conditions as used in experimental testing (Fig. 5.5). The Churchill-Chu equation is used to account for natural convection of the water (h_{water}) and saturated vapor (h_∞) on the areas of the substrate in which the wick is not operating. A constant heat transfer coefficient (h_{eff}) is assumed on the wick surface. Values for h_{eff} are iterated until the temperature profile on the heater surface from the simulation matches that of the experiment as measured by a calibrated thermocouple at the same location. The heat transfer coefficient on the surface may be a function of liquid curvature [55] which changes with heat flux, therefore h_{eff} is determined by a linear best fit to between the experimental and predicted heat transfer coefficient values for low heat flux cases. Once the appropriate h_{eff} value is determined, the temperature profile (including T_{wall}) throughout the wick can be determined using our numerical model.
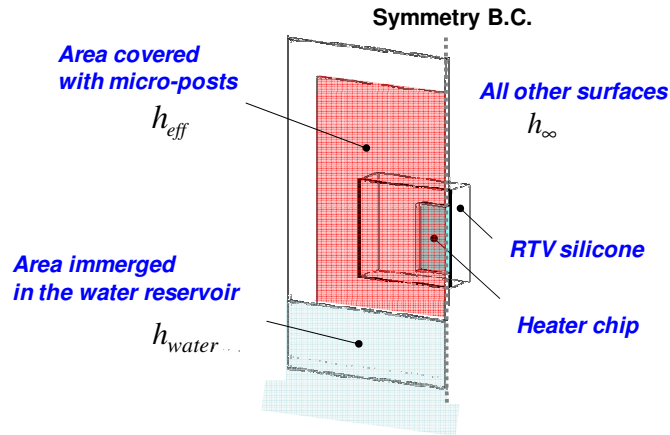
Figure 5.5: Numerical model to account for thermal spreading for accurate characterization of experimental effective heat transfer coefficient.

Assuming the wick is working correctly and has not dried out, our simulations predict that less than 1% of the input heat flux will be lost due to natural convection with the water bath or vapor ambient.

5.4   Summary

Two experiments are used for characterizing the performance of heat pipe wicks and for comparison to our modeling efforts. The first is a rate-of-rise experiment which can be utilized to discern information about the wick's liquid supply capability (directly related to CHF). By tracking the propagation of a fluid front as it rises through an initially dry sample, the permeability and effective pore radius combination can be determined. The second experiment is a heat transfer test which is utilized for determining evaporator performance. The wick is held in a vertical orientation and a soldered thin film heater (5x5 mm^2) acts as a heat source. The chamber itself acts as a condenser and returns the fluid to the liquid supply region of the wick, akin to a thermo-siphon.

CHAPTER 6

Experimental and Modeling Results: Effective Heat Transfer Coefficient

The evaporator is the section of vapor chamber subjected to the highest heat fluxes. The largest opportunity to minimize overall thermal resistance at the chamber level is to optimize the heat transfer in the evaporator region. Heat transfer in this region is dominated by solid and liquid conduction resistance. Previously we presented our modeling efforts to predict the effective heat transfer coefficient on the wick substrate surface – this definition included heat - transfer due through our wick structure, the resulting fluid meniscus, and the liquid-vapor interface. Here we present the results of our modeling and comparison to our experimental data. We analyze three types of structures: a monolayer of sintered Cu spheres, etched high aspect ratio Si structures, and electroplated Cu structures. The Si and Cu structures were designed so as to optimize the wetted perimeter per unit area. Previously we showed good agreement between our modeling and experimental results for hexagonally packed super-hydrophilic Cu posts for a contact angle range of 30-50°. We find that the same contact angle range results in strong agreement to the experimental results. The Cu spheres achieve an effective heat transfer coefficient of ~5.5W/cm^{2}K, the Si structures achieve ~8W/cm^{2}K, and the Cu structures achieve ~12 W/cm^{2}K. The work presented here can be used to minimize the overall thermal resistance in vapor chamber cooling solutions.

6.1   Background

Due to the variety of wick structure and substrate materials and designs, experimental operating conditions, and analysis methods, comparison of different groups' experimental low

heat flux results can be problematic. For example, a sintered Cu wick can be constructed onto a 500 μm or a 2000 μm thick Cu substrate or differently sized heaters can be used. For that reason, we test a variety of samples, attempting as best we can to remove this type of experimental variation so that a fair and accurate comparison can be made between sample types. Nevertheless, presented below is a summary of the experimental findings from previous experiments.

Because of its popularity as a wick material, many researchers have studied the performance of sintered Cu spheres [44, 45, 52, 59, 60, 61, 64, 65, 76, 79, 80]. Weibel et al. [64] experimentally tested phase change heat transfer in sintered Cu particles ranging from 45 – 355 μm in diameter and 600 – 1200 μm thicknesses. They measured an evaporator thermal resistance of ~0.2 K/W between their 1mm thick Cu substrate and reference vapor temperature (measured 1mm from sample surface). Hanlon and Ma [45] determined that thin film evaporation was necessary to achieve the highest evaporation heat transfer coefficients. They studied the effect of wick thickness (1.9mm – 5.7mm) for sintered Cu spheres and achieved heat transfer coefficients of 5000 – 9000 W/m^{2}K. Semenic et al. [52,65] also studied sintered mono-porous and bi-porous spheres and recorded heat transfer coefficients on the order of 9 and 10.5 W/cm^{2}K for mono-porous and biporous wick, respectively. Cai and Chen studied CNT based wicks [58] and claimed heat transfer coefficients as high as 20W/cm^{2}K but didn't mention their calculation method. Different experimental operating conditions and analysis methods makes low heat flux data comparison difficult. For this reason, our work focuses on providing a thorough modeling and experimental based study of the heat transfer physics occurring at low heat fluxes.

6.2   Sample Design Details (Geometries, Dimensions)

Monolayer of Sintered Spheres

A wick comprised of a monolayer of sintered spheres is fabricated on a Cu substrate. The substrate has a thickness of 500 μm and the wick covers an area of 3 x 3 cm. Nominal particle sizes of 29, 59, and 71 um are studied. Properties such as average particle size and distribution, porosity, necking ratio are determined by analysis of SEM images of the wick (Fig. 6.1). Images were analyzed at various locations on the wick sample so that uniformity across the surface could be determined. The results presented in Table 6.1 are averaged across three separately analyzed locations to characterize the properties of the entire surface. Due to manufacturing limitations associated with sieving, the size distribution can be ± 30% of the particle diameter for the small particles. The necking ratio is defined as the length of the neck to length normalized by the average particle diameter.
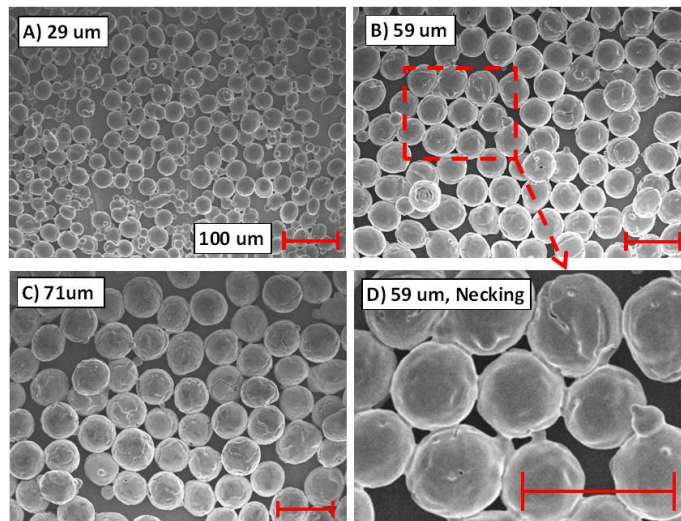
Figure 6.1: SEM images of Monolayer wicks: A) 29 μm, B) 59 μm, C) 71 μm, D) Necking in 59 um sample. Scale bar represents 100 μm for all images.

Porosity is a key characteristic of a wick structure. It describes the percentage of wick volume that is comprised of solid structures. For the monolayer case, porosity was determined using Eqn. 6.1:

$$\epsilon = \left.\sum_b V_{s,i}(D_i)\middle/(Area_b \times \bar{D})\right. \qquad (6.1)$$

where $V_{s,i}(D_i)$ is the spherical volume of particle i based on its measured diameter D, $Area_b$ is the substrate area over which the spheres are measured, and $\bar{D}$ is the average particle diameter in the base area.

Table 6.1: Summary of Monolayer Wick Physical Properties

Diameter	St. Dev.	Porosity	Neck %
29 μm	±8 μm	.35	.43
59	6	.38	.36
71	5	.37	.30

Optimized Etched Si Structures

We derive several alternative geometries for micro-post arrays starting from a uniform hexagonal array of cylindrical posts. Cylindrical posts of a uniform cross section are used as our baseline wick structure because they can be readily micro fabricated using electroplating (e.g. Cu) or deep reactive ion etching (e.g. Si). The primary design approach is to increase the total area of the so-called thin film region per unit evaporator surface area and achieve improved heat transfer coefficients *without* compromising the capillary performance.

The three geometries we examined in detail are shown in Fig. 6.2 and 6.3. In the pie geometry, internal channels (or gaps) are etched into each cylindrical post to increase the thin film region. Other similar variations of the baseline geometry were also investigated, including a gear geometry where each cylinder is replaced with a toothed gear and a sun flower geometry where each cylinder is replaced with a smaller center cylinder surrounded by multiple petal-shaped islands. These geometries showed qualitatively similar results and will not be discussed further. The second design, referred to as the cluster geometry, essentially replaces each "solid" cylinder of the baseline geometry with a sub-array of cylinders of a smaller diameter, D_m.

One unit cell of each wick structure is used to define relevant geometric parameters (Fig. 6.4). For the convenience of comparison and discussion, the diameter of baseline cylindrical posts ($D_p = 55$ μm) and the pitch ($P = 75$ μm) are set to be comparable to those of the uniform micro-post arrays investigated in our previous study (Chapter 2 and 3). The width $2S$ of the internal channels (gaps) of the pie geometry and diameter D_m of sub-array posts in the cluster geometry are set to be approximately 10 μm. The pitch P_m of the intra-cluster posts is 15 μm, resulting in a 5 μm spacing between posts, a typical limit of photolithography for high-aspect ratio structures. A summary of the key geometric parameters is shown in Table 6.2. The solid fraction (SF) of the pie and cluster geometries is 58% and 43% of the baseline case, respectively. The wetted perimeter per unit cell base area (P/UA) of the alternative geometries, in contrast, is approximately 1.8 times larger than the baseline case.
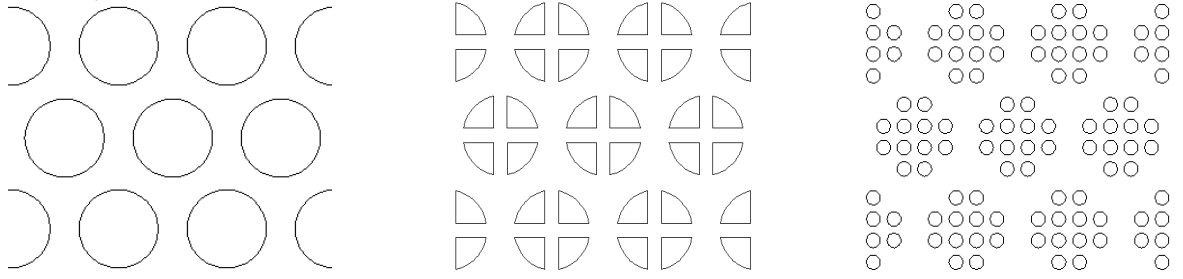
Figure 6.2: Iteration 1: Top views of schematic of hexagonal arrays of the baseline cylinders,

pies, and clusters (from left to right)

(a)   (b)   (c)
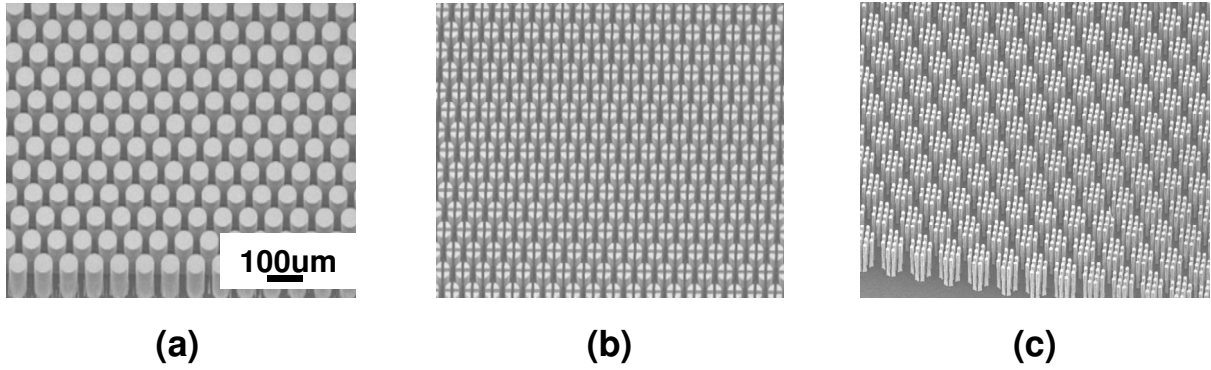
Figure 6.3: Iteration 1: SEM images of the silicon micropost wicks: a) baseline cylindrical

posts, b) pie-cylinders, c) clusters of cylinders.
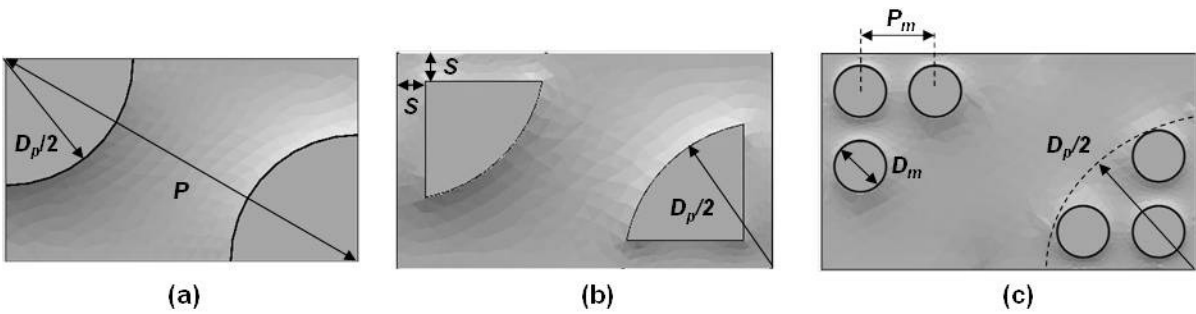
Figure 6.4: Iteration 1: Geometric parameters for the wick structures. (a) baseline cylindrical

posts (b) pie (c) cluster.

Table 6.2: Geometric Parameters for the Iteration 1 Wick Structures

	Solid Fraction	Perimeter per unit cell base area (μm^{-1})	D_p (μm)	P (μm)	Height (μm)
Cylinder	0.488	0.035			
Pie	0.283	0.064	55	75	140
Cluster	0.211	0.064			

Optimized Electroplated Cu Structures

We model and experimentally test four different structures: two cylindrical post geometries and two advanced "pie" structures similar to those presented in the previous Si structure section. The "pie" structures were chosen because of their high perimeter/unit area compared with the baseline cylindrical post case. A summary of the properties of the tested geometries is presented in Table 6.3. Fig. 6.5A-C presents SEM images of the fabricated structures.

Table 6.3: Geometric Parameters for the Iteration 2 Wick Structures

	Geometry	Nominal Diameter D_p	Nominal Spacing D_{cc}	Intra Spacing 2S	Height	Solid Fraction	Perim./ Unit Base Area
Iter. 2	Circular Post	75 μm	30 μm		100 μm	0.463	0.025 μm^{-1}
			50			0.326	0.017
	"Pie"		30	15 μm		0.388	0.043
			50			0.274	0.029

(a)   (b)   (c)
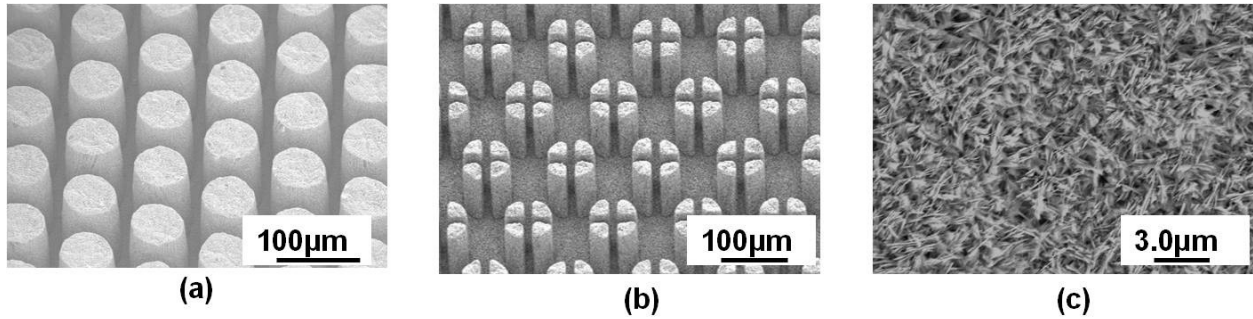
Figure 6.5: Iteration 2 Samples: A) SEM image of 75/30 post structure, B) SEM of 75/50 "pie" structure, C) SEM of super-hydrophilic CuO oxide structure

6.3   Effective Heat Transfer Coefficient – Results and Discussion

Modeling – Effective Heat Transfer Coefficient

Assuming that the majority of heat transfer occurs across the thin-film regions with small liquid conduction resistance, one may use a normalized thin-film area α, defined as (meniscus area within the thin-film region) / wick unit base area, to help compare the thermal performance of different wick structures. For example, in Chapter 3 it was shown that for a copper baseline cylindrical micropost wick, over 50% of total heat transfer is estimated to occur over the thin-

film regions when the appraent contact angle is small. For a variety of different post spacings, diameters, and contact angles, it was shown that due to the high percentage of heat transfer through the thin film region, the normalized thin film area was a strong predictor of heat transfer performance. However, more in-depth modeling analysis, presented in this chapter, reveals that at low solid fractions and moderate thermal conductivities, solid thermal resistance can be the dominant resistance term.

In the following discussion, water is chosen as the working liquid due to its favorable heat transfer properties at typical operating temperatures of heat pipes and vapor chambers for electronics cooling applications. The physical properties of water are obtained at the nominal condition used in our experimental study (saturated water at 45 ºC).

Mesh Analysis

Two meshes were analyzed: a surface mesh and a volumetric mesh. The surface mesh describes the liquid surface shape under the influence of surface tension. Over 6000 surface mesh elements were used to model the thin film region. Increasing the number of mesh elements in the region by 33% (to 8000 elements) resulted in < 1% change in h_{eff}, thus convergence was assumed. Doubling the number of volume mesh elements in the thin film region also resulted in less than < 1% change in h_{eff}.

Modeling and Experimental Results for Sintered Cu Spheres – Discussion

The meniscus shape between closely packed spheres can be quite complicated. Due to the small effective pore size when the spheres are touching (Fig. 6.6), the normalized thin film area can be quite large. Of course the thin film area is also a function of other parameters such

76

as the filling ratio (Initial Flat Fill Height/Pore Height, Fig 6.6C) and contact angle. Calculated

h_{eff} values are presented in Fig. 6.7. At low contact angles, the normalized thin film area is large;

hence very large heat transfer coefficients are realized. Very low contact angles produce a very

wettable surface, and at moderate fill ratios the effect of the extended meniscus can be large as

indicated by the exceptionally large h_{eff} values for a contact angle of 20°.
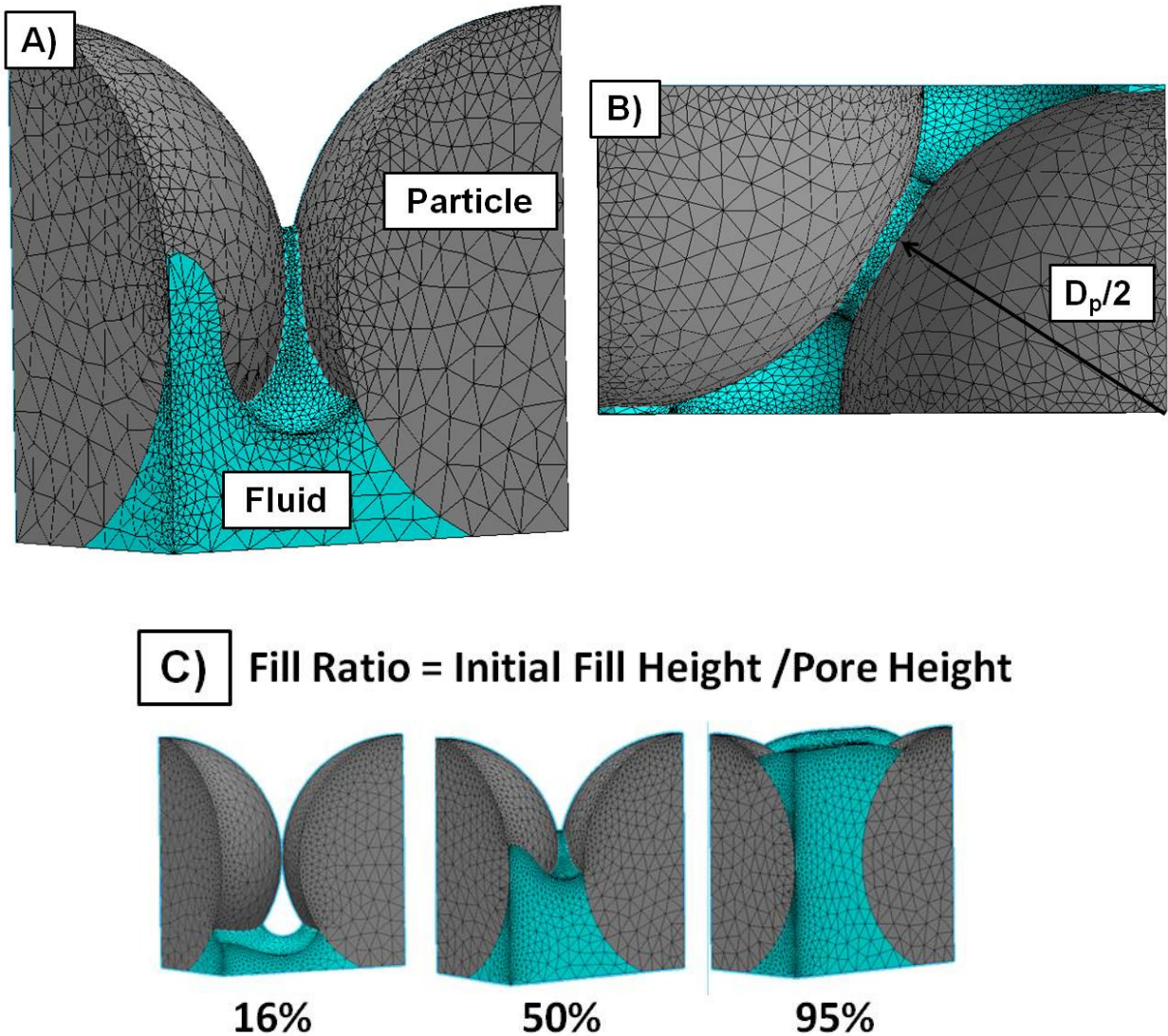
Figure 6.6: 3D meniscus shape between closely packed spheres. A: side view, B: top view. C:

Definition of Liquid Fill Ratio.
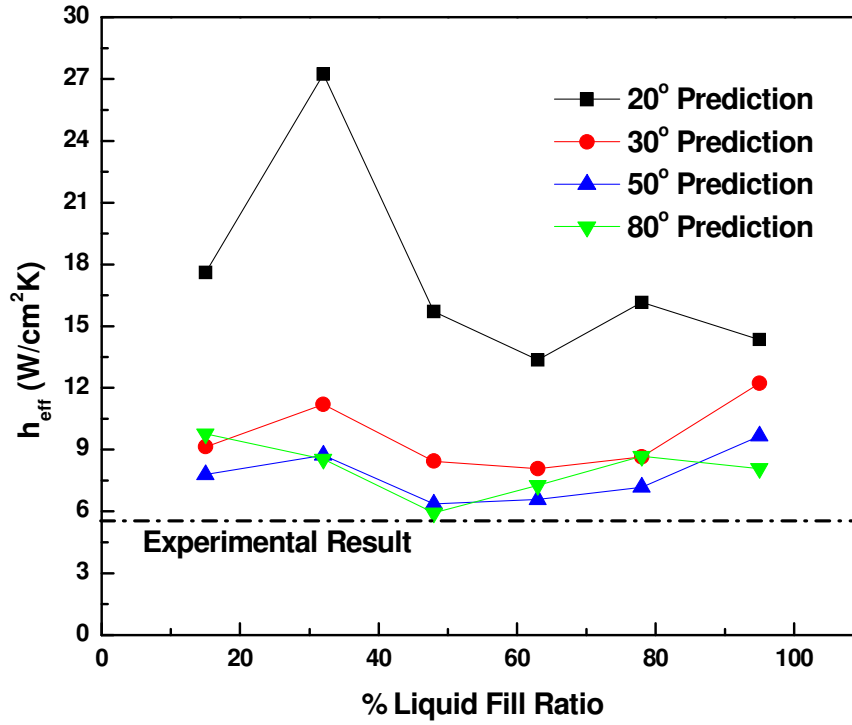
Figure 6.7: Comparison between modeling and experimental results for $D_{particle} = 59$ μm.

Comparison between the modeled and experimental results at low heat fluxes reveals strong agreement to the contact angle range of 55-80° at fill ratios of ~50%. At a fill ratio of 50%, in which the fluid height of a 90° contact angle would be $D_p/2$, the capillary pressure is typically highest because that is where the effective pore size is smallest (Fig. 7.2). The contact angle of water on flat, bare Cu is typically measured to be 80° [67]. While the static contact angle value does not include the effects interline region heat transfer, it does give a good predictor of what the meniscus shape may look like, especially at high heat fluxes when the wettability of the surface is somewhat limited compared to a more hydrophilic surface. Experimentally, effective heat transfer coefficients of 5.2 and 3.5 W/cm²K were achieved for the

78

59 and 71 μm particle diameters, respectively. In both cases, this agrees most closely with the moderate fill ratio, high contact angle predictions.

Modeling Results for Thin Film Optimized Structures - Discussion

Silicon and copper are chosen as wick materials for discussion because of their moderate to high thermal conductivities and use in our experimental testing. Diamond is also studied because its extremeley high thermal conductivity (~2000 W/mK) can be used as a refernce case where the effect of solid conduction resistance is negligible.

As mentioned previouly, although the majority of heat transfer will occur through the thin film region, in some cases, the effect of solid conduction resistance must be considered for an accurate h_{eff} prediction. For our first design iteration, Figure 6.8 shows the predicted effective heat transfer coefficient of the different Cu wicks as a function of the apparent contact angle for the case of the 55/20 nominal post geometry of our 1st iteration . The increase in heat transfer coefficient with decreasing apparent contact angle is due in part to increase in the areas of the thin-film regions and in part to increase in the overall meniscus area. The cluster and pie geometries exhibit higher thermal performance but only at contact angles > 20°. At smaller apparent contact angles, the baseline cylindrical post performs as well as or better than the two alternative geometries. As the apparent contact angle is reduced, the conduction resistance associated with the solid posts becomes more important. Due to their lower solid fractions, the cluster and pie geometries have larger solid conduction thermal resistances, which offset the benefit of the larger normalized thin-film areas. Therefore, we proceed with a second, higher solid fraction design iteration as shown in Table 6.3 and Figure 6.9.
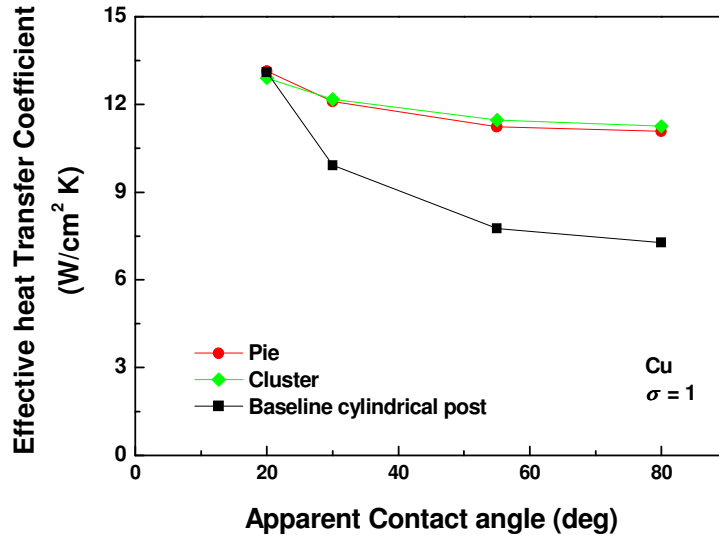
Figure 6.8: Predicted effective heat transfer coefficient Cu micro-post wicks with different geometries (Iteration 1 in Table 6.3). The accommodation coefficient $\hat{\sigma}$ is assumed to be 1.

The predicted h_{eff} values calculated using the static meniscus model are shown in Fig. 6.9. At high contact angles, liquid resistance is high and the benefit from the increased interline region is largest. Therefore, at high contact angles, the pie structures achieve the highest h_{eff} values despite the increased solid conduction resistance. As the contact angle decreases, liquid conduction resistance decreases, and the effect of solid conduction resistance increases. Hence, at low contact angles the lowest solid fraction wick (75/50 pie) is predicted to perform the worst despite the increased interline region. The 75/30 pie structure, however, has a large solid fraction so that even at low fluid conduction resistance, it still takes advantage of its high interline region.
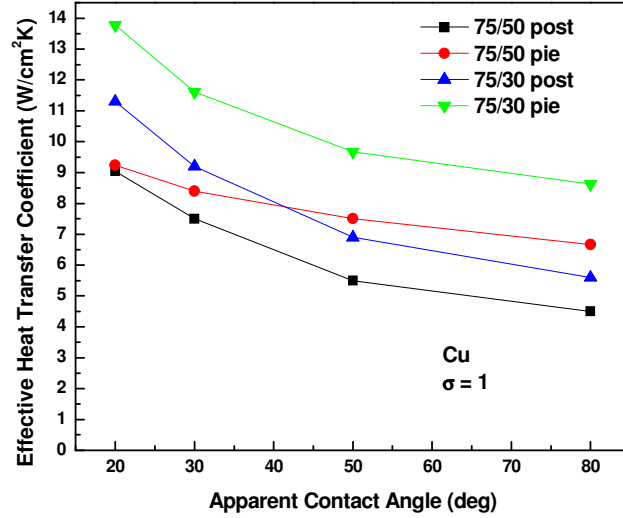
Figure 6.9: h_{eff} predicted by the static meniscus model (Iteration 2 in Table 6.3). The accommodation coefficient $\hat{\sigma}$ is assumed to be 1.

The effect of the interplay between solid and liquid conduction resistances can be further seen in Fig. 6.10 and 6.11 where we show the predicted effective heat transfer coefficient of the three wicks made of silicon and diamond (Iteration 1), respectively. Due to the moderate thermal conductivity of Si, the threshold apparent contact angle below which the baseline cylindrical geometry provides higher values of h_{eff} is larger for silicon. The pie geometry also exhibits better performance than the cluster geometry since the former has a higher solid fraction and the determinental effects of the lower thermal conductivity are smaller. For diamond, which as almost five times higher thermal conductivity than copper, the effect of solid conduction resistance is smaller and the cluster geometry exhibits the best performance even at an apparent contact angle around 20 °.
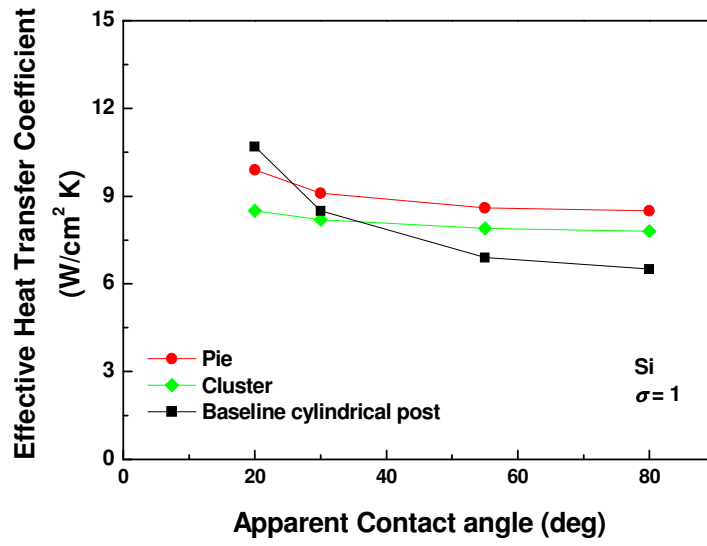
Figure 6.10: Predicted effective heat transfer coefficient Si micro-post wicks with different geometries. The accommodation coefficient $\hat{\sigma}$ is assumed to be 1.
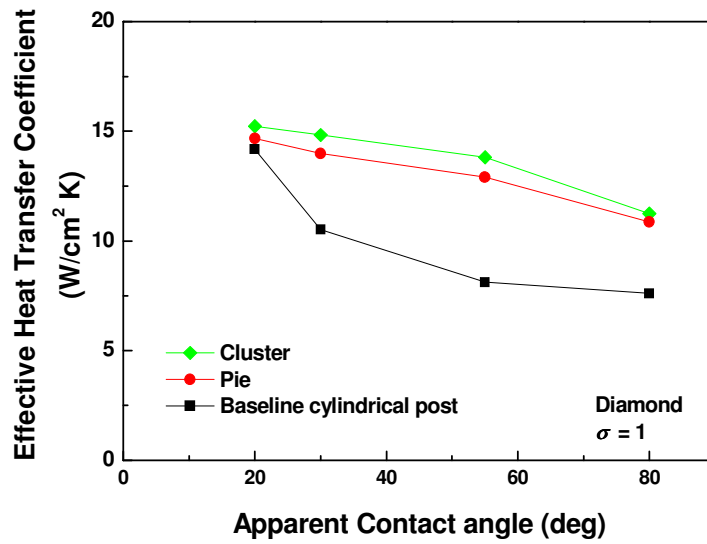
Figure 6.11: Predicted effective heat transfer coefficient diamond micro-post wicks with different geometries. The accommodation coefficient $\hat{\sigma}$ is assumed to be 1.

Figure 6.12 shows the predicted h_{eff} for Si micro-post (iteration 1) wicks for $\hat{\sigma} = 0.5$. The increased evaporation resistance results in smaller values of h_{eff} and reduced impact of the solid conduction resistance. The trend between geometries, however, remains roughly the same even when $\hat{\sigma}$ is as low as 0.25.
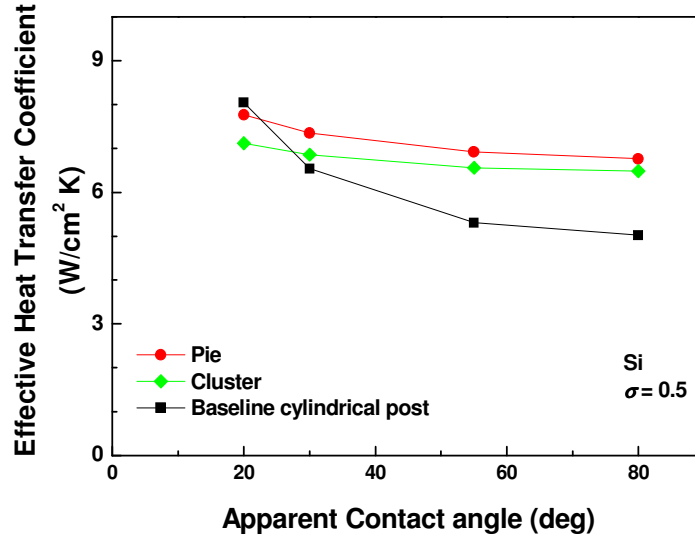
Figure 6.12: Predicted effective heat transfer coefficient Si micro-post wicks with different geometries. The accommodation coefficient $\hat{\sigma}$ is assumed to be 0.5.

Experimental Results for Thin Film Optimized Structures - Discussion

Figure 6.13 shows the experimentally measured heat transfer performance of the three wick samples. At nominal heat fluxes below ~ 20 W/cm^2 K, the superheat increases approximately linearly with heat flux. As local dryout occurs, the superheat increases more rapidly with heat flux, similar to the trend observed in our earlier work on wick samples containing uniform arrays of electroplated copper micro-posts.
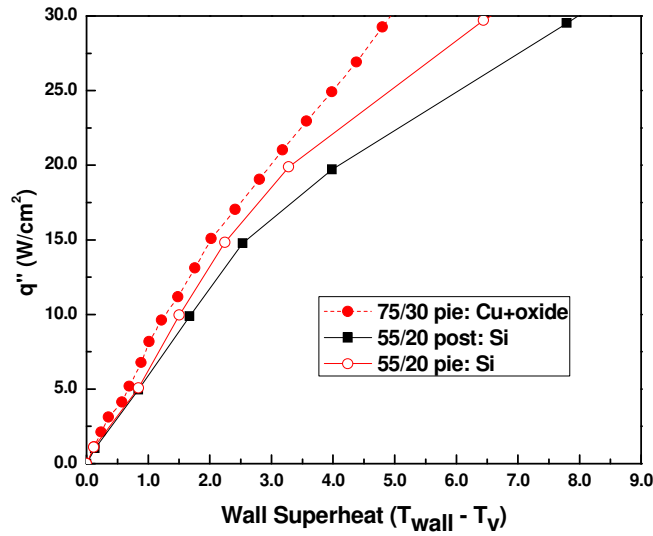
Figure 6.13: Experimentally measured low flux heat transfer performance of the coated and bare Cu wick structurs (iteration 2).

Following the procedure outlined in Chapter 5, we performed 3D numerical simulations to determine the average effective heat transfer coefficient of each wick by matching the predicted temperature rise in the thin film heater with the measured experimental value.

Figure 6.14 shows the effective heat transfer coefficients we determined from the experimental data in the low heat flux regions (< 15 W/cm^2 K) for the Si geometries (Iteration 1). The pie geometry shows the best performance in terms of h_{eff}. The model predictions with an apparent contact angles of $20 \sim 30º$ and $\hat{\sigma} = 0.5 \sim 1$ are generally consistent with the data. The performance of the baseline post geometry suffers from its low normalized thin-film area whereas the cluster geometry suffers from high solid conduction resistance resulting from its low solid fraction and the moderate thermal conductivity of silicon.
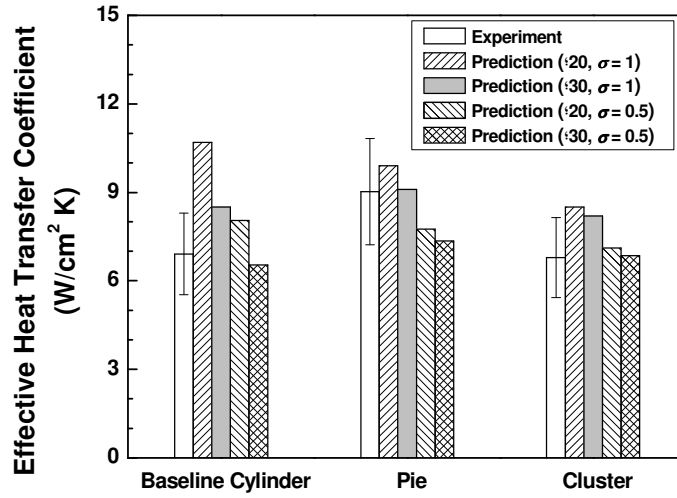
Figure 6.14: The experimentally determined and predicted effective heat transfer coefficients of

the three Si micro-post wicks (iteration 1).

For our Cu geometries, at low heat fluxes (< 20 W/cm^2), we compare the results of our static meniscus modeling to the experimental results (Fig. 6.15). Effective heat transfer coefficients as high as 12 W/cm^{2}K are achieved for the super-hydrophilic oxide coated 75/30 pie geometry. The best agreement for the super-hydrophilic geometries is found when an intrinsic contact angle of 20-40° is utilized in the static meniscus model. For the bare Cu samples, where small contact angles are expected not to occur, the agreeing contact angle range is around 80-90° for the 75/50 pie case, close to the contact angle of water on bare Cu [67]. This is also consisted with our bare Cu sintered sphere results. In the case of the bare Cu 75/30 post, the experimental results are lower than the predicted results. We hypothesize that this is due to the local wick dryout which may occur at even low heat fluxes due to poor liquid supply associated with the high solid fraction and low permeability and capillary pressure.
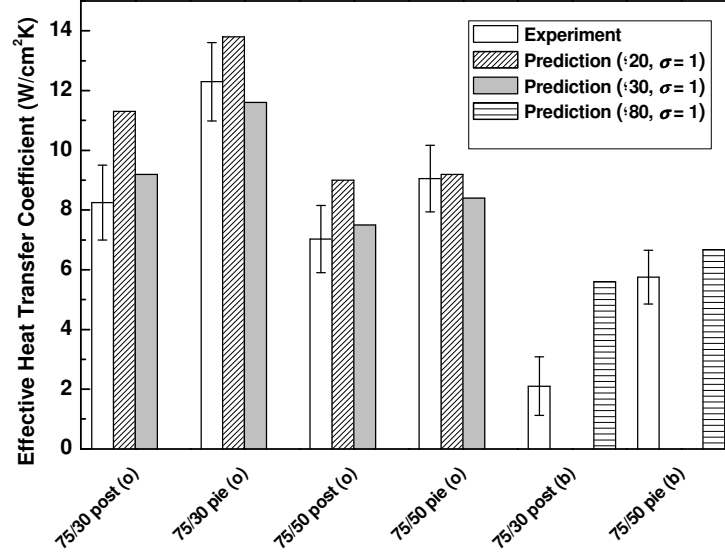
Figure 6.15: Comparison of static meniscus prediction to experimental h_{eff}.

6.4   Summary

The work presented in this chapter can be used to help design low thermal resistance

evaporators. Our modeling and wick design accounts for the effect of solid and liquid

conduction resistances. The geometries and structures studied include a monolayer of sintered

Cu spheres and optimized Cu and Si post-based geometries. The moderate thermal conductivity

of Si limited the effect of the thin-film optimization, but Cu geometries showed large decreases

in thermal resistance as a result of its high conductivity and thin-film area. Effective heat

transfer coefficients higher than 12 W/cm^{2}K were achieved for our optimized super-hydrophilic

Cu structures.

86

CHAPTER 7

Experimental and Modeling Results: Liquid Supply and Mid to High Heat Flux Regimes

Phase change heat spreaders offer a lightweight, and low profile thermal solution for dissipating large heat fluxes from electronic components. In capillary pumped devices, the evaporator region, which sees the largest fluxes, consists of micro structures which can have a large impact on the maximum allowed heat flux (CHF).

We use our liquid supply computational models (Chapter 2) to predict and optimize the post structure and geometry to increase CHF by increasing the capillary liquid supply while at the same time increase the interline region available for evaporation. Micro-fabrication techniques (Chapter 4) are used to construct these novel Cu and Si wick structures with aspect ratios as high as 5 and 10, respectively. In addition, a monolayer of sintered Cu spheres is studied as well. Heat transfer experiments are performed using a 5x5mm^2 thin film heater inside a controlled vacuum chamber.

We present the results of our advanced-geometry heat pipe wick investigation. This chapter focuses on moderate and high heat flux regimes. The effect of surface wettability and post height are all studied using both modeling and experimental analysis.

The results of this work can be used to aid in the design of thin and light-weight phase change thermal solutions by increasing the maximum CHF sustained by a thin heat pipe wick while at the same time minimizing thermal resistance.

7.1   Background

Previous heat pipe models have typically focused on one of two aspects: the overall heat pipe performance with the goal of determining critical heat flux (CHF) or a very detailed model

of the thin liquid meniscus interline region. CHF predictions allow for an estimated maximum heat flux capability – above which heat pipe will fail to operate as designed and device catastrophe may occur. CHF Modeling may include parameters such as liquid pressure drop, vapor pressure drop, capillary pumping, and other complexities such as boiling inception. These methods can then be applied to a variety of simple or complex wick structures [18,79].

We make use of our 3D meniscus modeling scheme which predicts both the capillary liquid supply capability (important for CHF) and the evaporator wick thermal resistance of advanced 3D geometries. By computing the 3D liquid meniscus shape, the driving capillary pressure can be determined. Liquid permeability can also be determined. In Chapter 6, we describe one facet of our wick design methodology: decreasing the thermal resistance by increasing the interline region available for evaporation. These optimized structures, with high liquid supply capability and low thermal resistances, are predicted to be superior to similar baseline cylindrical post geometries.

Traditionally, heat pipe wicks have been fabricated with sintered spheres, wire mesh, or uni-axial grooves [34, 45, 74]. CHF results have been shown to be a strong function of wick structure [65] and thickness [45, 65, 74]. Semenic et al. [65] measured CHF values of ~300 W/cm^2 using monoporous sintered Cu spheres with a thickness of 0.58 mm. Weibel at al [64] used a thicker monoporous wick (0.6 – 1.2mm) to reach CHF values between 500-600W/cm^2. Li et al. [74] used thin wire mesh layers + a liquid feeding wire mesh layer to achieve CHFs between 150 – 375 W/cm2 for wick thicknesses between 0.21 – 0.82 mm. More recently, researchers have begun fabricating wicks using etched silicon or titanium [59,81], carbon nano-tubes [58], or copper posts [62]. Cai and Chen [58] claimed their 250 μm thick CNT based wick could achieve a CHF of more than 600W/cm^2 with a heater size of 2x2mm^2 before device failure.

Nam [62] used hexagonal arrays of super-hydrophilic Cu posts (100 μm thick) and achieved

CHF values of ~170 W/cm^2 and ~950 W/cm^2 using 5x5mm^2 and 2x2mm^2 heaters. Advanced

wicks structures utilizing multiple length scales for optimized liquid supply have also been

studied by other researchers [40,54,58]. Semenic et al. [52] used biporous evaporators with a

thickness of 2.6mm to achieve a CHF of 1340 W/cm^2 with a heater radius of 3.2mm.

Our aforementioned optimized structures achieve increased CHF values over our baseline

cylindrical post structures due to increased liquid supply capability as well as large increases (20-

30%) in the effective heat transfer coefficient on the wicks surface. The work we present here

can be used for extremely thin evaporator wicks (<200 μm thickness) or for a thin evaporation

layer in multi-structure type devices.

7.2 Sample Design Details

We utilize the same sintered Cu spheres structure presented in Chapter 6. For our

optimized post-based geometries, we utilize the geometries from our "Iteration 2" group using

both Si and Cu.

Table 7.1: Summary of Si and Cu Geometries.

	Geometry	Nominal Diameter D_p	Nominal Spacing D_{cc}	Intra Spacing W	Height	Solid Fraction	Perim./ Base Area
Iteration 2	**Circular Post**	75 μm	30 μm		Cu: 100 μm Si: 100 & 200 μm	0.463	0.025 μm^{-1}
			50			0.326	0.017
	"Pie"		30	15 μm		0.388	0.043
			50			0.274	0.029

7.3　　Liquid Supply Results and Discussion

Monolayer of Sintered Spheres

Capillary pressure and permeability are modeled for the 59 um particle diameter. Although real monolayer structures feature particle-to-particle necking and intra sample variation, modeling all such possibilities is impossible. The particle-substrate interaction is important for both heat transfer (point contact of a sphere to a plane can be source of high thermal contact resistance) and capillary pressure. The substrate to sphere interaction is modeled such that the particle is "necked" to the sphere with a neck radius to particle radius ratio of 0.33. In addition, particle-to-particle interaction is considered by forcing the spheres to have a very small spacing – 0.2 μm at their closest points. This allows accurate and relevant computation of the liquid meniscus without the complexities associated with intersecting geometries. As can be seen in Fig. 7.2, the resulting meniscus shape near the thinnest part of the sphere separation can be quite complex.

Permeability is modeled using the methodology presented in Chapter 2. Both filling ratio (initial fluid height / particle diameter) and contact angle are varied to account for a number of possible flow conditions. Contact angle is shown to have minimal impact on permeability (Fig. 7.1). This is to be expected as the filling ratio is thought to be more closely related to the effect of the no-slip wall condition. As the filling ratio decreases, the permeability drops as well. At moderate fill ratios (50-80%), the permeability remains roughly constant. Within this range, the increase "flow area" is minimal because the necking region is relatively small.

The Carman-Kozeny relation [22] shown in Eqn. 7.1 is a semi-heuristic model that predicts permeability for a uniform slug of packed spheres with diameter D and porosity ϵ.

Using the values for particle diameter and porosity in Table 6.1, the Carman-Kozeny relationship over predicts the permeability by a factor of ~2 compared to the modeling prediction at the largest fill ratios. Semenic performed and experimental study for sintered Cu spheres as a function of particle diameter. Using Semenic's correlation for permeability, good agreement is found between his experimental results (1.5 μm^2) and the predicted computational method used here at high fill ratios [65]. Although the flow conditions through a monolayer can be different than flow through a bulk slug, at high fill ratios the entire pore is available for liquid flow, similar to the flow conditions used by Semenic. When the fill ratio is low, the effect of the substrate wall can be quite large and the flow conditions deviate from a bulk sample in which the entire pore is typically available for flow through.

$$K = \frac{D^2 \varepsilon^3}{150(1-\varepsilon^2)} \qquad (7.1)$$
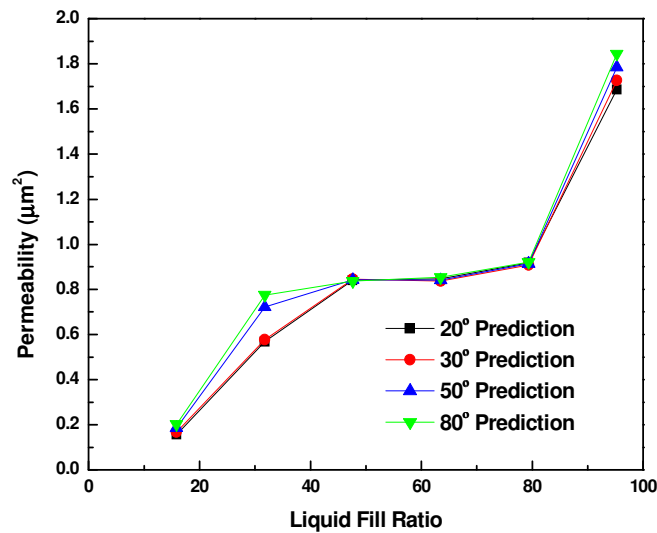
Figure 7.1: Predicted permeability water flow through monolayer of closely packed Cu sphere monolayer, $D_{avg} = 59$ μm.

The capillary pressure is computed following the methodology presented in Chapter 2. Figure 7.2 below is calculated for water using a surface tension of 72 mN/m. At large filling ratios, the surface tension interaction with the curved sphere surface results in a negative capillary pressure. At moderate filling ratios, the very small spacing between spheres results in very high capillary pressures – approaching 25 kPa for low contact angles. For a packed bed of spheres, Semenic [65] experimentally demonstrated that the maximum capillary pressure of water inside a slug of packed sintered spheres could be described as a function of particle diameter. The best agreement between the static meniscus capillary pressure and that measured by Semenic (16 kPa) is for moderate fill ratio (50%) and contact angle of ~55°. Semenic used a falling meniscus method which likely measured the capillary pressure occurring due to a receding meniscus within the smallest portion of the pore (Fig. 6.6). Although the contact angle of water on bare Cu is ~ 80° [67], the receding contact angle of water has been measured to be close ~50° on a slightly tilted plate [91].

We experimentally measure the liquid supply performance of each monolayer sample described in Table 6.1. We compare the effect of average particle diameter on liquid supply performance in Fig. 7.3. In addition, the experimental results are compared to our predicted results. Because our experiment used Methanol as the working fluid, a correlation relating the effective pore radii between Methanol and water is used ($R_{eff} = R_p\cos\theta$). The complexities associated with dynamic flow though a complex medium such as a monolayer of sintered spheres make exact knowledge of the flow characteristics difficult. Our static meniscus results are presented for capillary pressure associated with a 50% fill ratio and a contact angle of 55°and permeabilities of fill ratios of 55% and 100%. The first combination was chosen as a lower limit and describes the case in which the cross sectional flow area in the majority of the wick is

92

constrained due to the fluid only filling up to the point of maximum capillary pressure. The

second combination describes the case in which the cross sectional flow area is the entire height

of the particle diameter, implying that the majority of the wick sees a completely saturated wick.

The experimentally measured rate-of-rise experiment show that the liquid supply increases with

particle diameter (Fig. 7.3). The performance peaks around 59 μm and then begins to decrease.

The experimental results fall between the upper and lower predictions, showing the validity of

the prediction method.
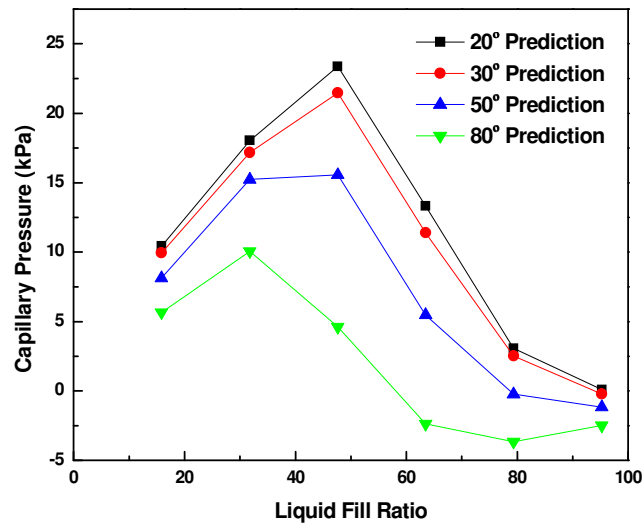
Figure 7.2: Predicted capillary pressure water in monolayer of closely packed Cu sphere

geometry, $D_{avg} = 59$ μm.
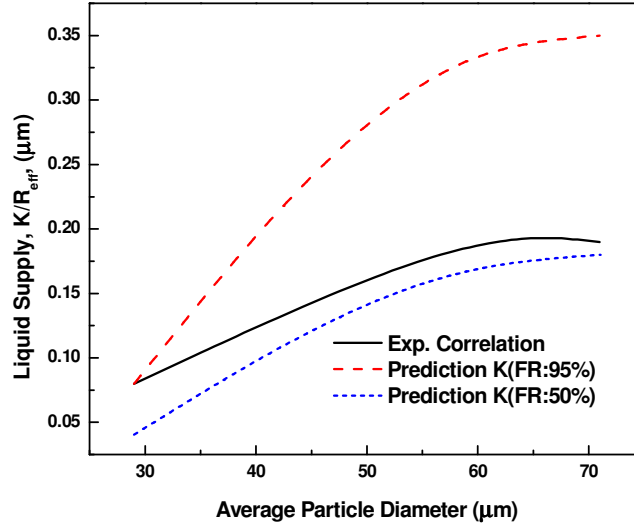
Figure 7.3: Experimentally determined liquid supply coefficient for monolayer of sintered Cu spheres.

Advanced Si and Cu Geometries

The liquid supply of the post and pie structures (Iteration 2) is presented in Fig. 7.4. In the post structure, the fluid volume is chosen so that the fluid meniscus reaches to top of the post (100μm) without the meniscus shape and curvature being affected by the geometry requirements. In the pie geometry, meniscus shape is shown to be a very strong function of fluid volume: the small pore sizes associated with the intra-spacing between individual posts can result in complicated and non-relevant meniscus shapes. For this reason, the fluid level is iterated until the capillary pressure for a given contact angle agrees with the corresponding baseline post case. Following our previous work, we expect that the structures with the CuO nanostructure and SiO_2 coating will achieve K/R values corresponding to contact angles of approximately 7° [24] and 10°. At low contact angles, the advanced structures are shown to increase the liquid supply capability by approximately 20% for the low solid fraction (75/50 case) and by ~40% for the

94

higher solid fraction case (75/30). This increase in K/R decreases only slightly as the contact

angles increases.
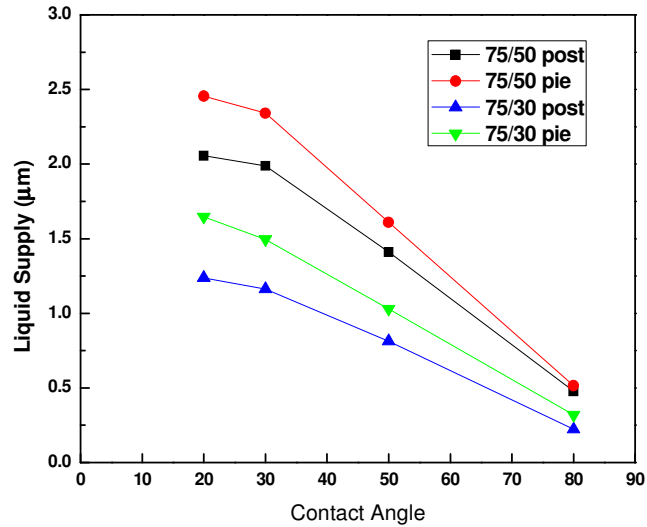
Figure 7.4: Modeled Liquid Supply of Post and Pie Structures

7.4   Moderate and Critical Heat Flux Results and Discussion

Monolayer of Sintered Spheres

In the mid-range heat flux region (13 W/cm^2 < q" < 60 W/cm^2), the 59 um sample

demonstrates higher performance at a given superheat than does the 71 μm sample. In this

region, the effective monolayer thickness can affect the relative performance for different

particle sizes. Hwang [79] claimed that effective thermal conductivity of a Cu monolayer with

spheres of ~ 60 μm and porosity of 0.4 was between 4.6 – 10 W/mK and used 6 W/mK with

good agreement to experimental results. 1-D modeling produces a ~1K difference in superheat

for a 15 μm change in wick thickness at 60 W/cm^2. Additional deviation in wick superheat

between the 71 μm and 59 μm sample may be due to complex phenomena such as local dryout.

95

The low heat transfer coefficient of 29 μm sample suggests that local wick dryout has already crippled performance.

As heat flux increases past 60W/cm^2, the higher liquid supply performance of the larger diameter samples acts to delay the initiation of wick dry out, as seen in Fig. 7.5. The 59 μm and 71 μm samples show similar effective heat transfer coefficients in this regime. As the heat flux increases past 80 W/cm^2, the slopes of the two samples decrease at an accelerated rate, suggesting that dryout has occurred. Both the 59 μm and 71 μm samples reach CHF at approximately the same heat flux, in agreement with our liquid rate of rise results.
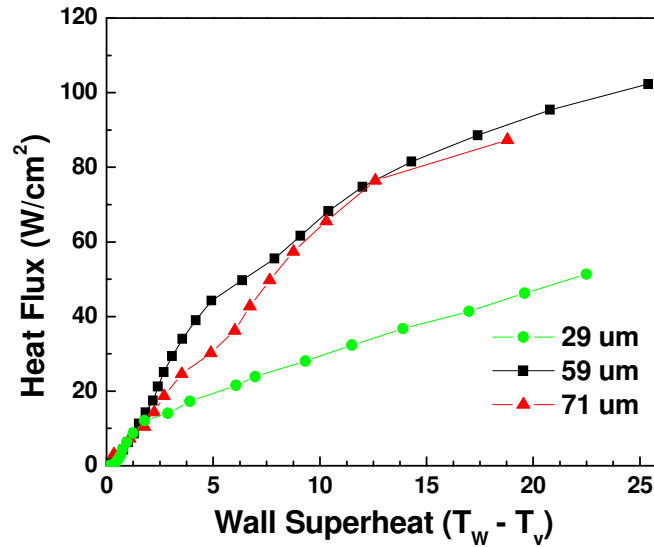
Figure 7.5: Heat flux vs. wall superheat for sintered Cu monolayer particles.

Advanced Cu and Si Geometries

To predict the capillary limited heat fluxes, we construct a 3D numerical model (Fig. 7.6) which mimics the conditions of our heat transfer performance experiment and sample. This

model considers the previously calculated permeability, evaporation on the wick surface, heat spreading through the Si substrate, temperature variation on fluid properties, and maximum capillary pressure (Fig. 7.6). A constant flow area corresponding to the post height (100 μm) is assumed. A constant pressure boundary condition is applied as the fluid inlet condition and symmetry imposed on the sides of the wick surface. The input heat flux is applied over a 5x5mm^2 area. The capillary pressure required to pump the fluid is computed as the liquid pressure gradient. When the maximum capillary pressure required for fluid pumping exceeds the maximum capillary pressure predicted by our static meniscus model, the capillary limit is assumed to be reached.

The results of this 3D numerical model area are compared to the 1D capillary heat flux limit (Eqn. 2.2) for a variety of different fluid temperature considerations with good agreement. Predicted capillary limited heat fluxes are between 200W/cm^2 for the 75/30 post structure and 400 W/cm^2 for the 75/50 pie structure (Fig. 7.7). As will be shown, the capillary limit is just one of the possible heat flux limitations. It will be shown that at heat fluxes at approximately 100 W/cm^2 result in boiling and partial wick dry-out.
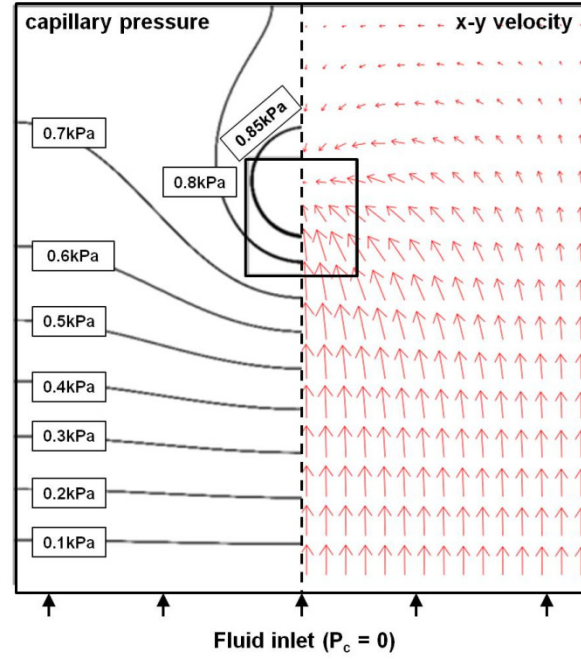
Figure 7.6: Predicted flow characteristics (capillary pressure and velocity field) of experimental

flow conditions calculated using predicted permeability for 75/50 pie geometry. Heat flux from

$5x5$ mm^2 heater = 100 W/cm^2.
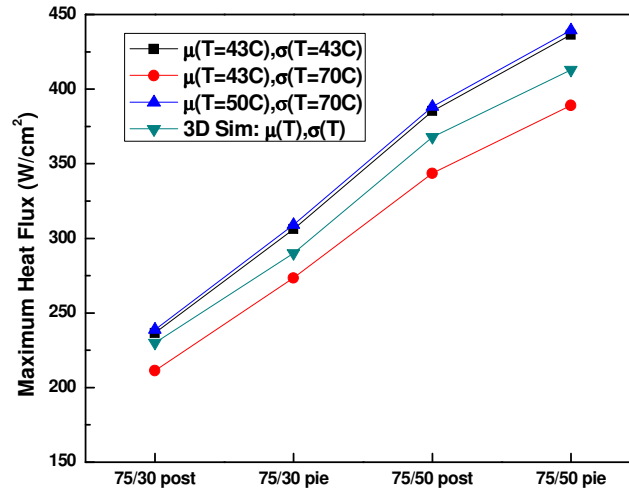
Figure 7.7: Maximum capillary limited heat flux ($5x5$mm^2 heater size), 100 μm tall structure, $7°$

contact angle.

The experimental heat transfer results of the 100 μm tall Cu structures with the super-hydrophilic CuO nanostructures are shown in Fig. 7.8 where wall superheat is plotted against heat flux from the heater. T_{wall} is the temperature at the plane of the structure/substrate intersection at the center of the heater. It is determined with a 3D numerical model to account for heat spreading between the heater and the substrate (see Chapter 5 for more details). The wick with the largest liquid supply, the 75/50 pie, achieves a critical heat flux higher than 175W/cm^2. The 75/30 pie and 75/50 post both reach a CHF of approximately 150-170 W/cm^2. The 75/30 post structure, with the lowest permeability, reaches CHF at 70W/cm^2. For the wicks that achieve a heat flux of at least 90W/cm^2, a sharp increase in performance is noted in which an increase in heat flux results in near zero or negative wall superheat increase. The below predicted maximum heat performance of the 75/30 post structure is thought to be due to the local dry out associated with the low liquid supply capability. In all cases, the maximum heat flux is less than predicted in Figure 7.7. This is discussed later in the chapter in the "Discussion of Different Heat Flux Regimes" section.
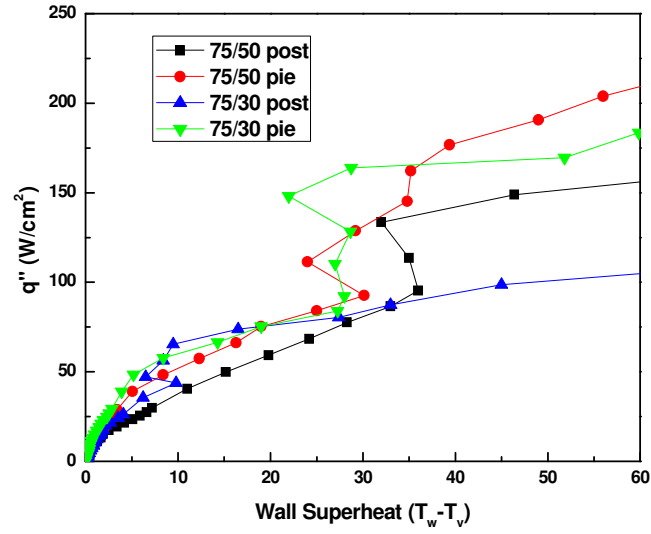
Figure 7.8: Experimental Heat Transfer Results for optimized 100 μm tall Cu structures

(Iteration 2) with super-hydrophilic oxide coating.

Effect of Super-hydrophilic surface

The effect of the super-hydrophilic CuO nanostructure is to increase liquid supply capability (Fig. 7.4) and minimize thermal resistance. This agrees with the previous results of Nam [62]. At the low and mid heat flux levels, the increased liquid supply capability associated with the nanostructure is thought to prevent local liquid dryout, hence a smaller thermal resistance is measured for corresponding wicks with the oxide structure. The 75/50 bare Cu pie achieves a heat flux of approximately ~100 W/cm^2 (Figure 7.9). Water on clean, bare Cu has a contact angle of approximately 80° [67]. Bare Cu liquid supply is estimated to be about 5 times less than a similar structure with a super-hydrophilic coating (Fig. 7.4). Therefore, the capillary heat flux limit for bare Cu structures should also be ~5 times lower than a similar hydrophilic

coated sample. The estimated capillary limit heat flux for the 75/50 bare Cu pie is ~84 W/cm^2, close to the ~100 W/cm^2 measured during our experiment.
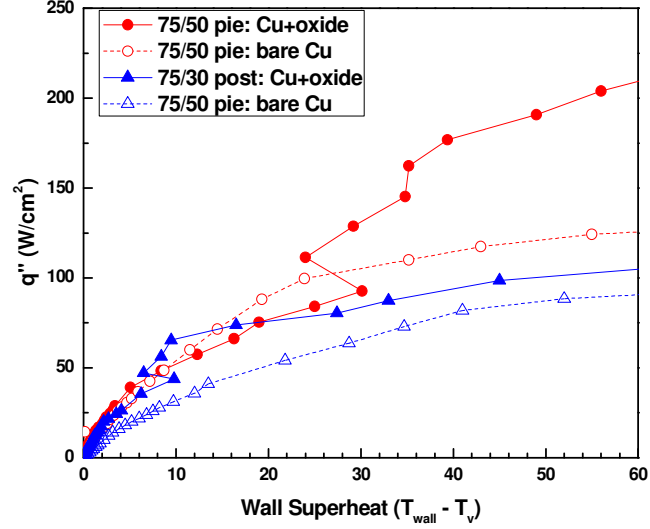
Figure 7.9: Experimental heat transfer results for optimized structures with and without super-

hydrophilic oxide coating.

Effect of Si Structure Height

The performance of the hydrophilic Cu and Si structures is presented for the 75/30 pie case (Fig. 7.10). The estimated capillary dryout for the 200μm tall Si pie (75/30) structure should be ~2x greater than that of the identical 100μm tall structure. Experimentally, the 200μm tall structure achieves a maximum heat flux of only about 50% greater than the 100μm tall structure. The reason for this divergence is discussed later in the chapter in the "Discussion of Different Heat Flux Regimes" section.
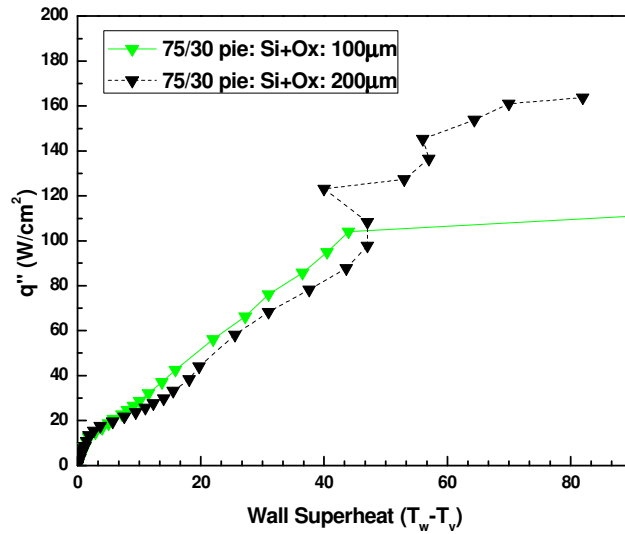
Figure 7.10: Experimental Heat Transfer Results for 75/30 pie structure: 100 μm and 200 μm

tall Si +hydrophilic SiO$_2$ coating.

Discussion of Different Heat Flux Regimes

The heat flux removal mechanism in the evaporator varies depending on the heat flux and

superheat. Figures 7.8 – 7.11 show that for the various samples, below ~80W/cm^2 the superheat

increases with increasing heat flux.   Above 80W/cm^2 the heat transfer phenomena begins to

drastically change and superheat may not increase with increasing heat flux – there may even be

increases in heat flux that result in decreases in superheat. Then above 120W/cm^2 a regime can

exist in which heat flux increases with approximately zero change in superheat. Finally, the

wick experiences dryout after this phase. Previous researchers have experimentally witnessed

this trend as well [92-94]. In the upcoming section, a discussion of what is occurring in these

various regimes is presented. Two example geometries are used for this discussion: 200 μm tall,

Si 75/50 post and 75/50 pie, with thermal oxide coating.   The Cu structures will be discussed as well.
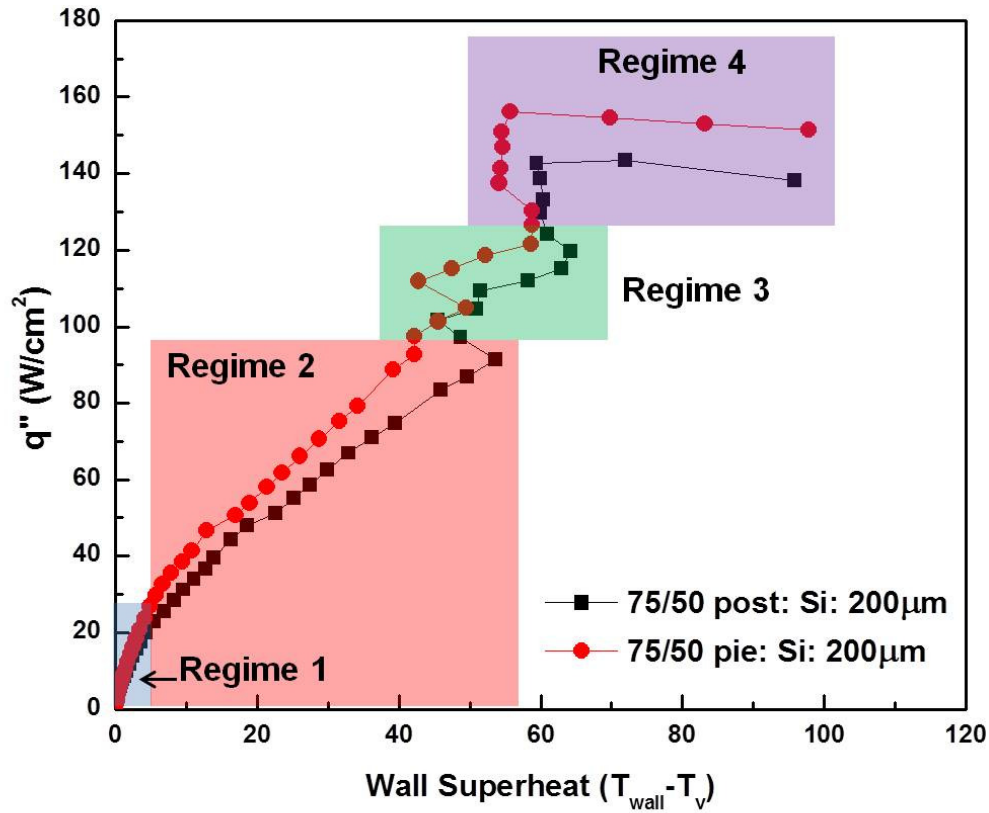
Figure 7.11: Experimental heat transfer results for 200 μm tall Si geometries with thermal oxide layer, four different heat transfer regimes have are discussed.

Regime 1 and 2: Low Flux

Regime 1, corresponding to super heats less than 5ºC and heat fluxes of ~25 W/cm^2, was discussed in depth in Chapter 6. Notice that the pie geometry has a larger slope due to the increased interline area. Regime 2, corresponding to superheats between 5-55 ºC and heat fluxes between 25 – 90W/cm^2 (roughly), is similar to Regime 1 in that a large portion of the heat transfer is expected to occur due to evaporation at the liquid-vapor interface near the top of the

posts. However, Regime 2 does show a decrease in slope and effective heat transfer coefficient. Semenic [52] noted that bubble nucleation in biporous wick began at heat fluxes of approximately 20W/cm^2 and superheats of ~5°C. While bubble nucleation or departure was not visibly noticed on the liquid-vapor interface during Regime 1 or 2, we did visually witness a change in the surface contrast as the heat flux increased (Fig. 7.12). This change in surface contrast can be due to the changing meniscus shape or the possibility of bubble growth at the substrate. The high interline area sample (75/50 pie) is shown to have a better performance than the lower interline area geometry in this regime.

Regime 3: Mid Flux Levels

Si wicks with large liquid supply ability will experience a sudden decrease in wick superheat at approximately 40-60°C superheat or heat flux of 85W/cm^2 (Fig. 7.11 and 7.12). In the 200 μm tall 75/50 Pie and Post Si structures, the decrease in superheat is accompanied by the appearance of a dryout area occurring suddenly, as at heat fluxes slightly less than 85W/cm^2 there is no visible dryout (Fig. 7.12). In the hydrophilic Cu wicks, regime 3 started at a slightly lower 30°C superheat, consistent with previous results on similar surfaces [62]. This difference in superheat is thought to be due to the difference in surface quality. The SiO$_2$ surface should be relatively smooth and uniform with a high surface energy corresponding to contact angles less than 20°. The CuO oxide structure, however, has a complicated 3D structure (Fig. 4.7) which helps decrease the contact angle to approximately 7°. However, the contact angle of water on a smooth CuO surface is estimated to be ~46° [24]. Therefore, the lower superheat required to enter regime 3 for the Cu samples may be due to small defects in the oxide layer or the lower surface energy of the CuO surface which allows for lower temperature requirements for bubble nucleation.

The dryout area is slightly larger than the 5x5mm^2 heater area size and the border between the saturated and dry portions of the wick is seen to be unstable and moves sporadically with time. As the heat flux increases, bubble nucleation can be seen on the saturated/unsaturated border (Fig. 7.12). The sudden dryout and resulting boiling at the interface cause the superheat to actually drop even as heat flux is increased (Fig. 7.11). After the initial superheat decrease, the superheat then increases with increasing heat flux until the next major change in heat transfer physics (the start of Regime 4).

Regime 4: High Flux Level and Dryout

At a superheat of ~55-60°C and heat flux of 125-170W/cm^2, the start of a strong and vigorous boiling and violent fluid ejection regime from the wick surface is seen (Fig. 7.12). The fluid ejection results in droplets that can shoot over 10cm from the wick surface. Unfortunately, the droplets land on the chamber window, partially blocking the view. This violent boiling and ejection regime is very efficient as a heat removal mechanism, and the superheat remains constant even as the superheat is increased (Fig. 7.11). The Cu post/pie structures go through the same type of violent fluid ejection regime as well. However, the Cu structures go through this regime at a much lower superheat (~30°C). Nam witnessed this regime at approximately a 20°C superheat in his experiments using the same hydrophilic CuO coating on Cu posts [62]. After passing through this stage, the wick experiences critical heat flux in which any increase in heat flux results in large increases in wick superheat which would result in overall device failure.
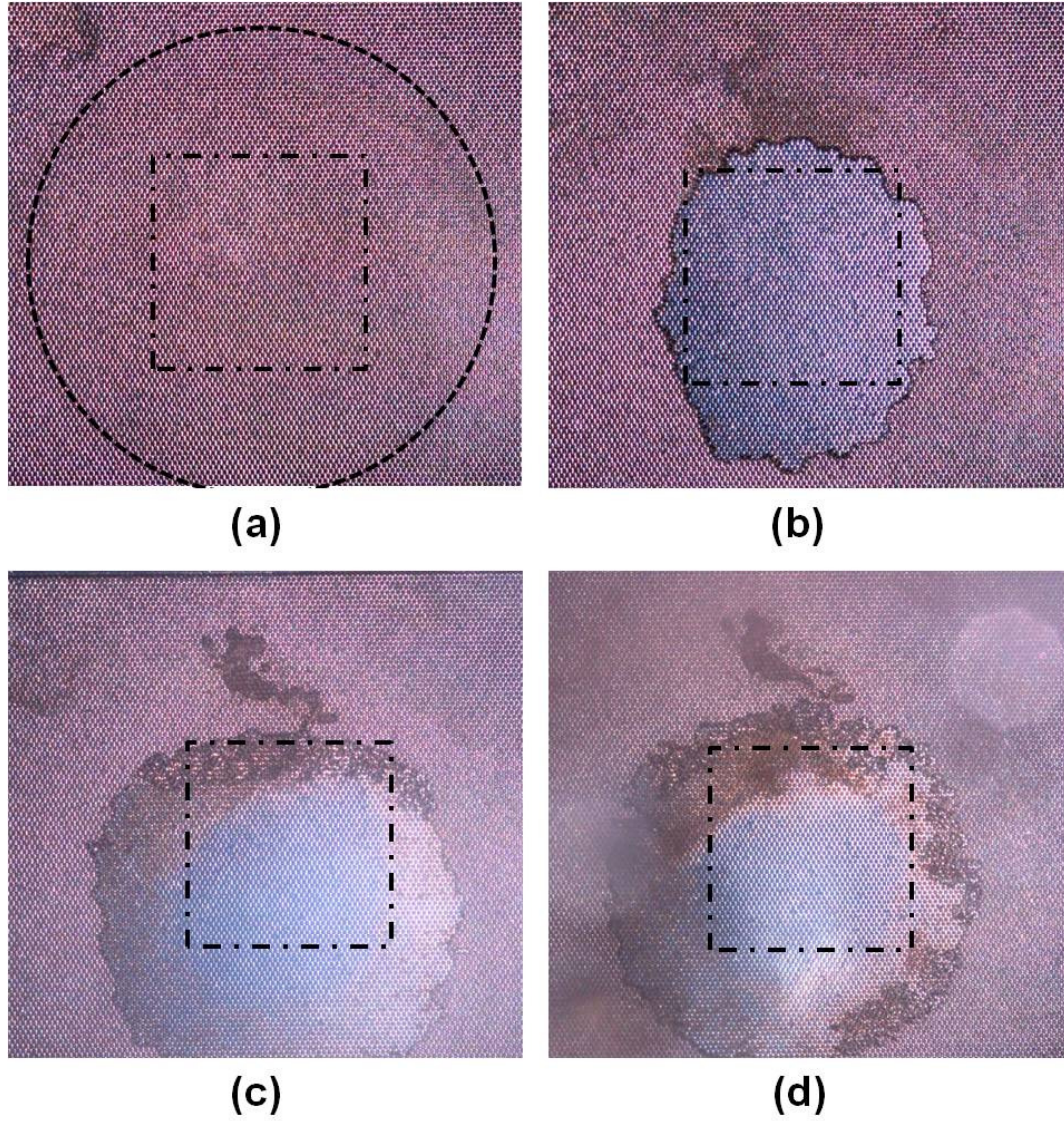
Figure 7.12: Si, 200 μm Pie structures during operation. a) regime 2: q" =75W/cm^2, b) regime 3: q" = 83W/cm^2, c) regime 3: q" = 105W/cm^2, d) regime 4: q" = 133W/cm^2. Black squares represent 5x5mm^2 heater location and size.

7.5   Summary

We utilized the static meniscus model to calculate the 3D meniscus shape in an advanced wick array and then predict the permeability, capillary pressure, liquid supply, and capillary limited heat flux. Optimized structures based on increasing the liquid supply and maximum heat flux are fabricated with both Cu and Si using traditional micro-fabrication techniques. Critical heat fluxes higher than 170W/cm^2 are achieved for the optimized samples and improvements over the baseline post geometries are seen. The effect of surface wettability is also studied: the super-hydrophilic coated structures achieve a higher maximum heat flux than their bare counterparts, but less than predicted by the capillary limit model. A boiling and fluid ejection regime are witnessed at high superheats (~30°C for Cu structures and ~40°Cfor Si structures) which result in efficient heat dissipation, but also disrupt the fluid flow to the evaporator. This blockage also limits the performance of tall (200μm) Si structures, which show only a 50% increase over their shorter (100μm) counterparts. The work presented here can be utilized for optimizing thin wick structures for lightweight thermal solutions.

CHAPTER 8

LED Cooling: Wicks on Printed Circuit Board (PCB) Substrates

Growing demand for LED lighting systems has increased the need for integrated cooling solutions to keep the LED at an appropriate temperature. Typical thermal solutions involve multiple heat spreader layers and thermal interface materials. Here we present our work in developing an integrated vapor chamber concept which is connected to the LED device without any polymer-based thermal interface material. We use our copper deposition fabrication process to construct a wick on a copper plated PCB board and the integrated thermal via. The thermal via is in direct contact with the LED device via a solder layer. A commercially available dielectric fluid is used as the working fluid to prevent electronic short circuiting. The static meniscus model is used to predict the heat transfer coefficients of the integrated wick on the thermal via and the results are compared to experimental testing. The work presented here can be used to develop powerful cooling solutions for high heat flux LEDs.

8.1   Background

The efficiency, output wavelength, and lifetime of an LED are related to its operating temperature [82]. As LEDs become a more popular solution for lighting applications, providing thermal solutions becomes more important. Incandescent light bulbs operate by heating a filament wire until it glows. Almost all the dissipated energy (including visible light) leaves as electromagnetic radiation. LEDs, on the other hand, operate at a much lower temperature. Therefore, radiation is not a viable heat dissipation mechanism. Only conduction through the backside of the LED package is available for significant heat dissipation [82,83].

A high brightness LED (HBLED) system consists of the LED die mounted to a solid conduction thermal spreader mounted to a PCB board attached to a heat sink (Fig. 8.1). The commercially available Philips Fortimo LED picture shown below consists of and LED unit mounted onto a PCB substrate, connected via a TIM to a high thermal conductivity aluminum board which is then connected via another TIM to an air-cooled heat sink [84]. The aluminum heat sink can be quite large relative to the LED/board combination (Fig. 8.1). As the demand for high brightness LEDs increases, replacing typical thermal solutions (such as solid thermal conductivity heat spreaders) may be a viable and necessary option.
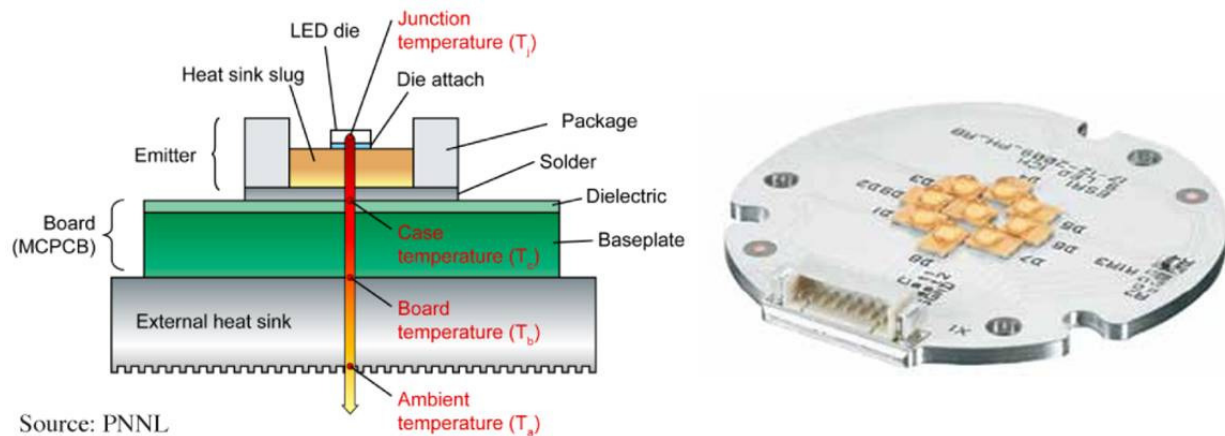
Figure 8.1: Left side shows schematic of a typical high flux LED system [82], Right side shows Philips Fortimo LED and Aluminum cooling plate [84].

HBLEDs are becoming more common in LED lamps, display backlighting, and camera flashes [75]. Today's typical die size may be on the order of $1mm^2$ and the total power requirement may be 1W. Assuming a 80% power to thermal energy conversation rate [82], the heat flux requirement may be as high as $80W/cm^2$. In the near future, this heat flux requirement is expected to be as high as $340 W/cm^2$ [85].

Our proposed solution makes use of an integrated vapor chamber/heat spreader which is linked directly to the LED device via a Cu thermal via (Fig. 8.2 and 8.3). The wick is constructed directly onto the thermal via and copper clad PCB backside. The backside of the LED may be covered with electrical arrays for power and sensor signals. The dielectric working fluid is chosen so as to prevent short circuiting – eliminating the need for a ceramic isolating material and the associated thermal resistance.   This design schemes removes the need for several layers of TIM and also takes advantage of the large thermal conductivity associated with phase change thermal spreaders as well as the ability to effectively cool at high dissipated heat fluxes.
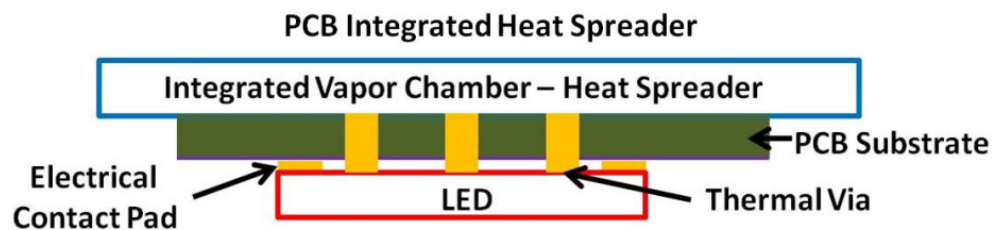
Figure 8.2: Proposed HBLED cooling solution using integrated vapor chamber.
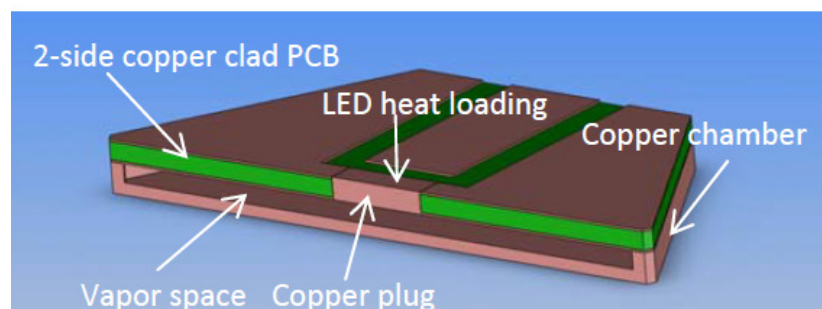
Figure 8.3. Proposed HBLED cooling solution with integrated vapor chamber: cross sectional

side view [83]

At the system level, fin-heat sinks with active air cooling is currently the most common thermal solution given its high reliability and low cost [86,87]. Active liquid cooling solutions have become attractive as heat flux requirement continues to increase [87]. Although typical heat pipe/vapor chamber setups can easily replace traditional solid conduction heat spreaders, the device proposed here is unique in that the thermal solution is connected directly to the thermal via and PCB substrate without the need for any TIM. This technology has the ability to improve LED thermal performance and potentially simplifying complex LED packaging.

8.2   Sample Details – substrate description and fabrication procedure

While phase change vapor chambers and heat spreads provide an ideal solution for LED applications, the low temperature requirement of the printed circuit board (PCB) makes traditional high-temperature wick fabrication methods, such as sintering particles or wire mesh, infeasible. The PCBs are typically composed of a fiberglass and resin combination resulting in a lower thermal conductivity substrate. Here we utilize a popular FR-4 woven fiberglass and epoxy resin board. The FR-4 has a thermal conductivity of 0.27 W/mK and has a temperature maximum of 140°C before going through a glass transition at which point the board loses its structural integrity [88]. The deposited Cu layer atop the PCB has a Cu thickness of approximately 350 nm. Holes for the thermal vias are drilled and tightly fitting Cu slugs are inserted. Both sides of the whole device are then Cu plated again to ensure a hermetic seal.

Experimental samples are fabricated using our established electro-deposition technique (Chapter 4). We chose this fabrication process so as to limit the maximum temperature seen by the PCB board to 100°C. A 130 μm thick electroplating mask is spun onto the polished (near mirror finish) Cu clad PCB/thermal via substrate. Photolithography is used to etch the mask with

the desired pattern (wick area is 2.5 x 2.5 cm). Electroplating mask adhesion to the Cu surface is

a function of the surface quality of the surface. Scratches or unevenness can result in premature

mold lift-off, especially at the via/substrate interface. Copper is electroplated through the mask

holes at a current density of approximately 5mA/cm^2 to form the desired wick structure.

The 75/50 post, 120 µm height, structure was successfully fabricated on both polished

and non-polished Cu clad PCB substrates (Fig 8.4). On near-mirror quality polished samples

(Fig. 8.5), plating posts onto the thermal via – PCB interface was achieved. However, roughness

at the thermal via – PCB interface resulted in missing posts due to poor electroplating mold

integrity (Fig. 8.6).
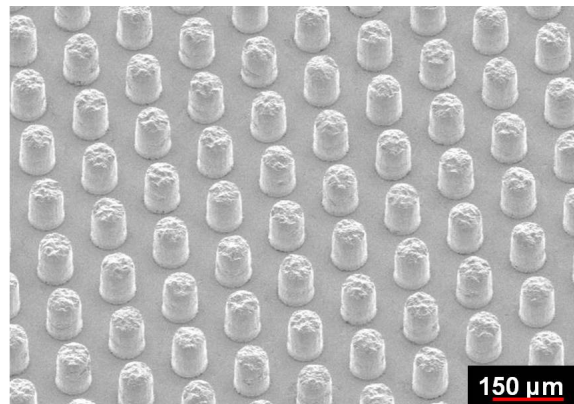
Figure 8.4: 75um post diameter, 50um edge-to-edge spacing, 120 µm post height, Cu Post Wick

Geometry on unpolished Cu clad PCB substrate
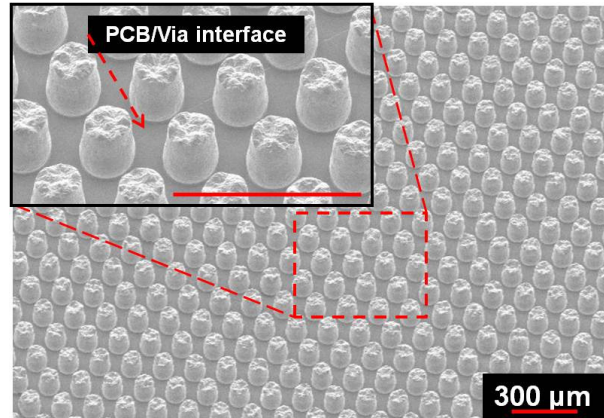
Figure 8.5: Posts at the thermal via/PCB substrate interface on polished substrate.
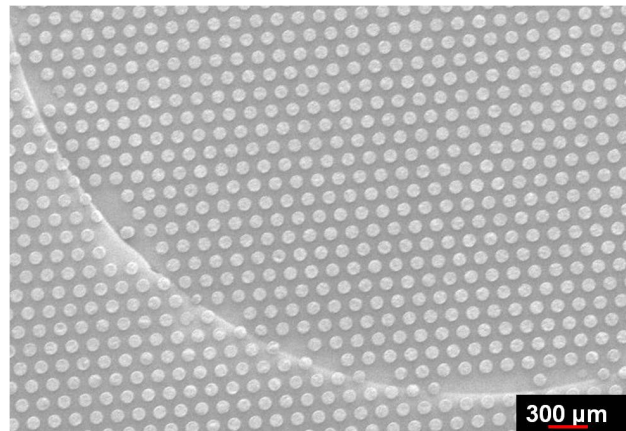
Figure 8.6: Missing posts at the thermal via/PCB substrate interface on the un-polished

substrate, damaging thermal performance.

8.3   Working Fluid Description

The fluid properties used in our simulations and experiments are presented in Table 8.1.

Compared to water, the dielectric fluids have enthalpies of vaporization and thermal

conductivities of approximately an order of magnitude less than those of water. The surface

tension of the dielectrics is also very low, resulting in well-wetting properties similar to those of

methanol.

Table 8.1: Summary of thermo-fluid properties of dielectric fluids.

Properties	Dielectric Fluids			
	3M-7200 [89]	3M-72DE [90]	3M-7100 [89]	Water [18]
ρ (kg/m^3)	1430	1280	1510	997
μ (mPa*s)	5.8	4.4	5.8	8.91
h_{fg} (kJ/kg)	125	217	112	2441.7
σ (mN/m)	13.6	19	13.6	72
T_{sat} (°C at 1atm)	76	43	61	100
k (W/mK)	0.068	~0.07-0.1	0.068	0.6
M (W/cm^2)	3.8 x10^4	1.2x10^5	2.5 x10^4	2.0x10^6

8.4   Results and Discussion

Liquid Supply

The results of our static meniscus modeling are presented first. Due to the low surface tension of the 3M Novek 7100 dielectric fluid, contact angles approaching 0° are expected. Using our static meniscus modeling, maximum capillary pressures of 0.6kPa and 0.34kPa are predicted for the 75/30 and 75/50 cases, respectively

Effective Heat Transfer Coefficient and Superheats

The predicted h_{eff} values calculated using the static meniscus model are shown in Fig. 8.7. Using Novec 7200 as the working fluid, expected values of h_{eff} range between 0.5-1.25 W/cm^{2}K are expected for the 75/50 post geometry. Approximately 20% higher values are expected for the 75/30 post geometry due to the decreasing solid conduction and liquid resistance associated with a higher solid fraction and higher normalized thin film area, respectively. Our modeling optimization scheme shows that due to the low thermal conductivity of 7200 fluid compared to water (~10x lower than water), the liquid-side conduction resistance can be a dominant term in the wick thermal resistance. For this reason, increasing the interline area available for evaporation results in decreased overall thermal resistance. The 75/30 pie structure has a large solid fraction so that for all predicted liquid side conditions it still takes advantage of its high interline region.
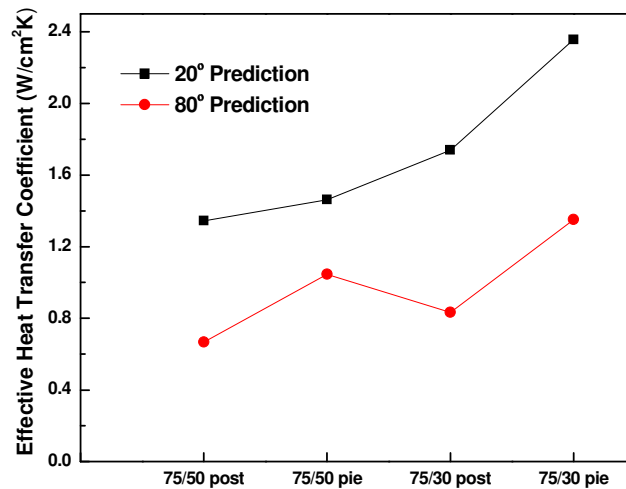
Figure 8.7: h_{eff} predicted by the static meniscus model for 3M Novek 7200 Dielectric Fluid.

The predicted superheat required to remove a heat flux of 50W/cm^2 is shown in Fig. 8.8. The superheat is calculated assuming the LED heat dissipation occurs over the same area as the thermal via (no 3D heat spreading in the thermal via) and no spreading on the wick surface due the low thermal conductivity of the PCB substrate and very thin Cu layer. Therefore, a 1D approximation can be made and the superheat calculated as q"x $1/h_{eff}$. Depending on the liquid-side contact angle, the resulting superheat for the 75/50 post structure is expected to vary between 37 and 75°C. However, by utilizing an optimized interline geometry such as the 75/30 pie, the superheat is expected to decrease to between 20-40°C for all liquid-side conditions. As heat flux increases, the effect of the increased interline region can significantly decrease the required superheat.
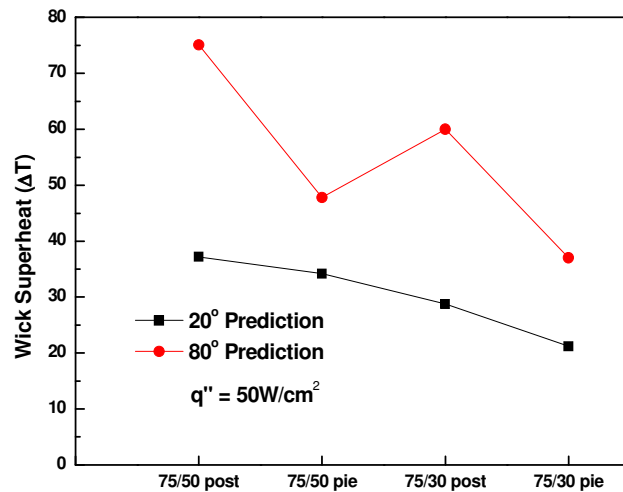
Figure 8.8: Wick superheat predicted by the static meniscus model for 3M Novek 7200 Dielectric fluid.

We test our modeling efforts using the same experimental setup as described in Chapter 5. However, instead of using the PCB integrated wick with thermal via, we instead use our bare Cu wick as described in Chapter 4. The 75/30 pie geometry is tested using both 7200 and 72DE dielectric fluids from 3M. Given the low Merit numbers of these fluids, CHF is reached at relatively low values (compared to water). The 7200 fluid results in dryout at approximately $6W/cm^2$ and the 72DE at $15W/cm^2$. This agrees well to the capillary-viscous balance of Eqn. 2.2. Both results were achieved using a $5x5mm^2$. This heater size is large compared to most LED die sizes. It is estimated that a $5mm^2$ heater area would achieve heat fluxes 30 and 75 W/cm^2 for the 7200 and 72DE fluids, respectively. Assuming the capillary limit governs dryout, a $1mm^2$ die size would achieve critical values of over $100 W/cm^2$ for the 7200 fluid and much higher for the 72DE.

The effective heat transfer coefficient of the 72DE test is larger than the 7200 due to the higher thermal conductivity of the 72DE fluid (~0.1W/mK vs 0.068 W/mK, respectively). However, the predicted h_{eff} values differ from the experimentally determined values. One reason for this may be that the static meniscus assumption is no longer valid due to the low surface tension and low enthalpy of vaporization of the dielectric fluid. Compared to water, the dielectric fluid will require much more fluid pumping to the thin film region due to the low thermal conductivity and enthalpy of vaporization, likely resulting in large meniscus deformation away from the static shape. Assuming identical meniscus shapes and flow conditions to those of water, the Weber number ratio (ratio of inertia to surface tension forces) of the 7200 dielectric fluid to that of water is less than 0.01, showing that the relative inertia effect is much stronger in the dielectric fluids.
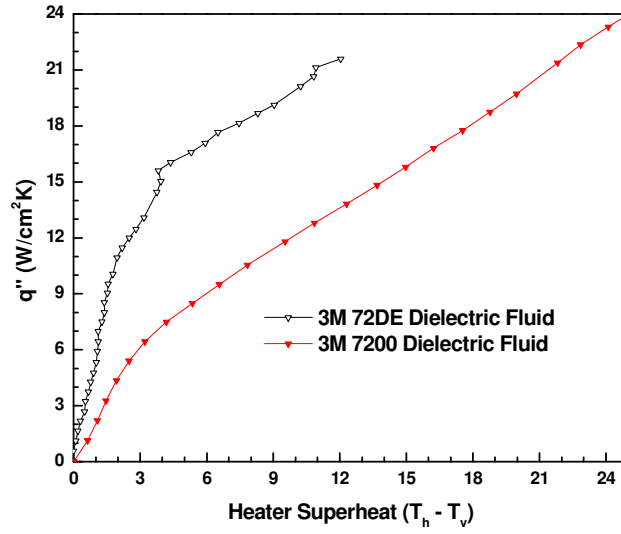
Figure 8.9: Experimental Superheat of as a function of heat flux using dielectric fluids.

8.5   Summary

The work presented in this chapter can be used as an innovative cooling solution for LED lighting applications. Due to the packaging and heat flux requirements, phase change thermal spreaders integrated directly to the LED package may provide an ideal option for cooling solutions. We have shown that wick fabrication directly onto the Cu clad PCB substrate as well as the thermal via can be performed using our micropost deposition method. This eliminates the need for several TIM layers. We have also shown that the dielectric fluid and wick combination we have chosen are capable of removing very large heat fluxes (+100W/cm^2) for small die sizes.

CHAPTER 9

Conclusion

This thesis has presented new research in the field of thermal management of high heat flux electronic components. More specifically, phase change heat transfer on low-profile structured surfaces for vapor chamber applications has been studied and presented. Key results are based on a three-pronged approach: modeling, fabrication, and experimental validation.

A static meniscus model was developed using a surface energy minimization algorithm to determine the shape of a 3D liquid meniscus resulting from fluid interaction with a complex solid structure. This 3D meniscus could then be used to determine the capillary pressure and also predict the permeability and effective heat transfer coefficient. Knowledge of the capillary pressure and permeability allows the determination of the wick's liquid supply, a direct predictor of critical heat flux. To determine the validity of this model, well defined geometries are fabricated.

Traditional micro-manufacturing techniques are utilized to develop well-controlled wick structures. Three different fabrication methods are utilized: "traditional" sintering, etched micro Si structures, and electroplated Cu through micro pores. Sintering is the most common fabrication method for wicks in industry, but can suffer from intra sample variability associated with particle size distributions and packing. With the etched Si structures, extremely high aspect ratio structures (>20) can be developed easily and quickly. However, the nominal thermal conductivity of Si can limit the effective heat transfer performance. The deposited Cu structures achieved aspect ratios as high as five. However, the relatively high thermal conductivity of Cu

allows for extremely high effective heat transfer coefficients. After fabrication, these wick structures are experimentally tested.

Experimental testing of the fabricated wicks is used to validate our modeling techniques. A copper vacuum chamber provided a controlled saturation pressure and temperature. The wick was held in a vertical orientation to prevent flooding and an input heat flux was provided by a thin film heater. The experimental results agreed with our modeling predictions.

In addition, a novel vapor phase change device for cooling LEDs with limited thermal interface materials was presented. The wick was integrated directly onto the PCB substrate and relevant dielectric fluids were tested for experimental verification.

The key conclusions of this work are as follows:

1. The static meniscus model is an accurate and efficient method of predicting wick liquid supply and effective heat transfer coefficient, though the assumptions made for the heat transfer coefficient are only valid at low heat fluxes.

2. The effective heat transfer coefficient is a strong function of solid conduction resistance and interline area. The static meniscus method can be used to optimize the heat transfer coefficient and liquid supply.

3. Using hexagonally packed cylinders as a baseline case (same nominal diameter, same pitch), optimized structures can be developed which feature a higher permeability due to lower solid fraction, but also lower thermal resistance due to the effect of increasing the interline region area.

4. The monolayer of sintered spheres showed the best performance for particles with diameters of ~60 μm – a critical heat flux of ~80W/cm^2 was achieved.

5. Optimized silicon wick were fabricated using an etching method that allowed for high aspect ratio structures and boiling visualization.

6. Copper structures were fabricated using an electro-deposition technique. The optimized "pie" geometry showed increases in CHF and effective heat transfer coefficient. CHF as high as 170 W/cm2K and effective heat transfer coefficients > 12W/cm^{2}K were achieved.

7. A novel LED cooling method was demonstrated. The low-temperature Cu deposition process was used to integrate a wick structure to a copper clad PCB board with thermal via. Using a dielectric as the working fluid, heat fluxes as high as 15W/cm^2 are effectively dissipated.

References

1. Kanellos, M., 2003, "Intel Scientists Find Wall for Moore's Law," CNET News. Published December 1, 2003, <news.cnet.com/2100-1008-5112061.html>.

2. Walker, J., 2011, "Handbook of RF and Microwave Power Amplifiers", Cambridge University Press.

3. Banerjee, K., Souri, S., Kapur, P., and Saraswat, K., 2001, "3-D ICs: A Novel Chip Design for Improving Deep-Submicrometer Interconnect Performance and Systems-on-Chip Integration," *Proceedings of the IEEE*, May (89) no. 5.

4. Koo, J.M., Im, S., Jiang, L, and Goodson, K., 2005, "Integrated Microchannel Cooling for Three-Dimensional Electronic Circuit Architectures," *Journal of Heat Transfer,* January (127).

5. BCC Research and Market Forecasting, 2012, "Top Ten Thermal Management Companies and Emerging Transformative Technologies," January 2012, Report Code: SMC075A.

6. Wilson, J., 2003, "Challenges in Thermal Control of Military Electronics Systems," *Electronics Cooling,* Accessed May 2012, <http://www.electronics-cooling.com/2003/02/challenges-in-thermal-control-of-military-electronics-systems/>.

7. Kanbach, H., Wilde, J., Kriebel, F., and Meusel, E., 2000, "3D Si-on-Si Stack Packaging," *Soldering & Surface Mount Technololgy*, December, pp. 35-39.

8. Lasance, C., and Simons, R., 2005, "Advances in High-Performance Cooling for Electronics", *Electronics Cooling*, Accessed online May 2012, <www.electronics-cooling.com/2005/11/advances-in-high-performance-cooling-for-electronics/>.

9. Wang, E., et al., 2004, "Micromachined Jets for Liquid Impingement Cooling of VLSI Chips", *Journal of Microelectromechanical Systems*, October (13) No. 5.

10. Sung, M.K. and Mudawar, I., 2009, "CHF Determination for high-heat flux phase change cooling system incorporating both micro-channel flow and jet impingement," *International Journal of Heat and Mass Transfer*, (52) pp. 610-619.

11. Morini, G.L., 2004, "Single-Phase Convective Heat Transfer in Microchannels: A Review of Experimental Results," International Journal of Thermal Sciences, 43, pp. 631-651.

12. Garimella, S., and Sobhan, C., 2003, "Transport in Microchannels – A critical review," *Annual Review of Heat Transfer*, (13) pp. 1-50.

13. Gillot, C., Schaeffer, C., and Bricard, A., 2000, "Integrated Micro Heat Sink for Power Multichip Module," *IEEE Transactions of Industry Applications*, (36) no. 1.

14. North, M., and Cho, W.L., 2003, "High Heat Flux Liquid-Cooled Porous Metal Heat Sink," *ASME 2003 International Electronic Packaging Technical Conference and Exhibition*, IPack2003-35320, pp 681-686.

15. Kaviany, M., 1995, *Principles of Heat Transfer in Porous Media*", 2nd Edition, Springer.

16. Chi, S.W., 1976, *Heat Pipe Theory and Practice*.

17. Holley, B., and Faghri, A., 2005, "Permeability and Effective Pore Radius Measurements for Heat Pipe and Fuel Cell Applications," *Applied Thermal Engineering*, 26, pp. 448-462.

18. Mills, A., 1992, *Heat Transfer*, First Edition.

19. Sarraf, D., and Anderson, W., 2007, "Heat Pipes for High Temperature Thermal Management," *Proceedings of IPACK 2007,* IPACK2007-33984.

20. Washburn, E.W., 1921, "The Dynamics of Capillary Flow," *Physics Review*, 17(3).

21. Dullien, F., 1979, *Porous Media: Fluid Transport and Pore Structure*, Academic Publishing.

22. Carman, P.C., 1937, "The Determination of the Specific Surface Area of Powder I", *Journal of the Society of Chemical Industries*, (57) pp. 225-234.

23. Ranjan, R., Murthy, J., Garimella, S., 2009, "Analysis of the Wicking and Thin-Film Evaporation Characteristics of Microstructures," *Journal of Heat Transfer*, 131.

24. Nam, Y., Sharratt, S., Byon, C., Kim, S.J., Ju, Y.S, 2010, "Fabrication and Characterization of the Capillary Performance of Superhydrophilic Cu Micropost Arrays," *Journal of Microelectromechanical Systems*, 19 no. 3, pp. 581-589.

25. Xiao, R., Enright, R., and Wang, E., 2010, "Prediction and Optimization of Liquid Propagation in Micropillar Arrays," *Langmuir Letter*, 26(19), pp 15070-15075.

26. Brakke, Kenneth, 1992, "The Surface Evolver," *Experimental Mathematics*, 1.

27. Carey, Van P., 2008, *Liquid-Vapor Phase-Change Phenomena*, Second Edition.

28. Frommelt, Thomas et al., October 2008, "Flow Patters and Transport in Rayleigh Surface Acoustic Wave Streaming," *IEEE Transactions on Ultrasonics, Ferroelectrics, and Frequency Control*, 55.

29. Personal communications with Frommelt, Thomas occurring in October 2009.

30. Darcy, H., 1856, *Les Fontaines publiques de la ville de Dijon*. Paris: Dalmont.

31. Wang, H., Garimella, S., Murthy, J., 2007, "Characteristics of an Evaporating Thin Film in a Microchannel," *International Journal of Heat and Mass Transfer*, 50, pp. 3933 – 3942.

32. Wayner, P.C. Jr., 1991, "The Effect of Interfacial Mass Transport on Flow in Thin Liquid Films," *Colloids and Surfaces,* 52, pp. 71-84.

33. Stephan, P.C. and Busse, C.A., 1995, "Analysis of the Heat Transfer Coefficient of Grooved Heat Pipe Evaporator Walls," *International Journal of Heat and Mass Transfer*, 35. No 2., pp. 383-391.

34. Xu, X., Carey, V.P., 1990, "Film Evaporation from a Micro-Grooved Surface – An Approximate Heat Transfer Model and Its Comparison With Experimental Data," *Journal of Thermophysics and Heat Transfer*, 4, pp. 512-520.

35. Schonberg, J.A., DasGupta, S., and Wayner, P.C., 1995, "An Augmented Young-Laplace Model of an Evaporating Meniscus in a Microchannel with High Heat Flux," *Experimental Thermal and Fluid Science*, 10, pp. 163-170.

36. Ma, H.B., Cheng, P., Borgmeyer, B., and Wang, Y.X., 2008, "Fluid Flow and Heat Transfer in the Evaporating Thin Film Region," *Microfluid-Nanofluid*, 4, pp. 237 – 243.

37. Potash, M. Jr., and Wayner, P.C., 1972, "Evaporation from a Two-Dimensional Extended Meniscus," *International Journal of Heat and Mass Transfer*, 15, pp. 1851 – 1863.

38. Edwards, D.K, Balakrishnan, A., and Catton, Ivan, August 1974, "Power-Law Solutions for Evaporation from a Finned Surface," *Journal of Heat Transfer*, pp. 423 – 425.

39. Demsky, S.M. and Ma, H.B., 2004, "Thin Film Evaporation on a Curved Surface," *Microscale Thermophysical Engineering*, 8, pp. 285-299.

40. Mirzamoghadam, A., and Catton, I., 1988, "A Physical Model of the Evaporating Meniscus," *Journal of Heat Transfer*, 110, pp. 201 – 207.

41. Park, K., and Lee, K.S., Flow and Heat Transfer Characteristics of the Evaporating Extended Meniscus in a Micro-Capillary Channel, International Journal of Heat and Mass Transfer (46) (2003) (4587 – 4594).

42. Peterson, G.P., Swanson, L.W., Gerner, F., 1998, "Micro Heat Pipes," *Microscale Energy Transport*, Chapter 8.

43. Holm, F.W. and Goplen, S.P., 1979, "Heat Transfer in the Meniscus Thin Film Transition Region," *Journal of Heat* Transfer, (101) pp 543 – 547.

44. Hwang, G.S, Fleming, E., Carne, B., Nam, Y., Sharratt, S., Dussinger, P., Ju, Y.S, Kaviany, M, 2011, "Multi-Artery Heat Pipe Spreader: Lateral Liquid Supply," *International Journal of Heat and Mass Transfer*, (54) pp. 2334-2340.

45. Ma, Hanlon, Ma, H.B., 2003, "Evaporation Heat Transfer in Sintered Porous Media", *Journal of Heat Transfer*, 125, pp. 644 – 650.

46. Ranjan, R., Murthy, J., Garimella, A microscale model for thin-film evaporation in capillary wick structures, Int. J. Heat Mass Transfer 54 (1-3) (2011)169-179.

47. Ranjan, R., Murthy, J., Garimella, and U. Vadakkan, A numerical model for transport in flat heat pipes considering wick microstructure effects, International Journal of Heat and Mass Transfer (54) (2011) 153-168.

48. Marek, R., and Straub, J., Analysis of the evaporation coefficient and the condensation coefficient of water, International Journal of Heat and Mass Transfer 44 (2001) 39-53.

49. Mills, A.F. and Seban, R.A., 1967, "The Condensation Coefficient of Water," *International Journal of Heat and Mass Transfer,* 10, pp. 1815-1827.

50. Do, K.H., Kim, S.J., and Garimella, S., 2008, "A Mathematical Model for Analyzing the Thermal Characteristics of a Flat Micro Heat Pipe with a Grooved Wick," *International Journal of Heat and Mass Transfer*, 51, pp. 4637 – 4650.

51. NIST Standard Reference Data. <http://webbook.nist.gov/chemistry /fluid/>.

52. Semenic, T., Lin, Y.Y., Catton, I., Sarraf, D., 2006, "Use of biporous wicks to remove high heat fluxes," *Applied Thermal Engineering*, 28, pp. 278-283.

53. Jiao, A.J., Ma, H.B., and Crister, J.K., 2008, "Heat Transport Characteristics in a Miniature Flat Heat Pipe With Wire Core Wicks," *Journal of Heat Transfer*, 130.

54. German, R.M, 1996, *Sintering Theory and Practice*, John Wiley & Sons.

55. Lips, S., Lefevre, F., Bonjour, J., 2010, "Thermo-hydraulic Study of a Flat Plate Heat Pipe by Means of Confocal Microscopy: Application to a 2D Capillary Structure," *Journal of Heat Transfer*, 132.

56. Revellin, R., Rullière, R., Lefèvre, F., and Bonjour, J., 2009, "Experimental validation of an analytic model for predicting the thermal and hydrodynamic capabilities of flat micro heat pipes," Applied Thermal Engineering, 29, pp. 1114-1122.

57. <frostytech.com>. Accessed on September 2010.

58. Cai, Q. and Chen, C., 2010, "Design and Test of Carbon Nanotube Biwick Structure of High- Heat-Flux Phase Change Heat Transfer*, Journal of Heat Transfer*, 132.

59. Ding, C., Soni, G., Bozorgi P., Piorek, B., Meinhart, C., MacDonald, N., 2008, "A Titanium Based Flat Heat Pipe," *Proceedings of IMECE 2008*.

60. Reilly, S., and Catton, I., 2009, "Improving Biporous Heat Transfer by Addition of Monoporous Interface Layer," *Proceedings of the 2008 ASME Summer Heat Transfer Conference.*

61. Zhao, Y., Chen, C., 2006, "An Investigation of Evaporation Heat Transfer in Sintered Copper Wicks with Microgrooves," *Proceedings of IMECE2006*.

62. Nam, Y., Sharratt, S., Cha, G., Ju, Y.S, 2011, "Characterization of the Heat Transfer Performance of Nanostructured Cu Micropost Wicks," *Journal of Heat Transfer*, (133).

63. Qu, W., and Siu-Ho, A., 2008, "Liquid Single-Phase Flow in an Array of Micro-Pin Fins – Part I: Heat Transfer Characteristics," Journal of Heat Transfer, 130.

64. Weibel, J., Garimella, S., North, M., 2010, "Characterization of Evaporation and Boiling from Sintered Powder Wicks Fed by Capillary Action, "International Journal of Heat and Mass Transfer," 53, pp. 4203-4215.

65. Semenic, Tadej, 2007, "High Heat Flux Removal Using Biporous Heat Pipe Evaporators", PhD Thesis, UCLA.

66. Sharratt, S., Y. Nam, and Y.S. Ju, Liquid Supply and Heat Transfer Performance of Sintered Cu Monolayer Wicks for Phase Change Heat Transfer Applications, Proceedings of the ASME/JSME 2011 8th Thermal Engineering Joint Conference, AJTEC2011-44356.

67. Nam, Y., Ju., Y.S, 2008, "Comparative Study of Copper Oxidation Schemes and Their Effects of Surface Wettability," Proceedings of IMECE 2008, IMECE2008-67492.

68. Kurokawa, Y. and Utsumi, H.T., 2005, "Development and Microstructural Characterization of High-Thermal-Conductivity Aluminum Nitride Ceramics", *Jounral of the American Ceramic Society*, (71) issue 7, pp. 588-594.

69. Stellar Industries, Accessed 2011, < http://www.stellarind.com/products/ceramics/ aluminum_nitride.html>.

70. Qu, W., and Siu-Ho, A., 2008, "Liquid Single-Phase Flow in an Array of Micro-Pin Fins – Part II: Pressure Drop Characteristics," Journal of Heat Transfer, 130.

71. Vasiliev, L.L., 2008, "Micro and Miniature Heat Pipes – Electronic Component Coolers." *Applied Thermal Engineering*. 28, pp. 266-273.

72. Bock, P., Varanasi, K., Chamarthy, P., Deng, T., Kulkarni, A,. Rush, B., Russ, B., Weaver, S., and Gerner, F., 2008, "Experimental Investigation of Micro/Nano Heat Pipe Wick Structures," *Proceedings of IMEMCE 2008*, IMECE2008-67288.

73. Fries, N., Odic, K., Conrath, M., Dreyer, M., 2008, "The Effect of Evaporation on the Wicking of Liquids in to a Metallic Weave," *Journal of Colloid and Interface Science*, 321, pp. 118-129.

74. Li, C., Peterson, G.P., Wang, Y., "Evaporation/Boiling in Thin Capillary Wicks (I) – Wick Thickness Effects", *Journal of Heat Transfer*, 128, pp. 1312 – 1319.

75. Reilly, S., and Catton, I., 2011, "Utilization of Advanced Working Fluids with Biporous Evaporators", *Journal of Thermal Science and Engineering Applications*, (3), issue 2.

76. Iverson, B., Davis, T., Garimella, S., North, M., and Kang, S., 2007, "Heat and Mass Transport in Heat Pipe Wick Structures," *Journal of Thermophysics and Heat Transfer, vol. 21, no. 2.*

77. Indium Corp. of America, 2012, "Product Data Sheet: Solder Ribbon and Foil."

78. Omega Corp., "OMEGABOND 101 Epoxy Adhesive User's Guide."

79. Hwang, G.S., Kavinay, M., Anderson, W.G., Zuo, J, 2007, "Modulated wick heat pipe," *International Journal of Heat and Mass Transport*, 50, pp. 1420 – 1434.

80. Min, D.H., Hwang, G.S., Kaviany, M, 2009, "Multi-artery, heat pipe spreader," *International Journal of Heat and Mass Transfer*, 52, pp. 629-635.

81. Sharratt, S., Peng., C., Ju, Y.S., 2012, "Micro-Post Wicks with Modified Geometries for Improved Phase Change Heat Transfer Performance," *International Journal of Heat and Mass Transfer*, to be published.

82. EERE, "Thermal Management of White LEDs," June 2009, PNNL-SA-51901.

83. Fan, A., Bonner, R., Sharratt, S., and Ju, Y.S., 2012, "An Innovative Passive Cooling Method for High Performance Light-emitting Diodes," *Proceedings of 28th IEEE SEMI-THERM* Symposium.

84. Philips, "Philips Fortimo LED Spotlight Module System: Design-in Guide", Accessed November 2011.

85. Zhang, J., Niu, P., Gao, D., and Sun, L., 2011, "Research Progress on Packaging Thermal Management Techniques of High Power LED," *Advanced Materials Research*, (vol. 347-353) pp.3989-3994.

86. Christensen, A. and Graham, S., 2009, "Thermal Effects in Packaging High Power Light Emitting Diode Arrays," *Applied Thermal Engineering*, (29) pp. 364-371.

87. Lai, Y., Cordero, N., Barthel, F., Tebbe, F., Kuh, J, Apfelbeck, R., and Wurtenberger, D., 2009, "Liquid Cooling of Bright LEDs for Automotive Applications," *Applied Thermal Engineering*, (29) pp 1239-1244.

88. NEMA, 1998, "Industrial Laminating Thermosetting Products*."*

89. 3M Thermal Management Fluids, "Safe Sustainable Cooling Performance – Dielectric heat transfer solutions for the electronics industry," Accessed November 2011.

90. 3M Thermal Management Fluids, "3M Novec 72DE Engineering Fluid," Accessed November 2011.

91. Shirtcliffe, N.J., McHale, G., Newton, M.I., and Perry, C.C., 2005, "Wetting and Wetting Transitions on Copper Based Super-Hydrophobic Surfaces," *Langmuir*, (21) pp. 937-943.

92. Mughal, M.P. and Plumb, O.A., 1996, "An Experimental Study of Boiling on a Wicked Surface," *International Journal of Heat and Mass Transfer*, (39) No. 4, pp. 771-779.

93. Williams, R.R. and Harris, D.K, 2006, "A Device and Technique to Measure the Heat Transfer Limit of a Planar Heat Pipe Wick*, Experimental Thermal and Fluid Science*, (30), pp 277-284.

94. Yeh, C.C., Chen, C.N., and Chen, Y.M., 2009, "Heat Transfer Analysis of a Loop Heat Pipe With Biporous Wick," *International Journal of Heat and Mass Transfer*, (52) pp. 4426-4434.